The relationships between tectonics, climate and exhumation in the Central Andes (18-36°S): evidence from low-temperature thermochronology

Nadja F. Stalder[1], Frédéric Herman[1], Giuditta M. Fellin[2], Isabelle Coutand[3], Germán Aguilar[4], Peter W. Reiners[5], Matthew Fox[6]

1 Institute of Earth Surface Dynamics, Université de Lausanne, 1022 Chavannes-près-Renens, Switzerland

2 Department of Earth Sciences, ETH Zurich, 8092 Zurich, Switzerland

3 Department of Earth Sciences, Dalhousie University, Halifax, Canada

4 Advanced Mining Technology Center, Facultad de Ciencias Físicas y Matemáticas, Universidad de Chile, Santiago, Chile

5 Department of Geosciences, University of Arizona, Tucson, AZ 85721

6 Department of Earth Sciences, University College London, Gower Street, London, WC1E 6BT, United Kingdom

Abstract

The Central Andes between 18°S and 36°S latitude strike north-south for 2000 km along the Chilean subduction margin, cross several climate zones from hyperarid to humid and exhibit mean elevations in excess of 4000 m.a.s.l. Here, we investigate the relationships between tectonics, climate and exhumation by inverting low-temperature thermochronological data compiled from the literature (824 ages from 549 samples) and new data (238 ages from 146 samples) to quantify the exhumation rate history of the Central Andes since 80 Ma. Our inferred exhumation rates west of the drainage divide and between 18 and 32°S did not exceed 0.25 km/Ma. Such low exhumation rates are consistent with low shortening rates and arid conditions in this region. Local pulses of exhumation occurred only during the Eocene as response to active deformation and during the Miocene, probably as response to uplift of the western Andean slope. East of the drainage divide between 18 and 28°S, the observed exhumation pattern reflects the onset and eastward propagation of deformation. Here, exhumation occurred locally since the middle-to-late Eocene in the Eastern Cordillera and the Altiplano-Puna and subsequently affected larger parts of these regions and the north-western Sierra Pampeanas during the Oligocene. In the early Miocene (~20 Ma), the Interandean zone started exhuming and at 12-10 Ma exhumation propagated into the Subandean zone. Enhanced shortening rates and intensified precipitation along the eastern deformation front associated with the onset of the South American Monsoon led to increased exhumation rates in the eastern Interandean and the Subandean zones in the Plio-Pleistocene (0.6 km/Ma). Higher Pleistocene exhumation rates are also observed in the northern Sierra Pampeanas (1.5 km/Ma) that can be related to rock uplift along steep reverse faults coupled with high precipitation. South of 32°S on the western side, exhumation rates in the Principal Cordillera increased from ca. 0.25 km/Ma in the Miocene to rates locally exceeding 2 km/Ma in the Pleistocene. Whereas the tectonic regime in the southern Principal Cordillera remained unchanged since the late Miocene, these higher rates are likely associated with enhanced erosion resulting from intensified Pleistocene precipitation and glacial growth in this region, reinforced by isostatic rock uplift and active tectonics. Our study shows that the onset of exhumation correlates mainly with the initiation of horizontal shortening and crustal thickening, whereas the magnitude of exhumation is largely set by the amount of precipitation and glacial erosion and by the style of deformation, which is controlled by inherited structures and the amount of sediments in the foreland.

1. Introduction

The topographic, kinematic, and exhumational evolution of mountain belts reflects interactions between tectonic, climatic, and surface processes whose relative roles in forcing and modulating various features of orogens are widely debated (*e.g.*, England and Molnar, 1990; Molnar and England, 1990; Raymo and Ruddiman, 1992; Reiners et al., 2003; Molnar, 2009; Whipple, 2009; Champagnac et al., 2012; Herman et al., 2013). At convergent margins, tectonic forcing creates horizontal shortening that induces spatial gradients in crustal thickness, which drive both contractional deformation and surface uplift and initiate erosion. Erosion and sedimentation, in turn, have the potential to strongly influence the shape of the orogen by setting the orogenic mass balance and lithospheric stress regime that control internal deformation and isostatic uplift of mountain belts (Dahlen and Suppe, 1988; Koons, 1990; Molnar and England, 1990; Beaumont et al., 1992; Willett, 1999). The climatic factors that modulate these surface processes may also be influenced by the size, form and height of the orogen itself, further complicating efforts to resolve or distinguish the respective role of tectonics and climate in shaping mountain ranges.

Numerical (Beaumont et al., 1988; Koons, 1989; Beaumont et al., 1992; Willett et al., 1993; Batt and Braun, 1997; Willett, 1999) and analogue models (Davies et al., 1983; Dahlen and Suppe, 1988; Malavieille 1984; Koons, 1990; Konstantinovskaia and Malavieille, 2005) suggest that along-strike variations in orogen height and width may be caused by either differences in tectonically-controlled variations in horizontal shortening rate (e.g., Isacks, 1988; Gephart, 1994; Kley and Monaldi 2002; Giambiagi et al., 2012), or climatically-forced variations in erosion rate (e.g., Masek et al., 1994; Horton, 1999; Montgomery et al., 2001). Similarly, in an orogen with steady form, localized regions of high rock uplift and erosion rates, or cross-orogen differences in these rates, could be driven by either kinematic or climatic factors, or both. In both cases, positive feedbacks will complicate the discrimination between tectonic and climatic effects on the kinematics, erosion, and topography of orogens (e.g., Molnar, 2009). Nevertheless, it is reasonable to expect that independent, far-field-driven changes in either tectonic or climatic processes affect orogens in ways that would allow us to examine their responses in size, form, internal kinematics, and erosion rates, as well as the response of the coupled forcing (climate or tectonics).

For example, a change in the convergence rates between plates may change the amount and rate of shortening. Shortening, together with other processes either contributing to crustal thickening, as for instance magmatism (*e.g.*, Francis and Hawkesworth, 1994; de Silva and Kay, 2018), or to surface uplift, as for instance dynamic uplift related to mantle processes (*e.g.*, Dávila and Lithgow-Bertelloni, 2015), construct topography that sustains higher exhumation rates. The amount and rate of shortening might also be influenced by the amount of sediments and the presence of decollement layers and inherited structures in the foreland that control the structural mode of deformation (*i.e.*, thick- versus thin-skinned) and the fault geometry (*e.g.*, Allmendinger et al., 1983; Allmendinger and Gubbels, 1996). If the topographic growth is sufficient to build orographic barriers, the precipitation pattern changes and may alter the distribution and magnitude of exhumation rates. Increased precipitation should be observable in the sedimentary record of the orogen by a change in the sedimentary facies (*e.g.*, Strecker et al., 2007). Focused precipitation at the range front may also promote out-of-sequence thrusting related to enhanced erosion (Horton, 1999), whereas on the lee side of the orographic barrier the crust thickens in the absence of erosion and a high-elevation plateau in the orogen interior might form (Willett, 1999). Finally, the drop of the equilibrium line altitude (ELA) during the Late Cenozoic cooling resulted in wide-spread glaciations and might has led to increased erosion rates in mountainous regions (*e.g.*, Herman et al., 2013). Yet evidence of feedbacks that are not only circumstantial are challenging to observe in field studies (Whipple, 2009; Whipple, 2014), which are complicated by uncertainties in the reconstruction of tectonic, climate and erosion rate histories (*e.g.*, Montgomery et al., 2001; Zhang et al., 2001; Molnar, 2004; Champagnac et al., 2012; Herman et al., 2013; Herman and Champagnac, 2016; Willenbring and Jerolmack, 2016; Carretier et al., 2018).

In this study, we use the Central Andes (18 – 36 °S) as a natural laboratory to investigate how the exhumation rate varied through time with the evolution of the mountain belt and across different tectonic and climatic gradients. The Andes are formed by the active subduction of the Nazca plate below the South American plate and stretch for approximately 7000 km along the west coast of South America. They cross several climatic zones from the tropics to the polar regions, which results in strong precipitation gradients both across and along the strike of the orogen (*e.g.*, Schwerdtfeger et al., 1976; Garreaud, 2009; Garreaud et al., 2009).

A large number of studies attributed the variable Andean rock uplift, erosion and morphology to different tectonic and geodynamic processes (*e.g.*, Barnes et al., 2006; Gillis et al., 2006; Spikings et al., 2008; Strecker et al., 2009; Hilley and Coutand, 2010; Carrapa and DeCelles, 2015; Reiners et al., 2015) and climatic conditions (*e.g.*, Masek et al., 1994; Horton, 1999; Montgomery et al., 2001; Lamb and Davis, 2003; Thomson et al., 2010; Barnes et al., 2012). To shed new light on the outstanding questions about the influence of climate through erosion on the dynamical evolution of mountain ranges, we integrate a wide range of stratigraphic, geochronologic and thermochronologic data sets at the scale of an orogen. We use the central and southern Central Andes (18-36°S) as a natural laboratory. To our knowledge, this has not been tempted at such spatial and temporal scales and in such detail.

In the following, we present new low-temperature thermochronological data (238 ages) that we complement with literature data (824 ages) to constrain the exhumation rate history of the Andean mountain belt at large temporal (Ma) and spatial scales (18 to 36°S). We focus on apatite and zircon fission track (AFT and ZFT, respectively) and apatite and zircon (U-Th)/He (AHe and ZHe) data. Our study area is located in the central and southern part of the Central Andes (Gansser, 1973; Ramos, 1999) and is informally divided into a northern (18-28°S), a central (28-32°S), and a southern (32-35°S) segment based on the different morphotectonic structures observed in these parts of the Central Andes (e.g., Charrier et al., 2007). First, we review the deformation and climatic histories of the Central Andes and briefly discuss the geothermal field and magmatic activity that can influence the interpretation of thermochronological data. Based on the low-temperature thermochronological data, we then model thermal histories and interpret them in terms of the exhumation rate history of the Central Andes since 80 Ma using an inverse approach. The changes in exhumation rates are compared to changes in the tectonic and climatic records to investigate the role of tectonic and climatic processes on exhumation. We find that in the western part of the northern segment, where the climate is dry and shortening rates are low, Cenozoic exhumation rates vary little through time and are lower than 0.25 km/Ma. East of the drainage divide in the northern segment, exhumation locally started in the middle-to-late Eocene in the Eastern Cordillera and Altiplano-Puna plateau and expanded into wider parts of these regions during the Oligocene. During the Miocene, exhumation subsequently spread into the eastern part of the southern Eastern Cordillera and into the Interandean- and Subandean zones, with rates between ca. 0.1 and 0.25 km/Ma. This reflects the onset and eastward propagation of compressional deformation in these regions. Compared to the west, the higher rates can be explained by higher shortening rates and higher precipitation in this region. Highest exhumation rates are observed in the Pleistocene in the southern Principal Cordillera west of the Andean range crest (≥2 km/Ma), that coincide with Pleistocene glacial growth, and in the northern Sierra Pampeanas (1.5 km/Ma) and the Subandean belt (0.6 km/Ma) east of the crest that relate to tectonic activity and enhanced precipitation in these regions. We conclude that the onset of exhumation is mostly consistent with the beginning of compressional tectonics and crustal thickening, whereas the climate significantly influences the magnitude of the observed exhumation rates.

2. Deformation history of the Central Andes

The Andean mountain belt is a type-example of a non-collisional orogen in an ocean-continent subduction setting (Dewey and Bird, 1970), formed by the ongoing eastward subduction of the Nazca Plate below the South American Plate (*e.g.*, Barazangi and Isacks, 1976; Cahill and Isacks, 1992). The present-day geometry of the subduction zone in the study area shows a flat slab segment between 28° and 32°S latitude (Barazangi and Isacks, 1976; Cahill and Isacks, 1992) that initiated in the Miocene (Kay and Mpodozis, 2002) (Fig. 1). Based on the tectonostratigraphic and magmatic records, the Andean orogeny started in the Late Cretaceous at about 100 Ma, when the prevailing extensive regime of back-arc spreading and rift basins changed into a convergent arc setting (*e.g.*, Mpodozis and Ramos, 1989; Charrier et al., 2007; Horton et al., 2018a,b).

Compilations of shortening estimates suggest a significant decrease of the total amount of crustal shortening with latitude, from 270-420 km at 21°S to 31-71 km at 33.5°S (*e.g.*, Kley and Monaldi, 1998; Oncken et al., 2006; Faccenna et al., 2017; Schepers et al., 2017 and references therein). Similarly, reconstructed average crustal shortening rates have consistently been higher in the North than in the South and varied between 1.2 mm/a and 16 mm/a in the north and between 1.2 and 6.5 mm/a in the south during the last 45 Ma (Oncken et al., 2006; Giambiagi et al., 2015a; Riesner et al., 2018) (Fig. 2). Due to structural inheritances and thickness variations in the pre-existing sedimentary cover, compressional deformation in the Central Andes can be described by three different deformational styles (e.g., Allmendinger et al., 1983; Allmendinger and Gubbels, 1996; Kley et al., 1999; McQuarrie and DeCelles, 2001; McQuarrie et al., 2002; Giambiagi et al., 2003; Elger et al., 2005; Anderson et al., 2017). i) Thin-skinned deformation in a typical foreland basin system as observed in the Subandean fold-and-thrust belt and adjacent Chaco foreland basin in the Bolivian Andes. Here, the fold-and-thrust belt developed in a thick Paleozoic to Mesozoic sedimentary sequence, where shortening has been accommodated by intra-sedimentary deformation along primarily east-vergent, flat-ramp thrust systems and by displacement on the basal décollement (e.g., Allmendinger et al., 1983; Baby et al., 1992; Dunn et al., 1995; Kley, 1996; Horton and DeCelles, 1997; Anderson et al., 2017). ii) Basement-core uplift as observed in the Sierra Pampeanas, where almost no sediment cover existed before the onset of contractional deformation (Allmendinger et al., 1983). Here, tectonic shortening is accommodated by spatially disparate, diachronous uplift of Proterozoic-to-Paleozoic basement blocks that are bound by high-angle reverse faults formed along inherited structures associated with earlier deformation (Jordan and Allmendinger, 1986; Strecker et al., 1987; Grier et al., 1999; Hilley et al., 2005). The newly formed Neogene contractional basins are passively transported in the hanging-wall of these basement ranges. iii) A combination of these two deformational styles, where both the basement and the sedimentary cover are deformed in a mix of flat-ramp thrusts and steep structures rooting in the deeper basement as for instance in the Eastern Cordillera (e.g., McQuarrie and DeCelles, 2001; McQuarrie, 2002; Müller et al., 2002; Pearson et al., 2013; Anderson et al., 2017), the Interandean zone (e.g., Kley, 1996; Anderson et al., 2017), the Altiplano-Puna (e.g., Kraemer et al., 1999; Coutand et al., 2001), the Santa Barbara range (e.g., Kley and Monaldi, 2002) and the Principal and Frontal Cordilleras (e.g., Giambiagi et al., 2003; Riesner et al., 2018). Below, we review the Andean deformation history by extracting the occurrence of syntectonic sediments and other structural and sedimentological observations from the literature in three segments (northern, central and southern) that show different tectonic and climatic conditions (Fig. 3, supplementary Table S6). Note that we exclude studies that use thermochronology to infer onset and magnitude of deformation or shortening rates to avoid circular reasoning when comparing it to the modelled exhumation rates derived by our approach. Our review aims at constraining shortening rates to provide a first-order constraint on crustal thickening processes. However, the amount of shortening and estimated shortening rate reconstructions summarized here and depicted in Figure 2 should be interpreted with care. Shortening estimates on the western side of the Andes and in large parts of the Altiplano are poorly resolved because deformation markers are obscured by both volcanic deposits and little to non-incised intramontane basins. Detailed reconstructions are thus restricted to the Eastern Cordillera and the Inter- and Subandean zones. Also, all estimates should be regarded as minimum values due to erosional removal of hanging-wall cut-offs and the incompleteness of the sedimentary record. Furthermore, shortening estimates are very variable among different studies as they rely largely on balanced cross-section, as for instance between 270 km (Oncken et al., 2006) and 420 km (Schepers et al., 2017) at 21°S. Such differences are due to the fact that balanced cross-sections are commonly built from surface observations with sparse control of the geometry and kinematics of deep structures and on the constant-area assumption that is generally valid at shallow crustal levels only, leaving shortening at depth largely unknown. Differences also arise from inherent subjectivity of the applied techniques and from the lack of unified structural evaluation, since most shortening estimates focus only on specific tectonomorphic units and transects across the entire Andes are rare. Yet, despite the fact that shortening estimates have clear limitations, they provide fundamental insight into the deformation history, which we summarize below.

2.1. Northern segment (18 - 28°S)

The northern part of this segment (18 - 23.5°S) is a wide mountain belt that comprises, from west to east, the Coastal Cordillera, the Central Depression, the Western Cordillera, the Altiplano-Puna plateau, the Eastern Cordillera and the Interandean and Subandean zones (Fig. 1). South of 23.5°S, the Subandean zone is replaced by the Santa Barbara system and the southern Eastern Cordillera, which sit over the transition zone from a steeply subducting Nazca Plate to a flat slab geometry. These units end at around 26°S and the Sierra Pampeanas appears. We first describe the deformation history in the region between 18 and 23.5°S and then briefly review the tectonic setting in the southern part between 23.5° and 28°S. Our main focus is on the eastern flank of the orogen since little is known about deformation on the western side.

At 21°S, the Central Andes are 720 km wide from the coast to the present mountain front in the Subandean zone and record more than 270-420 km of total shortening (*e.g.*, Kley and Monaldi, 1998; McQuarrie et al., 2005; Oncken et al., 2006; Eichelberger et al., 2013; Anderson et al., 2017; Faccenna et al., 2017; Schepers et al., 2017). This shortening is thought to have been accommodated mainly by the Eastern Cordillera and Interandean zone (190 ± 46 km), the Subandean belt (82 ± 21 km) and the Altiplano (65 km) over the last 40-50 Ma, whereas shortening in the Central Depression and Western Cordillera seems to be less important (Anderson et al., 2017).

Mountain building is thought to have started in the Late Cretaceous (90 Ma) in the Central Depression and Western Cordillera as suggested by compressional growth structures and angular unconformities in Late Cretaceous to late Eocene sediments (Mpodozis et al., 2005; Arriagada et al., 2006; Amilibia et al., 2008; Herrera et al., 2017) and by the early foreland basin depositional history preserved in the Altiplano basin (Horton and DeCelles, 1997; Sempere et al., 1997; Horton et al., 2001; Elger et al., 2005; McQuarrie et al., 2005; DeCelles et al., 2011; Horton, 2018a) (Fig. 3A). This is also corroborated by increasing proportions of granitic clasts with western provenance observed in Late Cretaceous sediments of the Salar de Atacama Basin, which indicate unroofing of the Western Cordillera or "*Cordillera Domeyko*" during that time (Bascuñán et al., 2016). This initial period of shortening was followed by a complex deformation history with contractional, strike-slip and extensional phases from the Oligocene to the earliest Miocene in the Western Cordillera (Pananont et al., 2004; Arriagada et al., 2006; Jordan et al., 2007; Bascuñán et al., 2019). Since then, the area underwent west-vergent thrusting, tilting and local extension (Muñoz and Charrier, 1996; Victor et al., 2004; Farías et al., 2005). Shortening rates west of the Altiplano did not exceed 1.2 mm/a and were always lower than in the east of the Altiplano (Oncken et al., 2006). Highest rates were observed during the Eocene and are possibly associated with enhanced mountain building in the Western Cordillera ("*Cordillera Domeyko*"; *e.g.*, Charrier et al., 2007). At about 40 Ma, shortening rates in the west slowed down to <0.25 mm/a (Victor et al., 2004; Oncken et al., 2006) and the thrust front moved into the Eastern Cordillera that shows tectonic activity until the late Miocene (McQuarrie and DeCelles, 2001; Müller et al., 2002; McQuarrie et al., 2005). By the early Oligocene, deformation affected most parts of the orogen including the Altiplano and expanded as far as 26°S south into the Puna (Coutand et al., 2001; DeCelles and Horton, 2003; Elger et al., 2005; McQuarrie et al., 2005; Oncken et al., 2006; DeCelles et al., 2011) (Fig. 3A). Shortening rates in the Altiplano show high local and temporal variability in the range of 0.1 and 3 mm/a, with a period of quiescence in the early Miocene (Elger et al., 2005). In the Eastern Cordillera, shortening rate estimates based on stratigraphy and fault kinematics suggest that shortening culminated in the Oligocene to early Miocene with rates of 5-10 mm/a (Müller et al., 2002; Elger et al., 2005). In the early Miocene (25-21 Ma), shortening in most parts of the Eastern Cordillera ceased except for some out-of-sequence thrusting in its central part (Müller et al., 2002; Horton, 2005; Anderson et al., 2017) and the deformation front migrated eastward across the Interandean zone, where the majority of the shortening between 25 and 10 Ma (70 km) took place (Horton, 2005; Elger et al., 2005; Anderson et al., 2017; Calle et al., 2018). At 12-10 Ma, deformation in these parts of the Andes finally terminated (Gubbels et al., 1993; McQuarrie et al., 2005; Calle et al., 2018) and moved into the Subandean fold-and-thrust belt, where east-vergent thrust systems subsequently incorporated sediments previously deposited in the early foreland basins and accommodated up to 82 km of shortening (Baby et al., 1992; Kley, 1996; Dunn et al., 1995; DeCelles and Horton, 2003; Echavarria et al., 2003; Uba et al., 2005; Uba et al., 2006; Uba et al., 2009; Calle et al., 2018). Shortening rate estimates in the Subandean zone suggest that shortening rates either (1) steadily increased since 9 Ma to a maximum of 11 mm/a at 3 Ma and a present-day rate of 8 mm/a or (2) that shortening occurred in two discrete pulses from 9-7 Ma and 2-0 Ma with maximal rates of 13 mm/a, which were separated by a period of modest shortening rates (0-5 mm/a) (Echavarria et al., 2003).

At around 24.5°S, the Central Depression on the western side of the Central Andes narrows and finally disappears at 28°S. Similarly, the Subandean fold-and-thrust belt on the eastern side disappears around 23.5°S and is replaced by the southern Eastern Cordillera and the Santa Barbara system and, south of 26°S, the Sierra Pampeanas (Fig. 1). These structural changes in the foreland may be linked to the transition from a steep to a flat subduction geometry (*e.g.*, Jordan et al., 1983) as well as to inherited paleogeography and associated thickness variations of pre-Cenozoic strata (*e.g.*, Allmendinger et al., 1983; Allmendinger and Gubbels, 1996; Pearson et al., 2013; del Papa et al., 2013). Compared to the thin-skinned Sub-Andean fold-and-thrust belt that formed in a zone of thick Paleozoic and Mesozoic sedimentary cover, the preexisting sedimentary accumulations are thinner in the Santa Barbara system and almost absent in the thick-skinned Sierra Pampeanas (Allmendinger et al., 1983). The total amount of shortening at 24-25°S is ca. 142 km and thus significantly less than at 21°S (Pearson et al., 2013). Deformation across the Puna, the southern Eastern Cordillera and the Santa Barbara system was spatially disparate and predominantly along reactivated extensional structures associated to the Cretaceous-to-Paleogene Salta rift system (Grier et al., 1991; Kley and Monaldi, 2002). This resulted in a Paleogene broken foreland where Cenozoic sediments were deposited in intermontane basins separated by uplifted ranges of Proterozoic and Paleozoic basement, similar to the present-day broken foreland of the Sierra Pampeanas (*e.g.*, Hongn et al., 2007; del Papa et al., 2013; Montero-López et al., 2016). Growth strata in these intermontane basins indicate that tectonic activity started in the middle Eocene at the Puna margin in the southern Eastern Cordillera (*e.g.*, Hongn et al., 2007; Montero-López et al., 2016) and in the late Eocene to Oligocene in the Puna plateau interior (Kraemer et al., 1999; Coutand et al., 2001; Carrapa and DeCelles, 2008). In the Puna, shortening was largest in the middle Miocene and continued until the Pliocene (Kraemer et al., 1999; Coutand et al., 2001). To the east, the exhuming Puna margin shed detritus into a formerly unrestricted foreland that became compartmentalized in the middle to late Miocene, when ensuing shortening led to the uplift of Paleozoic basement in the western and central parts of the Eastern Cordillera (Hilley and Strecker, 2005; Coutand et al., 2006; Deeken et al., 2006; Carrera and Muñoz, 2008; Hain et al., 2011). Concurrent range uplift at the Eastern Cordillera-Santa Barbara boundary documents the disparate nature of deformation (Hain et al., 2011). Tectonic activity continued during the Plio-Pleistocene across the entire foreland by promoting further basement uplift in its eastern part and by maintaining synsedimentary deformation in the intermontane basins of the Eastern Cordillera (Hilley and Strecker, 2005; Coutand et al., 2006; Carrera and Muñoz, 2008; Hain et al., 2011). Deformation in the northern Sierra Pampeanas started during the late Miocene by fragmentation of the former continuous foreland basin (Strecker et al., 1989; Bossi et al., 2001; Carrapa et al., 2008; Zapata et al., 2019), although some topography may have already existed before in its eastern part (Strecker et al., 1989; Zapata et al., 2019). Major relief development and range uplift occurred after 6 Ma along reverse fault-bounded basement blocks akin to the structures in the Eastern Cordillera and the Santa Barbara system (Strecker et al., 1989, Bossi et al., 2001; Carrapa et al., 2008; Zapata et al., 2019). Folded and overthrusted Quaternary units in the eastern part document that deformation in this region continued during the Plio-Pleistocene (Strecker et al., 1989).

In summary, and as depicted in Fig. 3A, the sedimentary record between 18° and 23.5°S shows different deformation histories for the western and the eastern sides of the Central Andes. The western side of the Andes shortened relatively continuously since the Late Cretaceous to the present-day, with deformation reaching its climax in the Eocene (*e.g.*, Charrier et al., 2007). At this time, compressional deformation initiated in the Eastern Cordillera (*e.g.*, Müller et al., 2002; Elger et al., 2005). From the Oligocene until 10 Ma, the whole Andes except for the Subandean zone experienced major tectonic deformation (Fig. 3A). Since 12-10 Ma (*e.g.*, Gubbels et al., 1993), deformation north of 23.5°S has mainly been accommodated in the thin-skinned fold-and-thrust belt forming the Subandean zone, where shortening rates may have reached up to 13 mm/a in the Pliocene (Echavarria et al., 2003). South of 23.5°S, the Subandean belt disappears and the dominant deformation mode is thick-skinned. Here, deformation started in the Eocene in the Puna and the westernmost southern Eastern Cordillera (*e.g.*, Montero-López et al., 2016). In the middle to late Miocene, the continuous foreland was dissected into several intermontane basins that are separated by basement blocks uplifted along steep reverse faults related to inherited extensional structures (*e.g.*, Strecker et al., 1989; Coutand et al., 2006). Deformation continued during the Plio- and Pleistocene (*e.g.*, Strecker et al., 1989; Carrera and Muñoz, 2008).

2.2. Central segment (28 - 32°S)

The central segment of our study area (28-32°S) is located above the contemporary Pampean flat slab segment of the Nazca subduction zone. It comprises from west to east the Coastal, Principal and Frontal Cordilleras, the Precordillera, the Santa Bárbara system and the Sierra Pampeanas (Fig. 1).

Syntectonic sediments from the Principal and Frontal Cordilleras indicate that a first pulse of compressional deformation may have taken place during the Late Cretaceous to the Paleocene, between 82 and 45 Ma (Martínez et al., 2016; Rossel et al., 2016; Martínez et al., 2018) (Fig. 3B). Such an early onset of mountain building and topographic growth is also corroborated by the onset of incipient retroarc foredeep sedimentation with provenance from the Frontal Cordillera and magmatic arc by at least the late Eocene (Fosdick et al., 2017). During the Oligocene, extensional structures in the Doña Ana Group are related to an intra-arc and retro-arc setting in the Frontal Cordillera (Winocur et al., 2015). Compression in the Frontal Cordillera resumed in the early Miocene and led to the inversion of the previously formed basins (Winocur et al., 2015; Martínez et al., 2016; Rossel et al., 2016; Martínez et al., 2018). Shortening now also affected the western part of the Precordillera, as evidenced by early Miocene (~20 Ma) syntectonic growth strata and onlap structures identified on seismic data (Allmendinger et al., 1990; Jordan et al., 1993) (Fig. 3B) and by the oxygen isotope record of pedogenic carbonates that indicate that this part of the Precordillera has attained present-day elevations before 9 Ma (Hoke et al., 2014). This early phase of deformation was followed by 3 to 4 Myr of tectonic quiescence. At 15 Ma, shortening resumed and peaked around 9-12 Ma with rates of 20-25 mm/a, followed by decreasing rates >10 mm/a (Jordan et al., 2001a; Allmendinger and Judge, 2014). Deformation then subsequently propagated to the east where it affected the eastern part of the Precordillera and the Sierra Pampeanas since 5-7 Ma (Strecker et al., 1989; Jordan et al., 1993; Jordan et al., 2001a) (Fig. 3B).

2.3. Southern segment (32 - 36°S)

The southern segment of our study area (32 - 36°S) includes the transition from the shallowly dipping segment of the Nazca subduction zone to a moderately (30°) dipping segment south of 33°S. Here, the Central Andes comprise the Coastal Cordillera, the Central Depression, the Principal Cordillera, the Frontal Cordillera and the eastern Malargüe fold-and-thrust belt and foreland basin (Fig. 1).

Thrust-related growth strata and evidence of basin inversion in the Coastal Cordillera/Central Depression and in the Malargüe fold-and-thrust belt also suggest a late Cretaceous (~100 Ma) onset of shortening in this part of the Andes (Horton, 2018b and references therein) (Fig. 3C). However, the formation of several basins filled by volcano-sedimentary deposits in the late Eocene to the Oligocene (~37-23 Ma) document large-scale extension and crustal thinning in this region, similar to the setting at 30°S (Jordan et al., 2001b; Charrier et al., 2002; Ramos and Folguera, 2005; Burns et al., 2006; Folguera et al., 2010; Rojas Vera et al., 2010; Horton et al., 2016; Horton et al., 2018b). Shortening finally resumed in the latest Oligocene by tectonic inversion of the former extensional basins (Godoy et al., 1999; Charrier et al., 2002). Neogene compressional syntectonic strata at 33-34°S are observed in the inverted Abanico basin in the western Principal Cordillera, in the Alto Tunuyán basin separating the Principal and Frontal Cordilleras, and in the foreland (Giambiagi et al., 2001; Giambiagi et al., 2003; Fock et al., 2006; Porras et al., 2016; Riesner et al., 2017; Riesner et al., 2018) (Fig. 3C).

Deformation in the southern segment was accommodated by two fold-and-thrust belts of opposite vergence located in the Principal Cordillera. Two contrasting views about the onset, the intensity and the partitioning of deformation have been proposed based on either an east-vergent structural model (e.g., Giambiagi and Ramos, 2002; Farías et al., 2010; Giambiagi et al., 2012; Giambiagi et al., 2015a) or a bi-vergent model (Armijo et al., 2010; Riesner et al., 2017; Riesner et al., 2018; Riesner et al., 2019). In the east-vergent model, most of the orogenic shortening has been accommodated by east-vergent thrusts in the hybrid thick- and thin-skinned Aconcagua fold-and-thrust belt, which is located in the eastern Principal Cordillera and separates the modern volcanic arc and the basement culmination of the Frontal Cordillera (Giambiagi et al., 2015a and references therein). According to this model, compressional deformation started around 22 Ma in the western and central Principal Cordillera by inversion of the Abanico basin (Godoy et al., 1999; Charrier et al., 2002; Fock et al., 2006), which resulted in 7-16 km of shortening during the early Miocene (Farías et al., 2010; Giambiagi et al., 2015a). Shortening in the Aconcagua fold-and-thrust belt in the eastern Principal Cordillera initiated around 18-15 Ma and was active until the early Pliocene (~5 Ma) as revealed by syntectonic sediments deposited in the Alto Tunuyán wedge-top basin adjacent to the east (Giambiagi et al., 2001; Giambiagi and Ramos, 2002; Giambiagi et al., 2003; Giambiagi et al., 2015a; Porras et al., 2016) (Fig. 3C). East of the Principal Cordillera, shifts in the sedimentary provenances in the foreland basin at 16 Ma and in the Alto Tunuyán Basin at 11-9 Ma indicate important uplift of the Frontal Cordillera during that time that continued through the Pliocene (Irigoyen et al., 2000; Giambiagi et al., 2003; Porras et al., 2016; Buelow et al., 2018). This is also corroborated by the oxygen isotope record of pedogenic carbonates from the Alto Tunuyán Basin that indicates that 2 ± 0.5 km of surface uplift occurred during the Mio-Pliocene (Hoke et al., 2014). In the Pliocene (~4 Ma), compressional deformation finally propagated to the eastern Frontal Cordillera and to the Cuyo foreland (Irigoyen et al., 2000; Giambiagi et al., 2003; García and Casa, 2014; Giambiagi et al., 2015b). In this model, the Coastal Cordillera and the western Principal Cordillera were uplifted passively due to the tectonic activity of the Aconcagua fold-and-thrust belt (Giambiagi et al., 2015a), with main surface uplift occurring during the late Miocene (10.5 Ma) to the Pliocene (4.6 Ma) based on geomorphologic evidence (Farías et al., 2008). However, recent detailed analyses of syntectonic deposits in Oligocene-to-Miocene sedimentary rocks of the western Principal Cordillera indicate the activity of a series of west-vergent thrusts since 25 Myr, which form the West-Andean fault-and-thrust belt (Riesner et al., 2017). These faults inverted and folded the former Oligocene-to-Miocene Abanico basin with an average shortening rate of 0.1-0.5 mm/a. Its westernmost fault delineates the current western mountain front of the Principal Cordillera, where deformation is still active today as testified by shallow seismic activity and at least two paleo-earthquakes in the past 20 ka (Barrientos et al., 2004; Vargas et al., 2014). To the east, a series of out-of-sequence thrusts deformed Jurassic to Miocene sediments in west-vergent folds between 15 Ma to 5 Ma that link the West-Andean thrust belt with the east-vergent Aconcagua fold-and-thrust belt (Riesner et al., 2018). These new insights indicate that the western part of the Andean mountain belt has accommodated more shortening and deformation than previously thought (Armijo et al., 2010; Riesner et al., 2017; Riesner et al., 2018). Therefore, shortening in the Principal Cordillera and uplift of the Frontal Cordillera is proposed to be accommodated by a bi-vergent orogen with continuous, primary westward deformation since 25-20 Ma. The Aconcagua fold-and-thrust belt is considered as a secondary structural feature which passively accommodated Andean deformation along thin-skinned thrusts (Riesner et al., 2018), instead of being the principal structure as suggested by Giambiagi et al. (2015a). These two contrasting models also lead to different shortening rate reconstructions across the Andes (Fig. 2). According to Riesner et al. (2018), the long-term average shortening rate is 1.2 - 2.2 mm/a. In the reconstruction of Giambiagi et al. (2015a), shortening peaks between 17-11 Ma with rates of 4.7-6.5 mm/a and is lower before 17 Ma (2 mm/a) and during the Pliocene (1.6 mm/a). The total amount of shortening decreases from 31-71 km at 33.5°S (Giambiagi and Ramos, 2002; Giambiagi et al., 2012; Giambiagi et al., 2015a; Riesner et al., 2018) to 10-13 km at 36°S (Giambiagi et al., 2012). The Frontal Cordillera disappears south of 34.5°S (Giambiagi et al., 2012) and the Aconcagua fold-and-thrust belt gives way to the thick-skinned Malargüe fold-and-thrust belt and its corresponding foreland basin (Ramos et al., 1996), which are both characterised by syntectonic sediments younging to the east (*e.g.*, Horton et al., 2018b and references therein).

2.4. Summary of the deformation history of the Central Andes

As outlined above, the magnitude and onset of deformation in the Central Andes varies considerably with latitude (Fig. 2, Fig. 3). The total amount of shortening is highest in the northern segment of the study area and was accommodated mostly in the eastern part of the orogen (Fig. 3A). Shortening amounts decrease substantially towards the south. The compressional regime in the central and southern segments was interrupted by a period of foreland quiescence and hinterland extension in the late Eocene to the late Oligocene (*e.g.*, Litvak et al., 2007; Wincour et al, 2015; Horton et al., 2016; Horton et al., 2018b), while the north experienced a major phase of deformation (*e.g.*, Elger et al., 2005; McQuarrie et al., 2005) (Fig. 3). Deformation resumed at about 25 Ma and was accommodated by either an east-vergent fold-and-thrust belt in the eastern Principal Cordillera or by a doubly-vergent wedge with mainly westward deformation located in the western Principal Cordillera (Giambiagi et al., 2015a; Riesner et al., 2018).

3. Crustal thickening, magmatism and the geothermal field of the Central Andes

The primary control on surface elevation is isostasy (*e.g.*, Molnar and England, 1990). Erosion, magmatism, and tectonic shortening set the crustal thickness that in turn controls elevation (*e.g.*, Allmendinger et al., 1997; Kley and Monaldi, 1998; Giese et al., 1999). Additionally, mantle dynamics especially above subduction zones or crustal flow also influence topography, exhumation, and the shape of a mountain belt (*e.g.*, Jordan et al., 1983; Braun, 2010; Martinod et al., 2010; Dávila and Lithgow-Bertelloni, 2015; Flament et al., 2015; Siravo et al., 2019). In particular, and as for instance observed for the modern Pampean flat slab segment (28 - 32°S), flattening of the subducting slab may generate dynamic uplift (Dávila and Lithgow-Bertelloni, 2015; Flament et al., 2015) and induce shortening in the upper plate's interior far away from the trench, which leads to the widening of the mountain belt (Martinod et al., 2010). On the contrary, steep and retreating subduction slabs can lead to dynamic subsidence and to a topography that is lower than expected from crustal thickening (Mitrovica et al., 1989; Royden, 1993). Based on the magmatic arc activity and on periods of deformation and crustal thickening, several past flat slab segments might have formed during the Cenozoic in the Central Andes (Ramos and Folguera, 2009 and references therein). These were located from 14° to 20°S between 45-35 Ma and 25 Ma, from 20° to 24°S between 18 and 12 Ma, and from 34.5°S to 37.75°S between 15 and 5 Ma (Ramos and Folguera, 2009). However, our compilation of igneous activity in the Central Andes (Fig. 4, supplementary Table S7) does not show the expected cessation of magmatism for the latest two periods of the proposed flat slab subduction in the respective locations of the Western and Principal Cordilleras. Hence, uncertainties about the past geometry of the subduction zone remain.

The magmatic contribution to crustal evolution and surface uplift in the Andes relative to crustal thickening due to tectonic shortening is difficult to constrain because of the uncertainty on the amount of igneous material added to the crust. This is commonly calculated from the volume of volcanic rocks by assuming a plutonic-to-volcanic ratio that can vary from 3:1 to 35:1 (*e.g.*, de Silva and Kay, 2018) and assuming a mantle contribution to the melt of roughly 50% (*e.g.*, Kay et al., 2010). Early estimates of magmatic addition are 13 km^2/Ma over the last 10 Ma at 21-22°S (Francis and Hawkesworth, 1994), but more recent estimates in the same region are much higher, up to 33-107 km^2/Ma over the last 11 Ma (de Silva and Kay, 2018). Assuming an average shortening rate of 9-10 mm/a (Fig. 2) and an average crustal thickness of 50 km, these estimates of magmatic addition indicate that the contribution of magmatic activity to crustal thickness relative to the contribution from tectonic shortening can vary between 2-3% and 6-24%. However, crustal thickening by shortening and magmatism is compensated in some places by crustal thinning resulting from processes like crustal delamination and forearc subduction erosion. For instance, the Altiplano-Puna plateau was rather a site of crustal loss than addition according to de Silva and Kay (2018). These processes of lithospheric removal and magmatic contribution may have resulted in ~1 km of Airy isostatic surface uplift in the Altiplano-Puna plateau over the last 11 Ma (Perkins et al., 2016). Although the highest estimates of magmatic contribution to crustal thickening do not exceed 25% relative to the amount of crustal thickening driven by tectonic shortening, these values indicate that magmatic addition is a non-negligible contribution to crustal growth. Therefore, we briefly review the current knowledge about crustal thickening and magmatic activity in the Central Andes.

3.1. Present-day crustal thickness

Continental-scale data analysis from satellite gravimetry, seismic refraction, receiver functions and surface wave tomography show that the thickest crust of South America (> 70 km) is located below the central Andean Plateau (~10° to 28°S) (*e.g.*, Beck et al., 1996; Giese et al., 1999; Assumpção et al., 2013; Chulick et al., 2013; van der Meijde et al., 2013). The crustal thickness then gradually decreases southwards to ca. 45 km at 35°S (Assumpção et al., 2013; Chulick et al., 2013; van der Meijde et al., 2013). Thinner crust is also observed in the South-American craton east of the Andes (30-40 km) and along the range in the Andean foreland, where the average thickness is below 35 km (Assumpção et al., 2013). Hence, the Central Andes show variable crustal thicknesses that correlate with topography at the orogen scale, suggesting a first-order local Airy-type isostatic compensation (*e.g.*, Molnar and England, 1990; Beck et al., 1996; Ryan et al., 2016).

3.2. Crustal thickening and magmatic arc evolution

The evolution of crustal thickening through time can be constrained by the geochemical composition of volcanic and magmatic arc products (*e.g.*, Leeman, 1983; Plank and Langmuir, 1988).

Several lines of evidence suggest that the Andean subduction and related magmatism along the Chilean continental margin were relatively continuous since the early Carboniferous, although variations in the global geodynamic processes and crustal thickness produced noticeable modifications of magmatism through time (*e.g.*, Scheuber et al., 1994; Mamani et al., 2010a; Charrier et al., 2015; Hervé et al., 2014; del Rey et al., 2016; Oliveros et al., 2018). Since the late Paleozoic until the Late Cretaceous (91 Ma), the subduction margin underwent tectonic stretching that resulted in crustal thinning (Mamani et al., 2010a). A magmatic arc slightly oblique to the present-day coastline and a (mainly) marine back-arc basin to its east were formed (Charrier et al., 2007; Mamani et al., 2010a; Charrier et al., 2015; Oliveros et al., 2018). Several pulses of magmatism occurred during this time and initiated the creation of the Coastal Batholith and associated volcanoclastic deposits in the Coastal Cordillera (Oliveros et al., 2007; Mamani et al., 2010a; Oliveros et al., 2018) (Fig. 4, supplementary Table S7). In the Late Cretaceous to the middle Oligocene, a relatively wide forearc basin formed to the west of the magmatic arc and the marine back-arc basin evolved into a terrestrial foreland basin filled by volcanoclastic products and continental deposits (*e.g.*, Lamb et al., 1997; Mpodozis et al., 2005; Charrier et al., 2007; Mamani et al., 2010a; Wotzlaw et al., 2011; Di Giulio et al., 2012; Charrier et al., 2013; Charrier et al., 2015; Bascuñán et al., 2016). The magmatic arc subsequently migrated to the east into the Western/Principal Cordillera where it is located today, with the exception of an amagmatic zone delineating the current Pampean flat slab segment between 28° and 32°S that initiated in the Miocene (*e.g.*, Kay and Mpodozis, 2002) (Fig. 4).

In the northern segment of the Central Andes, between 13° and 26°S, geochemical observations from magmatic and volcanic arc composition indicate incipient crustal thickening during the late Cretaceous (91 Ma) to the middle Oligocene (30 Ma) and major thickening since then (Kay et al., 1994; Mamani et al., 2010a; Profeta et al., 2015). Several observations suggest that the Western Cordillera and its slope reached a substantial part of its current elevation before or during the Miocene and that uplift in this region was a rather continuous process since at least the Neogene (Jordan et al., 2010; Evenstar et al., 2015; Scott et al., 2018). The uplift history of the Eastern Cordillera and the Altiplano is less clear (*e.g.*, Barnes and Ehlers, 2009). Studies using paleo-elevation and -temperature proxies from the Altiplano and Eastern Cordillera at 19-22°S suggest that these regions reached their modern elevations in the Burdigalian to Langhian after a pulse of surface uplift of 2-3 km, which is attributed to an isostatic response to crustal thickening and lower lithosphere delamination (Hoke and Garzione, 2008; Saylor and Horton, 2014; Garzione et al., 2017 and references therein). However, the use of such proxies to infer paleo-altitudes remains debated mainly because they may reflect changes in climate rather than in elevation (Ehlers and Poulsen, 2009) and other studies favour either an early, pre-Oligocene uplift history (*e.g.*, Canavan et al., 2014) or continuous growth since the Oligocene (*e.g.*, Fiorella et al., 2015) of the Eastern Cordillera and Altiplano-Puna plateau.

In the flat subduction segment and its margins, the late Oligocene to early Miocene volcanism is characterized by basaltic to andesitic composition erupted through a crust of normal thickness (30-35 km) in an extensional setting (*e.g.*, Kay and Mpodozis, 2002; Litvak et al., 2007). Incipient slab shallowing between 28° and 32°S in the latest early Miocene (~18 Ma) resulted in the broadening of the magmatic arc and in the eastward migration of the arc front into the Precordillera and Sierra Pampeanas (Kay et al., 1991; Kay and Mpodozis, 2002) (Fig. 4). Crustal thickening began in the middle to late Miocene (*e.g.*, Kay et al., 1991; Kay et al., 1994; Kay and Mpodozis, 2002; Litvak et al., 2007; Kay et al., 2014). With the peak of slab shallowing in the latest Miocene, igneous activity in the Principal Cordillera ceased by 8 to 5

Ma and shut down completely by 2 Ma in the Precordillera and Sierra Pampeanas, indicating full emplacement of the flat slab segment by the Pliocene (Kay and Mpodozis, 2002) (Fig. 4).

To the south of the flat slab segment between 33° and 36°S, the late Oligocene to early Miocene magmatic activity was concentrated at the western border of the Principal Cordillera in a relatively thin crust of 30-35 km (Nyström et al., 2003; Kay et al., 2005) (Fig. 4). Geochemical changes in the composition of the magmatic arc products indicate that crustal thickening in this part of the Andes began in the latest early Miocene (Kay et al., 2005). The magmatic arc front migrated 35 km towards the east from 19 to 16 Ma and additional 50 km from ca. 7 to 3 Ma to its current position at the Argentinian-Chilean border, where it has stayed during the last 3 Ma (Kay et al., 2005). By this time, the crust reached its present-day thickness of about 45-50 km (Kay et al., 2005).

3.3. Heat flow and geothermal gradients in the Central Andes

Exhumation rates derived from thermochronological data strongly depend on the assumed geothermal field. Whereas modern and past geothermal gradients set the depth of the closure isotherms of thermochronometers, the geothermal field is influenced by erosion due to its control on how fast heat is advected to the surface. Furthermore, magma bodies emplaced in the lower crust also influence thermochronometric ages in their surroundings and can lead to a misinterpretation of the observed cooling ages and exhumation rate history (*e.g.*, Calk and Naeser, 1973; Murray et al., 2018). Geothermal gradients in the Central Andes are expected to be different in distinct regions due to variable distances from the subduction trench, locations of the magmatic arc and crustal thicknesses. Present-day heat flow density data in the Central Andes come only from 74 boreholes (15-30°S) and are thus very sparse (Springer and Förster, 1998). These measurements reveal large across strike variations

(Springer and Förster, 1998). The Coastal Cordillera shows low values (20 mW/m^2) that increase to about 60 mW/m^2 at the western flank of the Western/Principal Cordillera. In the active magmatic arc (Western/Principal Cordillera) and the Altiplano, heat flow density values range from 50 to 180 mW/m^2 but are extremely sparse (Springer and Förster, 1998). The higher heat flow values in these parts may be related to isolated magma reservoirs in the shallow crust. Relatively high heat flow (80 mW/m^2) is further observed in the Eastern Cordillera, whereas the Subandean zone shows lower values of about 40 mW/m^2. Assuming an upper crustal thermal conductivity of 2.6 W/m/K (*e.g.*, Čermák and Rybach, 1982), these heat flow measurements translate to the following geothermal gradients: 8 °C/km in the Coastal Cordillera, 23 °C/km in the western flank of the Western/Principal Cordillera, 19-69 °C/km in the magmatic arc and Altiplano, 31 °C/km in the Eastern Cordillera and 15 °C/km in the Subandean zone and Andean foreland. At around 33°S in the Principal Cordillera, a geothermal gradient of 30-35 °C/km was measured (Höfer-Öllinger and Millen, 2010). Estimates of the Oligocene geothermal gradients in the Altiplano, Eastern Cordillera and Inter- and Subandean zones at 21°S range from 19 °C/km to 32 °C/km (Ege et al., 2007) and are thus similar to the present-day values.

We expect that geothermal gradients change through time due to changes in exhumation rates which control the advection of heat, due to evolving spatial patterns of magmatic activity and due to changes in slab geometry which likely change the temperature at the base of the crust from ambient mantle temperature within the mantle wedge to relatively chilled oceanic lithosphere. Our modeling accounts for the advection of heat driven by exhumation and we expect that the effects of magmatic activity can be mitigated by analyzing samples that are unlikely to be influenced by this activity. However, we do not account for changes in the slab geometry. Based on a crustal thickness of 50 km and a thermal diffusivity of 20 km^2/Ma, we expect that the temperature of the shallow crust (1-6 km) will respond to temperature changes at depth over a time scale of 125 Ma. Therefore, these thermal effects are not as important as changes in exhumation rates. However, our prescribed geothermal gradient in the inversion will significantly influence the magnitude of exhumation rates derived from thermochronological data. In particular, higher geothermal gradients will result in lower exhumation rates due to more efficient heat advection and shallower depths of closure of the thermochronologic systems. Therefore, exhumation rates will likely be underestimated in regions where the true geothermal gradient is lower than the modelled gradient and overestimated in places where it is higher.

4. Present-day and Cenozoic climate

4.1. Present-day climate of the Central Andes

The Central Andes cross several climate zones from arid and tropical conditions in the north to temperate and semi-arid conditions in the south (Schwerdtfeger, 1976). This first-order global atmospheric circulation pattern was established at least since the early Cenozoic (Parrish et al., 1982) or the Mesozoic (Hartley et al., 1992) but was altered by the uplift of the Central Andes (*e.g.*, Campetella and Vera, 2002; Insel et al., 2010).

The present-day climate along and across the Andes exhibits strong climatic gradients and seasonality due to the combined effects of latitudinal position, continentality, rain shadow and cold oceanic upwelling (e.g., Schwerdtfeger, 1976; Lenters and Cook, 1995; Houston and Hartley, 2003) (Fig. 5). The interference of the Andes with the prevailing wind systems creates the 'Arid Diagonal' (De Martonne, 1925; Gourou and Papy, 1966) that separates the northern and central Andes, which receive high precipitation on the eastern flank due to the South American Monsoon in austral summer, from the southern Andes, which are characterized by winter precipitation associated with the mid-latitude storm tracks or Westerlies (Schwerdtfeger, 1979; Lenters and Cook, 1995; Garreaud, 2007).

The South American Monsoon system is a major feature of the South American climate and forms in response to seasonal changes in the thermal contrast between the South American continent and the adjacent Atlantic Ocean (e.g., Zhou and Lau, 1999; Nogués-Paegle et al., 2002; Vera et al., 2006; Marengo et al., 2012). In austral summer, the South American Monsoon system is characterized in the upper levels by the “Bolivian high”, centered at 15°S, 65°W, and the “Nordeste through” over northeast Brazil (Lenters and Cook, 1997; Lenters and Cook, 1999). The South Atlantic Convergence Zone (SACZ) delineates a zone of cloudiness and precipitation that extents from the southern Amazon towards southeast Brazil and the adjacent Atlantic Ocean (Kodama, 1992; Lenters and Cook, 1999; Carvalho et al., 2004) (Fig. 5A). At low level, the easterly trade-winds transport high amounts of moisture from the tropical Atlantic Ocean and the Amazon Basin to the west. When encountering the Andes, the moisture-bearing winds are deflected southward into the Chaco Low via the South American low-level jet (Saulo et al., 2000; Nogués-Paegle et al., 2002; Marengo et al., 2004), which locally results in more than 1000 mm/yr of precipitation at the eastern flank of the Central Andes during austral summer (Fig. 5A). In austral winter, the zone of high precipitation migrates northwestward towards the equator (Vera et al., 2006). Precipitation on the eastern flank of the Andes is scarce and mainly related to northward incursions of the Westerlies (Vuille and Ammann, 1997) (Fig. 5B). In contrast, the Atacama Desert located between 5° and 27°S west of the Andes exhibits hyperarid conditions with mean annual precipitation <20 mm. Precipitation in the arid Altiplano-Puna plateau and intermontane basins to the east of the Puna is less than 200 mm/a and strongly variable throughout the year (Hijmans et al., 2005)

(Fig. 5). South of 35°S, the mean annual rainfall is controlled by the mid-latitude storm-tracks that bring moisture from the Pacific to the western side of the Andes, whereas the eastern side of the Andes receives only little rain due to the orographic barrier effect (e.g., Schwerdtfeger, 1976, Lenters and Cook, 1995). Because the latitudinal band of maximum precipitation associated with the Westerlies shifts from 45-55°S in summer to 35-45°S in winter (Garreaud, 2009), the region between 27° and 37°S shows strong seasonal variations and defines a transitional zone from a semi-arid climate with average rainfall of around 30 mm/a in the north to a Mediterranean climate with average rainfall of around 1000 mm/a in the south (Fig. 5).

4.2. Paleoclimate of the Central Andes

Modelling results from Ehlers and Poulsen (2009) and Insel et al. (2010) suggest that the emergence of the Andes above half of their present height may have resulted in increased precipitation along the eastern flanks and the central plateau, whereas hyperarid conditions replaced the semi-arid to arid conditions that prevailed since the Mesozoic in the Atacama Desert (Hartley et al., 1992; Dunai et al., 2005; Hartley et al., 2005; Le Roux, 2012; Oerter et al., 2016). The onset of Antarctic Bottom Water formation, the growth of the East Antarctic Ice Sheet and the resulting intensification of cold water upwelling along the Pacific Coast during the middle Miocene possibly contributed to the increasing aridity on the western side of the Andes (Houston and Hartley, 2003, and references therein). Sedimentologic, geomorphologic, pedogenic and isotopic data suggest that this change to hyperaridity occurred in the middle Miocene at about 12 Ma (Riquelme et al., 2007; Nalpas et al., 2008; Evenstar et al., 2009; Rech et al., 2010; Jordan et al., 2014; Rech et al., 2019) and was interrupted by several arid and semi-arid stages in the higher elevated regions of the western

Andean margin (Sáez et al. 2012; Jordan et al., 2014). The middle Miocene also marks the onset of deep canyon incision on the western Andean slope in northern Chile that are either linked to these climatic changes (García et al., 2011; Cooper et al., 2016) or to surface uplift related to westward tilting of the forearc (*e.g.*, Farías et al., 2005; García and Hérail, 2005; Hoke et al., 2007).

Starting in the Eocene to the Oligocene and throughout the Miocene, widespread, diachronous uplift of individual ranges in the Puna started to disconnect fluvial systems from the foreland and led to the establishment of internally drained basins in a semi-arid environment (see Strecker et al., 2007 for a review). Arid conditions were finally established in the late Miocene, when the Eastern Cordillera had built sufficient topography to block moisture transport towards the Puna plateau (Coutand et al., 2006). To the east, structurally similar basins in the Eastern Cordillera, Santa Barbara province and Sierra Pampeanas alternated between internal drainage conditions and open drainage to the foreland (Hilley and Strecker, 2005; Strecker et al., 2007). In the late Miocene (~9 Ma; Coutand et al., 2006), the sedimentary deposits in these intermontane basins mark a drastic shift from a (semi-)arid climate to fluvial conditions characterized by floodplains, lakes and swamps that support an important flora and fauna (Starck and Anzótegui, 2001). Higher moisture availability during the late Miocene is also indicated by the appearance of authigenic clays in paleosoils in the intermontane Santa María valley (Sierra Pampeanas) (Kleinert and Strecker, 2001), and from stable isotope data in pedogenic carbonates, leaf wax and volcanic class in the intermontane Angastaco Basin (Eastern Cordillera) (Rohrmann et al., 2016). Contemporaneously, a change from (semi-)arid to more humid conditions is also observed in the Subandean zone from sedimentary facies analyses (Uba et al., 2005; Uba et al., 2007) and from a fourfold increase in the sedimentation rate in the foreland stratigraphy (Uba et al., 2007); although the latter can also be associated to tectonic processes. These widespread climatic changes observed in late Miocene sediments are commonly attributed to the establishment of efficient orographic barriers due to the uplift of the Altiplano-Puna plateau, Eastern Cordillera and basement blocks in the Sierra Pampeanas (e.g., Starck and Anzótegui, 2001; Coutand et al., 2006; Strecker et al., 2007). At present-day, the main source of moisture along the eastern side of the Andes is the LLJ which is a direct consequence of the interaction between the easterly trade-winds and the Andean mountain belt (Lenters and Cook, 1995; Campetella and Vera, 2002; Insel et al., 2010). It is thus likely that the topographic uplift resulted in the initiation or amplification of the South American monsoon and associated LLJ at around 10-7 Ma (e.g., Strecker et al., 2007; Mulch et al., 2010; Rohrmann et al., 2016). The onset of fluvial megafan deposits in the Subandean zone in the late Miocene (Horton and DeCelles, 2001; Uba et al., 2005), which can be attributed to a monsoonal climate (Leier et al., 2005), corroborates this interpretation. Finally, the eastward migration of deformation in the Pliocene resulted in the subsequent uplift of individual ranges that acted as local orographic barriers, which led to focused precipitation on their eastern flank and renewed aridification in the adjacent intermontane basins located to the west (*e.g.*, Strecker et al., 1989; Kleinert and Strecker, 2001; Sobel and Strecker, 2003; Coutand et al., 2006).

In the southern part of the study area and west of the drainage divide, Cenozoic continental deposits between 27-37°S are sparse and paleoclimate reconstructions rely mainly on paleoflora studies with poor data coverage (Villagrán et al., 2004; Gayó et al., 2005; Hinojosa, 2005). These reconstructions rely on the assumption that the paleoclimatic conditions can be inferred from the present-day environment of the closest living relative and are thus subject to high uncertainty. The paleobotanic analyses indicate a shift from a Paleocene-to-Eocene (sub-)tropical climate towards drier and colder conditions from the end of the Eocene to the early Miocene (Villagrán et al., 2004; Gayó et al., 2005; Hinojosa, 2005). The re-appearance of sub-topical flora (Hinojosa, 2005) and subtropical sea surface temperatures revealed by strontium isotopes of marine fossils (Nielsen and Glodny, 2009) suggest a warmer and more humid climate during the Mid-Miocene Climatic Optimum. On the eastern side of the Andes at these latitude, paleoclimatic evidence comes mainly from the basin stratigraphy of the foreland. Here, upper Cretaceous to Paleocene fluvial and lacustrine sediments were replaced by semi-arid conditions with ephemeral rivers and playa lake deposits in the Paleocene-Eocene (Fosdick et al., 2017). In the Oligocene to the early Miocene, arid conditions led to the establishment of extensive eolian dune fields that covered large parts of the foreland (Jordan et al., 2001a; Tripaldi and Limarino, 2005; Fosdick et al., 2017; Buelow et al., 2018). Clay mineralogy and isotope analyses of paleosoils from an intermontane basin adjacent to the Frontal Cordillera (Ruskin and Jordan, 2007) and the onset of fluvial and lacustrine deposits in the middle Miocene (Jordan et al., 2001a; Ciccioli et al., 2014; Buelow et al., 2018) finally record a shift to renewed semi-arid conditions with seasonal precipitation.

In general, the paleo-climate of the northern and central segments of our study area is strongly influenced by the rise of the Andean mountain belt that led to the establishment or intensification of the South American Monsoon on its eastern flank and to aridification on its western side (e.g., Strecker et al., 2007). The onset of glaciations in West Antarctica and the formation of the cold Humboldt current in the middle Miocene probably enhanced this aridification (Houston and Hartley, 2003 and references therein). This first-order climatic pattern was overprinted by several global cold and warm phases that correlate well with plate tectonic processes (*e.g.*, Zachos et al., 2001; Ruddiman, 2008). However, the sedimentary records used to reconstruct paleo-climates during the Cenozoic are often too incomplete and resolutions are too low to draw firm conclusions about possible feedbacks. One of the best studied climatic transition occurred during the Late Cenozoic, when the global climate cooled (Zachos et al., 2001) and evolved towards high-amplitude oscillating conditions expressed by interglacial-glacial cycles throughout the Plio-Pleistocene (Shackleton et al., 1984). Many studies suggest that Pleistocene glaciation has had a global impact on the topographic evolution, relief, valley shape and erosion rates in mountainous landscapes (*e.g.*, Molnar and England, 1990; Montgomery et al., 2001; Shuster et al., 2005, Egholm et al., 2009; Shuster et al., 2011; Herman et al., 2013). Hence, past glaciations could have significantly contributed to the exhumation history of the Central Andes and we therefore summarize below evidences of past glaciations observed in the study area.

4.2.1. Evidence of past glaciations

Glaciers can only grow if the ELA is lower than the maximum elevation. North of 27°S in the semi-arid to arid Andes, the current ELA is at an altitude of around 6000 m and the presence of glaciers is restricted to few volcanic edifices exceeding 6000 m (Clapperton, 1983). The ELA also shows a steep east-west gradient due to higher precipitation on the eastern flanks of the Andes (Clapperton, 1994; Klein et al., 1999; Haselton et al., 2002). Between 27° and 40°S, the ELA drops from 6000 m to 1500 m (Schwerdtfeger, 1976; Harrison, 2004) and the east-west ELA gradient is reversed south of 30°S due to the inversion of the dominant wind direction and induced precipitation pattern (Clapperton, 1994). Today, the northernmost glaciers influenced by Westerly precipitation are found up to 27°S (Amman et al., 2001).

Although evidence of glaciations are found throughout the Andes, most studies focused on the glacial record of Patagonia south of 40°S (*e.g.*, Clapperton, 1983; Clapperton, 1994; Harrison, 2004; Rabassa et al., 2005; Hein et al., 2017), where glaciation started around 7-4.6

Ma (Mercer and Sutter, 1982) and was followed by several glacial-interglacial cycles throughout the Plio-Pleistocene (Clapperton, 1983; Harrison, 2004). There is also considerable evidence for extensive late Pleistocene icefields and valley glaciers between 32° and 37°S on the western side of the Andes (Clapperton, 1994; Harrison, 2004; Zech et al., 2008; Charrier et al., 2019). Mapped and dated moraine deposits at 33 to 34.5°S show that valley glaciers have descended as low as 950-1300 m during the last glacial maximum (LGM) (Herrera, 2016; Charrier et al., 2019) and thus have covered large parts of the catchments. Furthermore, radiometrically dated volcanic layers indicate that most valley incision in the higher Andes west of the drainage divide has occurred during the Pleistocene, with incision rates between 1.2 and 2.8 km/Ma during the last 1 Ma (Farías et al., 2008). Glacial growth in this region likely responded to increased precipitation associated with intensified Westerlies and may have occurred before (35-40 ka) the global LGM (Zech et al., 2008; Zech et al., 2011). Evidence for higher precipitation before and during the LGM, between 40 and 17 ka, also comes from grain-size and clay mineral analyses in marine sediment cores offshore Chile at 27°S (Stuut and Lamy, 2004) and 33°S (Lamy et al., 1999) and from palynological, sedimentological and isotopic data from a lake core from Laguna Tagua Tagua at 34.5°S (Heusser, 1983; Valero-Garcés et al., 2005). On the contrary, drier conditions prevailed during the early to mid-Holocene warm phase (Lamy et al., 2001; Jenny et al., 2003; Stuut and Lamy, 2004; Valero-Garcés et al., 2005). These climatic changes might be attributed to shifts in the core zone of the Westerlies in response to sea surface temperature in the eastern South Pacific Ocean (e.g., Lamy et al., 2010).

Glaciations in the semi-arid Andes up to 27°S north were less developed and restricted to higher elevations, with late Pleistocene ELA's located around 4000 m and the lowest preserved terminal moraine reaching down to 3450 m (Amman et al., 2001; Harrison, 2004;

Zech et al., 2008). Several cirque and valley glaciations are also observed in the Altiplano-Puna and in the Sierra Pampeanas which advanced during periods of intensified monsoonal precipitation (*e.g.*, Haselton et al., 2002; Zech et al., 2008; Backer and Fritz, 2015; D'Arcy et al., 2019). Colder temperatures and increased moisture on the eastern flank of the Andes led to a significant drop-down in Pleistocene snowlines of 300 m in the Puna and 900 m in the Sierra Pampeanas (Haselton et al., 2002). The extent to which these glaciations have affected the topography in the Central Andes remains debated. Montgomery et al. (2001) highlighted a strong latitudinal correlation between mean mountain height and the position of the ELA. Rehak et al. (2010) investigated the influence of climate on relief in Chile between 15.5°S and 41.5°S and identified the region between 28°S and 35°S as a zone of high local relief (750 m) generated by glacial erosion during the Quaternary.

Precipitation modulates erosion and thus influences exhumation and sediment storage, recycling and transport out of the system. According to the sedimentary record, several climatic changes could have left a signal in the exhumation history of the Central Andes. The most important change occurred during the late Miocene, when the Andes reached elevations high enough to act as an orographic barrier and initiated the South American Monsoon system (*e.g.*, Strecker et al., 2007). This led to increased precipitation at the eastern mountain front and thus possibly to higher erosion rates in parts of the Eastern Cordillera, Santa Barbara system, Sierra Pampeanas and Subandean zone (*e.g.*, Horton and DeCelles, 2001; Starck and Anzótegui, 2001; Uba et al., 2007). In northern Chile during this time, hyperarid conditions were established (*e.g.*, Rech et al., 2010; Jordan et al., 2014) and deep canyon incision started (*e.g.*, Farías et al., 2005; García and Hérail, 2005; Hoke et al., 2007; García et al., 2011; Cooper et al., 2016). Furthermore, the mid-Pleistocene shift to a highly oscillating climate (Zachos et al., 2001) and the occurrence of Pleistocene glaciation in the

Central Andes (*e.g.*, Zech et al., 2008) possibly also led to increased exhumation rates in parts of the Central Andes that experienced colder and wetter conditions (*e.g.*, Aguilar et al., 2011).

5. Methods

5.1. New and compiled data

We collected 149 bedrock samples between 21.8 and 34.9°S latitude in the Chilean Andes that we analysed for AHe (119 samples; supplementary Table S1), ZHe (92 samples; supplementary Table S2) and/or AFT (52 samples; supplementary Table S3). Our sampling strategy was to increase spatial coverage where data was sparse, concentrating on the western side of the Andes. Three analysed samples out of these 149 samples were rejected for all thermochronometric systems (14NC98, CLRK3849, Clin3). The new data includes samples collected on elevation transects at six locations to define age-elevation relationships (AER): samples Clin22A-D (AER-a in Fig. 1), CLRK3864 and CLRK3866 to CLRK3868 (AER-c in Fig. 1), Clin10A-E, Clin12A-E, Clin16A-E, and Clin25A-D analysed for AHe (all profiles), AFT (Clin22A-D, Clin25A-D and CLRK3864/3865-3868) and ZHe (CLRK3864/3865-3868). Clin22A and Clin25A were additionally dated with the U-Pb method because they were collected from shallow Miocene intrusions with unknown crystallization ages (supplementary Table S4 and Fig. S5).

The laboratory procedures are detailed in the supplementary material. We use mean ages and their standard deviation for (U-Th)/He data representation and modelling. AHe single grain ages with a U concentration over the grain mass smaller than 2 ppm and/or high He uncertainty (> 15%) were rejected because of their low precision (supplementary Table S1). We also rejected AHe single grain ages with an age difference greater than 50% relative to the average age of the sample, if the other aliquots show consistent ages similar to AHe samples in their surroundings. Additionally, two AHe single grain ages were rejected because they were older than the remaining aliquots, which gave consistent ages, and older than their crystallization (CLRK3853, age difference > 17% from average age) or ZHe age (CLRK3864, age difference > 35% from average age). We rejected three samples that showed large age dispersions (1σ > 50% of average age; 14NC36, Clin3, CLRK3849), one sample that is significantly younger than its surroundings and whose grains have very low U concentrations (<2 ppm) and high He-uncertainties (14NC38), and one sample that was derived from a Porphyry deposit and whose age overlap with its crystallization and ZHe age (14NC98). Single ZHe grain ages were excluded if they overlap or are older than their crystallization age or if they have age differences greater than 50% relative to the average age of the sample. In total, seven ZHe samples were rejected due to magmatic cooling (14NC26, 14NC29, 14NC31, 14NC70, 14NC98, CLRK3849) and high age dispersion (Huasco87) (supplementary Table S2).

We calculated AFT central ages, χ^2 probability and age dispersion for apatite fission-track ages (supplementary Table S3). Although derived from igneous bedrock, nine samples failed the χ^2-test and were decomposed into age peaks using Binomfit (Brandon, 2002). We use the central age if the major age peaks are similar to the central age and comprise a fraction of grains greater than 75% and for sample 14NC06, which yields two populations with ages similar to the central age. Track lengths could only be measured for 14 of the 54 samples (supplementary Table S3). Of these, seven samples show bimodal track length distributions with mean track lengths between 12.2 and 14.2 µm and 1σ > 2 (Gleadow et al., 1986). One additional sample (CLRK3874) has a track length of 11.72 ± 1.4 µm but this value is based on 5 measured tracks only. Because all but one (Huasco54) of this seven samples pass the χ^2-test and because all central ages have relatively low 1σ uncertainty and are consistent with other thermochronological data (AHe, AFT, ZHe) in their surroundings, the samples were included in the inversion. We cannot guarantee that samples for which no track lengths could be measured are not partially reset and these samples might lead to an underestimation of the modelled exhumation rate at their locations. Five samples show low U concentrations ($\leq$ 16 ppm), high uncertainties ($1\sigma > 15\%$ of the central age), and low numbers of counted grains ($\leq$ 11) and were rejected. Furthermore, sample 14NC05 was rejected because it is older than its corresponding ZHe age, contains little U (5 ppm) and shows high uncertainty ($1\sigma = 14.8$ % of the central age). Seven samples are close (< 2 Ma, within standard deviation of the mean age) to their magmatic cooling age and were rejected to exclude data corresponding to magmatic cooling instead of exhumation-related cooling (*e.g.*, Murray et al., 2018).

Additionally, we compiled a total of 1177 AHe, AFT, ZHe and ZFT ages from previous studies in the Central Andes between 18° and 36°S (supplementary Table S5). Of those, 255 ages were rejected because they were either of poor quality (*e.g.*, less than 10 grains analyzed for AFT/ZFT), highly dispersed for AHe/ZHe (1σ differs for more than 100% or 20 Ma from the average) or samples failing the χ^2-test, unreset detrital samples (*i.e.*, ages older than or overlapping with their formation age) or partially reset samples that were reported as such in the literature. Additionally, we excluded 80 AFT, ZHe and ZFT ages that are, within standard deviation of the sample age, less than 2 Ma younger than the sample intrusion age to exclude data corresponding to magmatic cooling instead of exhumation-related cooling. This value is a conservative estimate for magmatic cooling (Murray et al., 2018). 30 of those samples are from volcanic or porphyry rocks or dykes, the remaining ones are from intrusive rocks of which most can be related to porphyry copper deposits and associated hydrothermal circulation (*e.g.*, Maksaev and Zentilli, 1999; Deckart et al., 2005; Farías et al., 2008; Maksaev et al., 2009). We also excluded 18 samples that are derived from or located close to hydrothermally altered rocks or hot springs.

Including our 238 accepted ages, 1062 thermochronological ages from 695 samples were used to constrain the exhumation rate history of the central-southern Central Andes (Fig. 6, supplementary Table S5).

5.2. Inversion of data into exhumation rate histories

We use the inversion method described in Fox et al. (2014) and modified by Herman and Brandon (2015) to model the rate of exhumation for the last 80 Ma in the central-southern Central Andes. In this method, the depth from the surface to the closure depth (z_c) is described as the integral of the exhumation rate, $\dot{e}$, from the cooling age, τ, to the present day, which is translated to logarithmic space to avoid negative exhumation rates:

$$z_c = \int_0^\tau \dot{e}\, dt \longrightarrow \zeta = \ln\left(\int_0^\tau \exp(\varepsilon)\, dt\right) \tag{1}$$

where $\zeta = \ln(z_c)$ and $\varepsilon = \ln(\dot{e})$. The model assumes monotonic exhumation histories and therefore does not account for reburial.

A thermal model that accounts for heat advection and the effects of topography is used to model the geothermal gradient and rock cooling histories. From the thermal histories, we derive the closure depth using Dodson's definition for the closure temperature, *i.e.*, the temperature at which the sample was at the time given by its apparent age (Dodson, 1973).

This inverse problem is weakly non-linear and can be solved using the non-linear least-squares method (*e.g.*, Tarantola, 2005). This is achieved by discretization of the integral in Equation 1 into fixed time intervals Δt:

$$\zeta = \ln\left(\sum_{i=0}^{\tau} \exp(\varepsilon_i) * \Delta t\right) \tag{2}$$

Similar to Fox et al. (2014), we impose the condition that ε is spatially correlated by defining an a priori model covariance matrix, $\boldsymbol{C_M}$. This matrix is constructed for all time intervals using the horizontal distance between the ith and jth data points, d, and a Gaussian correlation function,

$$C_M(i,j) = \sigma^2 exp\left(-\left(\frac{d}{L}\right)^2\right) \tag{3}$$

where L is a correlation length scale, d the distance between samples, and σ^2 is the a priori variance serving primarily as a weighting factor. This covariance matrix enables, but does not impose, that data close to each other share a common exhumation history. Finally, a second non-linearity is implied because both the temperature field and closure depth calculations depend on the solution, *i.e.*, on the estimated erosion rates (Fox et al., 2014). The non-linear problem is solved using the steepest descent algorithm (Tarantola, 2005 (p.70)),

$$\varepsilon_m = \varepsilon_{m+1} - \mu\left(C_M G^t C_D^{-1}(\zeta_m - \zeta_{tm}) + \left(\varepsilon_m - \varepsilon_{prior}\right)\right) \tag{4}$$

where m is the iteration number, ε_{prior} is the logarithm of our initial guess of the erosion rate $\dot{e}_{prior}$, $\boldsymbol{C_D}$ is the data covariance matrix, μ is an *ad hoc* parameter chosen by trial and error that controls how rapidly the model parameters change, $\boldsymbol{\zeta_{tm}}$ is the logarithm of the closure depth computed with the thermal model, and $\boldsymbol{G}$ is obtained by computing the derivatives of $\ln(\sum_{i=0}^{\tau} \exp(\varepsilon_i)*\Delta t)$ with respect to ε (Herman and Brandon, 2015).

The model and data covariance must be chosen to minimize trade-off between model and data variance, σ_d^2 (*e.g.*, Aster et al., 2011). We start the iterative process by assigning the a priori expected value of the exhumation rate, $\dot{e}_{prior}$, and a final prior geothermal gradient, G_0. As any Bayesian inversion problem (*e.g.*, Tarantola, 2005), the model solution depends on the initial $\dot{e}_{prior}$ since it remains part of the solution (Equation 4) (Fox et al., 2014; Herman et al., 2013; Jiao et al., 2017; Willett et al., subm.). This dependency is more pronounced when data have poor resolution capacity. Similarly, the model also depends on our choice of G_0 due to the strong coupling between the geothermal field and the exhumation rate. In particular, higher geothermal gradients lead to shallower closure depths and thus to less exhumation. Higher exhumation rates increase the geothermal gradient because heat is more efficiently advected towards the surface. We run our model for two different $\dot{e}_{prior}$ values (0.1 and 0.5 km/Ma) and geothermal gradients G_0 (25 and 50 °C/km) to test the robustness of our results. The tested $\dot{e}_{prior}$ values are endmember values for regions that show very low Cenozoic exhumation rates like the Atacama Desert (< 0.2 km/Ma; Avdievitch et al., 2018) and regions that show higher exhumation rates like the southwestern Puna plateau (0.3 km/Ma to >1 km/Ma; Carrapa et al., 2005; Carrapa and DeCelles, 2008) or the southern Eastern Cordillera (0.1 to 0.6 km/Ma; Coutand et al., 2006; Deeken et al., 2006). The choice of G_0 and the length of time the model is run, *i.e.*, 80 Ma, set the final geothermal gradient at the end of the prior model. We adjust the initial geothermal gradient G_{ini} at 80 Ma to generate final geothermal gradients at the end of the prior model (G_0) of 25 and 50 °C/km, respectively, under $\dot{e}_{prior}$ values of 0.1 and 0.5 km/Ma. For example, a G_{ini} of 22.3 °C/km and running the model for 80 Ma with an $\dot{e}_{prior}$ of 0.1 km/Ma leads to a final prior geothermal gradient G_0 of 25 °C/km in the most recent time step. Because the geothermal gradient is influenced by heat advection, an $\dot{e}_{prior}$ of 0.5 km/Ma requires a smaller G_{ini} (14.5 °C/km) to get the same final prior geothermal gradient G_0 as in the inversion with an $\dot{e}_{prior}$ of 0.1 km/Ma. Similar G_0's for the different $\dot{e}_{\mathrm{prior}}$ values are important to allow investigating the influence of the $\dot{e}_{\mathrm{prior}}$ on the modelled exhumation rates. Finally, the modelled geothermal gradients in the most recent timestep (i.e., as constrained by the modelled exhumation rates) should be comparable to observed modern geothermal gradients in the Central Andes. A G_0 of 25 °C/km and a time length of 80 Ma leads to modelled geothermal gradients in the range of 24-34 °C/km ($\dot{e}_{prior}$ = 0.1 km/Ma) and 16-49 °C/km ($\dot{e}_{prior}$ = 0.5 km/Ma) for the last timestep. These values are consistent with most heat flow measurements of the Central Andes apart from the Coastal Cordillera, although few data are available (Springer and Förster, 1998; Höfer-Öllinger and Millen, 2010; Ege et al., 2007) (supplementary Fig. S4). Nevertheless, because many data especially in the southern segment were sampled closer to the magmatic arc and thus in areas with geothermal gradients up to 70 °C/km, we also test for a G_0 of 50 °C/km. Such a high final prior geothermal gradient results in modelled present-day values between 46-60 °C/km ($\dot{e}_{prior}$ = 0.1 km/Ma) and 31-75 °C/km ($\dot{e}_{prior}$ = 0.5 km/Ma), which are significantly higher than observed in the Central Andes.

To assess the solution, we compute the reduced variance which is the ratio between the a posteriori and a priori variance. The reduced variance ranges from 0 to 1 and is an indication of whether the solution has improved by incorporating data or not. The closer to zero, the better the solution is. We set the ratio between the a priori variance and a priori exhumation rate in logarithmic space equal to 7 for all inversions. This relatively high value permits more variation in the inverse solution and improves the fit to the data (Fox et al., 2014).

The use of the correlation structure $C_M(i,j)$ was recently criticized by Schildgen et al. (2018) who argue that the increase in late Cenozoic exhumation rates observed in modelled thermochronological data (Herman et al., 2013; Fox et al., 2015) are a result of a spatial correlation bias due to data correlation across faults. Willett et al. (subm.) reviewed the analysis of Schildgen et al. (2018) to identify the source of this discrepancy. They found that Schildgen et al (2018) made a series of errors, including incorrect construction of models, application of a biased operator to post-process Herman et al.'s (2013) results, and incorrect interpretations of both tectonic kinematics and how important these are to the resolving capability of thermochronometric data. These errors in Schildgen et al (2018) combined to create the appearance of an error in the original analysis of Herman et al. (2013) that does not exist. A spatial correlation may smooth exhumation rates across fault boundaries but does not impose a common history of correlated data. To demonstrate this, we test our model for different correlation length scales (10, 20 and 30 km) and provide model runs in which the study area is split into fault blocks that are independent from each other (*i.e.*, no correlation between data in different blocks) using the same set of parameters ($\dot{e}_{prior}$ = 0.1 km/Ma; G_0 = 25°C/km). The inversions with fault blocks are tested for correlation length scales of 20 and 1000 km for data located within the same block. In total, we provide eight inversions to test different combinations of G_0 and $\dot{e}_{prior}$ values (four inversions) and to explore the importance of the correlation length scales (2 inversions) and fault blocks (2 inversions). Each inversion is run for 80 Ma, which is the approximate onset of compressional deformation in the Central Andes (Fig. 3). Therefore, only thermochronological ages younger than or equal to 80 Ma are used in the inversions (837 ages). Finally, past and present geothermal gradients are unknown in most parts of the Central Andes. We thus compare our modelled exhumation rates with rates derived from age-elevation profiles at 3 locations, which provide independent constrains on exhumation rates (*e.g.*, Wagner et al., 1979; Gleadow and Fitzgerald, 1987; Fitzgerald et al., 1995), although Fox et al. (2014) showed that exhumation rates are robust with respect to the thermal model where data constrain exhumation rates due to age elevation relationships.

6. Results

6.1. Thermochronological ages

In the following section, we first analyse how the compiled thermochronological ages vary in time and space, including new and previously published ages (Fig. 6, supplementary Table S5). Whereas the Western/Principal Cordillera (348 ages), the Sierra Pampeanas (277 ages), and the Coastal (124 ages), Eastern (93 ages) and Frontal (105 ages) Cordilleras are relatively well covered with data, the other tectonomorphic units contain a maximum of 42 ages (Fig. 1, Fig. 6). Furthermore, more data are available in the western part of the orogen than in the east, where data density is high only at 21°S and in the southern Eastern Cordillera and northern Sierra Pampeanas. The absence of a certain age population in tectonomorphic structures where only few ages were dated can thus simply be a sampling bias.

We split the compiled data set along the main drainage divide to account for the climatic gradients that are opposite on the western and eastern sides of the Andes (Fig. 7, Fig. 8). Data from the internally draining Altiplano-Puna plateau are merged with data in the west. Relative frequencies of the age distributions for the western and eastern sides of the Andes are shown in the supplementary Fig. S1. Furthermore, we provide latitudinal cross-sections for the northern, central and southern segments to account for their different tectonic settings (Fig. 9). In the data description hereafter, the numbers in brackets represent the number of samples in a given tectonomorphic or temporal unit.

6.1.1. Data to the west of the main drainage divide

Figure 7 shows the 586 thermochronological ages that are located to the west of the drainage divide. A major feature is the significant drop in ages south of ca. 32°S observed in all four thermochronological systems.

North of 32°S, the distribution of the AHe and AFT ages share many similarities and therefore we describe them here together. The AHe (226) and AFT (147) ages range from 10 to 109 Ma and from 16 to 198 Ma, respectively (Fig. 7, supplementary Fig. S1 A and Table S5). Both systems have one exception located at 30°S in the Frontal Cordillera at 2050 m elevation with an AHe age of 6.9±0.6 Ma and an AFT age of 8.4±0.8 Ma (Rodríguez et al., 2018). Palaeocene and older ages are a minor fraction (23 AHe and 30 AFT ages). They are mainly located in the Coastal Cordillera (16 AHe and 17 AFT) and are rare and scattered from the Central Depression to the Puna Plateau. The majority of ages are Eocene to Oligocene (148 AHe and 108 AFT ages) and mostly located in the Principal Cordillera (94 AHe and 65 AFT ages), common in the Frontal Cordillera (11 AHe and 28 AFT ages) and sparse elsewhere. Miocene ages (56 AHe and 9 AFT ages) are common in the Frontal (19 AHe and 4 AFT ages) and Principal/Western Cordilleras (31 AHe and 2 AFT ages) but are sparse in the Coastal Cordillera and Puna plateau.

South of 32°S, the AHe ages (36) range from 0.5 to 35 Ma (Fig. 7, supplementary Fig. S1 B). Only four ages are Oligocene. These are located close to 32°S in the Coastal (2) and Principal (2) Cordilleras. The remaining AHe ages are all located in the Principal Cordillera. Miocene ages (9) are located closer to the mountain front, whereas most Plio-to-Pleistocene ages (23) are located closer to the drainage divide. The AFT data (50) range from 1.9 to 51 Ma. They show a minority of Eocene ages in the Principal (5) and Coastal Cordilleras (4), one early Miocene age in the Central Depression, and a large majority of ages (40) younger than 13 Ma located in the Principal Cordillera. Sixteen samples are Plio-Pleistocene in age.

ZHe ages north of 32°S (107) range from 31 to 221 Ma (Fig. 7, supplementary Fig. S1 A). Pre-Cretaceous ages (6) range between 150 and 221 Ma and are located in the Principal (5) and Frontal (1) Cordilleras. Cretaceous ages (51) are found in the Coastal Cordillera (27), the Principal (11) and Frontal Cordilleras (10), the Puna plateau (2), and the Central Depression (1). The remaining ages are Paleogene (50) and located in the Principal (34), Frontal (13), and Coastal (3) Cordilleras. South of 32°S, the Principal Cordillera yields Miocene (3) to Pliocene (3) ZHe ages between 13 and 2.8 Ma (Fig. 7, supplementary Fig. S1 B).

Only thirteen ZFT samples located west of the Andean crest remained after excluding ages that represent magmatic cooling ages, non-reset detrital ages, or samples that were most likely hydrothermally altered (supplementary Table S5). Among the accepted samples, six are located north of 32°S (Fig. 7). They show Triassic ages in the Western/Principal Cordillera and Cretaceous ages in the Coastal Cordillera. South of 32°S, all ZFT samples are located in the Principal Cordillera (7). One age is Late Cretaceous, three ages are late Paleocene to Eocene and three are middle to late Miocene (Fig. 7).

In summary, the majority of the thermochronological ages west of the Andean water divide and north of 32°S are Paleogene (Fig. 7 and supplementary Fig. S1 A). The few ZFT ages and the ZHe additionally show a major Cretaceous population. Among the Paleogene samples, AHe and AFT ages are predominantly Eocene to Oligocene whereas ZHe ages are mostly Paleocene to Eocene (supplementary Fig. S1 A). These ages are distributed from the Coastal Cordillera to the Western/Principal and Frontal Cordilleras to the Altiplano-Puna plateau. Miocene cooling ages, mostly AHe ages and few AFT ages, are mainly located in the Western/Principal and Frontal Cordilleras. Finally, pre-Cenozoic ages of all four systems, yet frequently recorded by the ZHe system, are common in the Coastal Cordillera but are also present in other units. Ages south of 32°S are significantly younger than in the north (Fig. 7, supplementary Fig. S1 B). Almost all ages are located in the Principal Cordillera. Plio-Pleistocene to Miocene ages prevail, whereas pre-Cenozoic ages are only observed in the ZFT system.

6.1.2. Data to the east of the drainage divide

East of the Andean range crest, the quantity of data (476) is lower than to the west (Fig. 6). Data are dense in the northern segment along a cross-section at 21°S in the Eastern Cordillera and Inter- and Subandean zones as well as in the southern Eastern Cordillera and the northern Sierra Pampeanas, whereas they are sparse in the Frontal Cordillera, Precordillera and eastern Principal Cordillera in the middle and central segments (Fig. 1). Unlike to the western side of the orogen, no clear spatial pattern is observed along a north-south transect (Fig. 8). Young AHe ages are present all along the eastern margin of the orogen. AFT and ZHe ages are youngest between 27° and 28°S .

As observed to the west of the drainage divide, the spatial distribution of the AHe and AFT ages east of the divide share some similarities and are thus described together. AHe ages range from 1.6 to 294 Ma (206 samples) and AFT ages from 2.6 to 270 Ma (203 samples) (Fig. 8, supplementary Fig. S1 C). The majority of Pre-Cenozoic AHe (56) and AFT ages (70) are located in the Sierra Pampeanas. The remaining Pre-Cenozoic ages are located in the Frontal (4) and Eastern Cordilleras (1) for AHe and scattered in the foothills of the Precordillera (6), the Subandean zone (2) and the foreland close to Malargüe (1) for AFT. Paleogene ages (40 AHe and 43 AFT) include a majority of mid-Eocene to Oligocene ages particularly dense in the Sierra Pampeanas and Santa Barbara range (27 AHe and 16 AFT) and in the Eastern Cordillera (6 AHe and 20 AFT). The rest are scattered among the Puna (5 AFT), Interandean zone (4 AHe) and Frontal Cordillera (3 AHe and 2 AFT). Miocene ages (89 AHe and 65 AFT) are distributed over most tectonomorphic units of the eastern side of the drainage divide and are most frequent in the Eastern Cordillera (25 AHe and 20 AFT), Sierra Pampeanas (26 AHe and 20 AFT) and Interandean zone (20 AHe and 15 AFT). The rest are found in the Subandean zone (6 AHe and 1 AFT), southern Frontal Cordillera (7 AHe), Puna (3 AFT), Precordillera (2 AFT) and in the Principal Cordillera (3 AHe and 2 AFT) and adjacent foreland (2 AHe and 2 AFT). Pliocene ages (18 AHe and 16 AFT) are mostly observed in the Sierra Aconquíja (5 AHe and all 16 AFT) and the Sierra de Valle Fértil (2 AHe), which are part of the Sierra Pampeanas, and in the Subandean zone (7 AHe). The remaining AHe are scattered at the southern margin of the Eastern Cordillera (2 AHe), in the Interandean zone (1 AHe) and in the Principal Cordillera (1 AHe). Pleistocene data include only three AHe ages located in the Sierra de Valle Fértil (1) and Fiambalá Basin (1) of the Sierra Pampeanas and in the Subandean zone (1) (Fig. 8).

Among the ZHe ages, which range from 9.4 to 378 Ma (64 ages), the majority are pre-Cenozoic (46) and mainly derived from the Sierra Pampeanas (37) (Fig. 8, supplementary Fig. S1 C). The remaining pre-Cenozoic ages are from the Eastern Cordillera (6), Interandean zone (1) and Frontal Cordillera (2). Cenozoic ages (18) are mainly Eocene to Oligocene (16). These are most abundant in the Eastern Cordillera (11) and few are derived from the Sierra Aconquíja in the Sierra Pampeanas (3), Interandean zone (1) and Frontal Cordillera (1). Two ages from the Sierra Aconquíja in the Sierra Pampeanas are Miocene.

There are only three ZFT ages in our compilation. These are located in the Eastern Cordillera (2) and Principal Cordillera (1) and yielded Upper Jurassic to Lower Cretaceous ages (Fig. 8).

In summary, the eastern dataset shows younger thermochronological ages compared to the western data set north of 32°S and a larger spread of ages (Fig. 7, Fig. 8, supplementary

Fig. S1 A,C). Pre-Cenozoic ages mainly occur in the Sierra Pampeanas and are abundant in all four thermochronometric systems. Paleogene and Miocene ages from the AHe, AFT and ZHe systems are distributed within most tectonomorphic units, although data are sparse in the Frontal and Principal Cordilleras, Precordillera and the Altiplano-Puna (Fig. 1). Pliocene ages are restricted to the AFT and AHe systems (Fig. 8). They are found commonly in the Subandean zone and the Sierra Pampeanas and only locally at the southern margin of the Eastern Cordillera, Interandean zone and Principal Cordillera. Pleistocene ages are sparse and only observed among the AHe data from the Sierra Pampeanas and the Subandean zone.

6.1.3. Latitudinal age distribution

Figure 9 shows the data distribution across the Andes in four latitudinal cross-sections. Thermochronological AHe and AFT ages in the cross-section between 18° and 23.5°S show an eastward decreasing age trend that is particularly important in the AHe system for the Inter- and Subandean zones (Fig. 9A). A similar trend can be observed in the cross-section between 23.5° and 28°S in the AHe, AFT and ZHe systems that show much younger ages and a wider age range in the northern Sierra Pampeanas (including the Fiambalá Basin) and the southern Eastern Cordillera than the data located to the west, which are all older than 10 Ma (Fig. 9B). The central segment between 28 and 32°S has less data and ages on the eastern side are restricted to the Sierra Pampeanas. AFT and ZHe ages are younger on the western side, whereas AHe ages are young on both side of the orogen and especially in the Sierra de Valle Fértil located in the Sierra Pampeanas (Bense et al., 2013; Ortiz et al., 2015) (Fig. 9C). Finally, the southern segment between 32° and 36°S shows significantly younger ages and a much wider spread of ages in the west compared to the east (Fig. 9D).

In summary, most ages in our database are Eocene to Miocene (643 ages). Plio-to Pleistocene ages (79) are common in three areas: in the Subandean zone and the Sierra

Pampeanas (especially in the Sierra Aconquíja) east of the drainage divide and in the southern Principal Cordillera west of the drainage divide.

6.2. Inversion of ages to exhumation rate histories

In this section, we first describe the inversion results for the exhumation rate history of the Central Andes for selected time intervals using a correlation length scale of 20 km, an $\dot{e}_{prior}$ of 0.1 km/Ma and a G_0 of 25 °C/km (Fig. 10, Fig. 11). The erosion rates mentioned in this section are specific for this set of parameters. This is because the prescribed G_0, and to a lesser extent the $\dot{e}_{prior}$ value and the correlation length scale, directly influence the magnitude of the modelled exhumation rates (Sec. 6.2.2). Yet the general pattern (i.e., acceleration, deceleration) stays the same for all inversions (supplementary material, movies InversionA-H). Furthermore, Fox et al. (2014) emphasized the importance of the reduced variance and temporal resolution when analyzing the inversion results. Because resolution degrades back in time, more recent stages of the model are better resolved than earlier stages, in which changes in exhumation rates can only be captured where multiple thermochronometers are available. Movies showing the complete exhumation rate histories since 80 Ma are provided in the supplementary material for all eight inversions.

6.2.1. Exhumation rate history of the Central Andes

6.2.1.1. Northern segment (18 - 28°S)

The exhumation rate history before 36 Ma is poorly constrained, as indicated by a reduced variance close to 1 in most parts of the Central Andes (Fig. 11A,B). Only the western flank of the Andes and parts of the Sierra Pampeanas, Eastern Cordillera and Interandean zone are partially resolved and show some constraints on the exhumation rates. These are mainly around 0.1 km/Ma between 60 and 36 Ma (Fig. 10A,B and supplementary movie, InversionA).

Such low exhumation rates prevail on the western side of the Andes during the whole modelled time period apart from localized zones in the Western Cordillera that show slightly higher (≤ 0.2 km/Ma) rates: A pulse of exhumation migrates from the south (28°S) to the north (26°S) between 50 and 38 Ma (Fig. 10B), and some localized spots show higher Miocene exhumation rates compared to their surroundings (Fig. 10G).

During the Late Cretaceous to the Paleocene, exhumation on the eastern side of the Andes occurs only in the northern Sierra Pampeanas with low rates (0.1 km/Ma) (Fig. 10A). By the middle to late Eocene, exhumation starts locally in the Eastern Cordillera and the Altiplano-Puna plateau (Fig. 10B) and subsequently affects larger parts of these regions and the north-western Sierra Pampeanas during the Oligocene (Fig. 10C,D). Exhumation rates remain smaller than 0.2 km/Ma until the middle Miocene. In the early Miocene, the Interandean zone starts exhuming with rates < 0.15 km/Ma (Fig. 10E,F). Reduced variances <1 in the Eastern Cordillera at 22°S and the western Sierra Pampeanas indicate that the solution in these parts is now reasonable constrained by thermochronological data (Fig. 11E,F). During the late Miocene, exhumation accelerates up to ca. 0.25 km/Ma in parts of the Eastern Cordillera, western Puna margin and Interandean zone and propagates eastwards into the eastern part of the southern Eastern Cordillera and into Subandean zone (Fig. 10G-K). Exhumation rates in the eastern Interandean zone and the Subandean zone increase from <0.2 km/Ma before 6 Ma to ca. 0.6 km/Ma in the Pleistocene (Fig. 10H-K). Plio-Pleistocene increases in exhumation rates are also observed locally in the northern Sierra Pampeanas, namely in the Fiambalà Basin and the Sierra Aconquíja. In the latter, rates increase from <0.1

km/Ma before 6 Ma (Fig. 10H) to about 1.5 km/Ma in the Pleistocene (Fig. 10K). This region shows the highest rates observed in the northern segment of the Central Andes.

6.2.1.2. Central segment (28 - 32°S)

Exhumation rates west of the drainage divide in the central segment show a similar pattern as the northern segment. Until the middle Miocene, exhumation rates in the Principal and Frontal Cordilleras vary around 0.1 to 0.13 km/Ma (Fig. 10A-F). Between ca. 10 Ma to 6 Ma, exhumation rates in the Frontal Cordillera constantly increase and reach values up to 0.25 km/Ma at 30°S (Fig. 10G,H). On the eastern side, only few thermochronological data are available that are restricted to the Sierra Pampeanas. There, exhumation rates are low (< 0.1 km/Ma) with the exception of the Sierra de Valle Fértil that starts exhuming during the Pliocene and shows exhumation rates of ca. 0.75 km/Ma in the last 2 Ma (Fig. 10I,K).

6.2.1.3. Southern segment (32 - 36°S)

In the Central Andes south of ca. 32°S on the western side of the drainage divide, most pre-Miocene ages are located in the Coastal Cordillera or close to the mountain front in the Principal Cordillera. In this zone, a first exhumation signal is observed in the early Eocene and low exhumation rates (~0.1 km/Ma) prevail until the late Miocene (Fig. 10A-F). However, data are sparse and the solution is not well resolved (Fig. 11A-F). After 12 Ma, exhumation is recorded in most parts of the Principal and Frontal Cordilleras with a better resolution (Fig. 10G, Fig. 11G). Exhumation rates on the western side increase from <0.15 km/Ma in the latest Miocene (Fig. 10H) to ca. 0.25 km/Ma in the Pliocene (Fig. 10I) and to more than 2 km/Ma in the Pleistocene (Fig. 10K). These are the highest exhumation rates observed in the Central Andes. On the eastern side of the Andes, exhumation rates in the Frontal and Principal

Cordilleras and in the Malargüe fold-and-thrust belt accelerate relatively continuously from ca. 0.15 km/Ma in the late Miocene to ca. 0.4 km/Ma in the Pleistocene (Fig. 10G-K).

6.2.2. Influences of the model parameters on the inversion results

To assess the influence of fault blocks, G_0, $\dot{e}_{prior}$ values and correlation length scales on the inversion result, we compare the exhumation rate histories and reduced variances for the 2-0 Ma time interval of the eight inversions (Fig. 12, Fig. 13). The misfit between observed and predicted ages and histograms of the age differences are provided in supplementary Figure S2.

The most significant influences on the modelled exhumation rates is exerted by our choice of the $\dot{e}_{prior}$ and G_0 (Fig. 12). Higher G_0's lead to lower exhumation rates because heat is more efficiently advected to the surface and thus the closure depths are shallower (Fig. 12B,D). Higher $\dot{e}_{prior}$ values instead lead to significantly higher exhumation rates because the $\dot{e}_{prior}$ stays part of the solution (Equation 4) (Fig. 12C,D). Thus, a higher geothermal gradient partly compensates for higher exhumation rates resulting from a high $\dot{e}_{prior}$, and therefore rates are highest in the inversion with an $\dot{e}_{prior}$ of 0.5 km/Ma and a geothermal gradient of 25 °C/km (Fig. 12C). These differences in exhumation rates are most important in fast exhuming places (*e.g.*, in the Inter- and Subandean zones, southern Principal Cordillera or Sierra Aconquíja), whereas in places where exhumation rates are low (*e.g.*, in the Western Cordillera) recovered rates are similarly low (and mainly below 0.2 km/Ma) in all inversions (Fig. 12). Different values of $\dot{e}_{prior}$ and G_0 do not influence the reduced variance if the correlation length scale remains the same (Fig. 13A-D). Instead, a smaller correlation length scale increases the reduced variance because the number of thermochronological data to infer exhumation rates at any given location is reduced (Fig. 13E). A larger length scale results in lower reduced variances and more spatial smoothing (Fig. 13F). Nevertheless, the exhumation rate magnitudes and patterns remain similar despite being less pronounced when a small correlation length scale is used (Fig. 12A,E,F).

The influence of fault blocks on the inversion results can be investigated by comparing Figure 12A (without faults) with Figure 12G (with faults), for which the same set of parameters was used ($\dot{e}_{prior}$ = 0.1 km/Ma; G_0 = 25 °C/km, L = 20 km). In the inversion with fault blocks, the spatial extent of the modelled exhumation rates (Fig. 12G) and reduced variances (Fig. 13G) is truncated at block boundaries because information of thermochronological data does not propagate into adjacent blocks, whereas the solution is smoothed across in the inversion without fault blocks (Fig. 12A, Fig. 13A). This is for example clearly observable along the western mountain front in the southern Principal Cordillera. However, these differences are rather local and exhumation rate magnitudes and patterns are similar in most places. Besides, regional differences in exhumation rates, which are an expression of spatially different thermochronological data, are equally recovered in several locations as for example at the boundary between the southern Eastern Cordillera and northern Sierra Pampeanas, the boundary between the Inter- and Subandean zones or in the Western Cordillera (Fig. 12A,G). Figure 12H shows the inversion for which fault blocks were combined with a correlation length scale of 1000 km, *i.e.* all data can be spatially correlated if located in the same fault block. Even with such a large correlation length scale, exhumation rates vary spatially in individual blocks (*e.g.*, in the southern Principal Cordillera and northern Sierra Pampeanas). Where data resolution is high, the magnitude and pattern of the modelled exhumation rates remain comparable to the inversion without fault blocks (Fig. 12A), although they are heavily smoothed.

6.2.3. Age-elevation profile analysis

The slope of an age-elevation profile is an approximation of the exhumation rate that is independent of the geothermal gradient (*e.g.*, Wagner et al., 1979; Gleadow and Fitzgerald, 1987; Fitzgerald et al., 1995) and thus enables us to validate our modelling results (Fig. 14). However, in such age-elevation relationships it is assumed that the isotherms are flat and that the samples have undergone an identical exhumation history (*e.g.*, Mancktelow and Grasemann, 1997). This assumption is often not valid because topography disturbs the geothermal field (*e.g.*, Mancktelow and Grasemann, 1997; Braun, 2002a,b). The temperature perturbation decreases exponentially with depth in proportion to the wavelength of the surface topography. The critical wavelength for this temperature disturbance can be approximated by the closure temperature divided by the geothermal gradient (Braun, 2002a,b). Assuming a geothermal gradient of 25 °C/km and a closure temperature of 70 °C (Farley, 2000) for AHe and 110 °C for AFT (Ketcham et al., 1999), the critical wavelength is 2.8 km for AHe and 4.4 km for AFT. We use three sites for the age-elevation analysis: two are located in the southern segment around 33.5°S latitude on the western (AER-a; this study) and eastern sides (AER-b; Riesner et al. (2019)) of the Andes, the third one is located in the Western Cordillera at 26.2°S (AER-c; this study) (see Fig. 1 and supplementary Table S5 for location and data). Because AER-b and AER-c were sampled over a larger horizontal distance (5.7 and 7.5 km) than the critical wavelength λ_c, the derived exhumation rates should be considered as maximum values (Braun, 2002b).

The age-elevation profile in the southern segment on the western side of the Andes (AER-a) consists of data between 1.24 ± 0.3 to 9.8 ± 1.0 Ma at elevations from 1559 to 2575 m (Fig. 14A). The AHe data show a break in slope that indicates an increase in the exhumation rate (*e.g.*, Wagner et al., 1979; Gleadow and Fitzgerald, 1987; Fitzgerald et al., 1995) from

0.15 ± 0.1 km/Ma before 2 Ma to 2.0 ± 3.7 km/Ma after 2 Ma. The linear fit to the AFT data indicates an exhumation rate of 0.54 ± 0.3 km/Ma between 7 and 10 Ma, which fits with the slower rate before 2 Ma in the AHe data. The two oldest AFT samples are close to their magmatic cooling age (10.2 ± 0.09 Ma; this study (supplementary Table S4)). However, the intrusion from which the samples were taken from is an isolated body of moderate size that was emplaced high in the crust and does not show any sign of multiple intrusive pulses and thus has cooled relatively quickly (Cornejo and Mahood, 1997). Therefore, these two ages probably represent cooling due to exhumation and can be used in the age-elevation relationship. Nevertheless, they were rejected in the inverse modelling since all thermochronological ages compiled for this study were treated uniformly (*i.e.*, at least 2 Ma younger than their intrusion age). The exhumation history as resolved by the age-elevation profile differs only partly from that derived from the inversion model (Fig. 14C). In the inversion, the reduced variance stays close to 1 before 15 Ma (Fig. 14E) indicating that the a posteriori rates are not resolved by the data. After 15 Ma, the modelled exhumation rates with $\dot{e}_{prior}$ = 0.5 km/Ma start to decrease from the prior value to ≤0.25 km/Ma at 8 Ma, whereas they start to increase slightly for the inversions with $\dot{e}_{prior}$ = 0.1 km/Ma (Fig. 14C). The observed decrease in exhumation rates for the inversions with an $\dot{e}_{prior}$ value of 0.5 km/Ma should thus be considered as an artefact caused by the transition from posterior rates unresolved by the data to rates resolved by the data. After 8 Ma, the reduced variance decreases significantly to values between 0.55 and 0.85 (Fig. 14E) due to the incorporation of the AFT data (Fig. 14A) and until 2 Ma all exhumation rates range between 0.08 and 0.26 km/Ma. At 2 Ma, the reduced variance drops below 0.1 and the rates increase abruptly to values between 0.65 and 0.74 km/Ma for G_0 set to 50 °C/km and between 1.43 and 1.62

km/Ma for G_0 set to 25 °C/km (Fig. 14C), which matches the slope of the age-elevation relationship. Different correlation length scales do not significantly influence the results.

The age-elevation profile on the eastern side of the orogen (AER-b) has much older AHe and ZHe ages than the profile on the western side (Fig. 14B) (Riesner et al., 2019). No AFT ages were available. AHe ages span the period between 10.5 ± 2.7 and 17.5 ± 6.2 Ma and the linear fit to this data indicates an exhumation rate of 0.07 ± 2.6 km/Ma. ZHe ages lie between 179 ± 12.4 and 227 ± 20.8 Ma and give an exhumation rate of 0.02 ± 0.01 km/Ma. These data are from a Permo-Triassic intrusion with poor age control (one whole rock K-Ar age of 234 ± 10 Ma; Gregori and Benedini 2013 and references therein) and the oldest two ZHe ages may represent magmatic cooling ages. The ZHe ages were not incorporated in the inverse model because only ages younger than or equal to 80 Ma were used. The modelled exhumation rates (Fig. 14D) and reduced variances (Fig. 14F) at this location show a first signal at 80 Ma due to the influence of pre-Cenozoic AHe ages in the surrounding area in the Frontal Cordillera. This is especially important for the inversions with $\dot{e}_{prior}$ values of 0.5 km/Ma for which erosion rates drop below 0.25 km/Ma (Fig. 14D). The decrease is a direct consequence of the choice of the $\dot{e}_{prior}$ and occurs when the model starts to adjust to rates constrained by thermochronological data. However, the reduced variance stays close to 1, indicating poor data resolution (Fig. 14F). By 42 Ma, exhumation rates of all inversions are similar and smaller than 0.15 km/Ma (Fig. 14D). Between 18 and 16 Ma, the exhumation rate history starts to be constrained by the AHe data along the age-elevation profile, which results in a drop of the reduced variance to 0.72-0.96 (Fig. 14F). The reduced variance stays around these values until 10 Ma, indicating that the solution in these time intervals is better constrained. All but one inversions show exhumation rates that steadily increase from below 0.1 km/Ma before 18 Ma to values between 0.15 and 0.6 km/Ma at 2 Ma. In the last time interval, the reduced variance drops again below 0.8 due to the additional constraint that the samples need to be exhumed to the surface. In the time interval covered by the thermochronological data (10-18 Ma), the exhumation rates of most inversions (0.06 to 0.17 km/Ma) are consistent with the rates derived from the AHe age-elevation relationship (0.07 ± 2.6 km/Ma).

A third age-elevation profile from the Western Cordillera (AER-c) also shows a good fit with the inversion results (supplementary Fig. S3). Here, ZHe, AFT and AHe data constrain the time period between 110 and 33 Ma in the age-elevation profile, giving exhumation rates of 0.01 ± 0.001 km/Ma ($\dot{e}_{ZHe}$), 0.03 ± 0.06 km/Ma ($\dot{e}_{AFT}$) and 0.2 ± 0.09 km/Ma ($\dot{e}_{AHe}$) that match well with the modelling results yielding rates between 0.04 and 0.2 km/Ma in the time interval covered by the data.

Taken together, the modelled exhumation rates are similar to the ones derived from age-elevation profiles at selected locations over the time intervals resolved by the data. Furthermore, all inversions show the same exhumation rate pattern (acceleration, deceleration) independently from the chosen parameters when data resolution is sufficient (*i.e.*, when the reduced variance < 1), but the magnitude of the rates varies strongly with G_0 and, to a lesser extent, the $\dot{e}_{prior}$.

7. Discussion

7.1. Influence of the $\dot{e}_{prior}$ and G_0 on modelled exhumation rates

The inversion of low-temperature thermochronological data requires to prescribe an a priori exhumation rate ($\dot{e}_{prior}$) and a priori covariance, which are both independent of the thermochronometric data (*e.g.*, Fox et al., 2014), and a final prior geothermal gradient G_0. Their influence can be tested by comparing inversion results with different sets of parameters or different correlation length scales (Fig. 12, Fig. 13) and by comparing the inversion solutions with age-elevation relationships at selected locations (Fig. 14, supplementary Fig. S3). Several conclusions can be drawn from these comparisons.

First, all tested cases converge toward similar exhumation rate histories that are consistent with the age-elevation relationships when data resolution is sufficient. At 33.5°S, all modelled exhumation rates increase significantly at 2 Ma west of the Andes (Fig. 14C) and moderately since 14 Ma on the eastern side of the orogen (Fig. 14D). The observed temporal variations of exhumation rate patterns (*i.e.*, acceleration, deceleration) are therefore independent of our prior model. This demonstrates the robustness of our approach.

On the other hand, the magnitude of the modelled exhumation rates strongly depends on G_0 and to a lesser extent on the $\dot{e}_{prior}$. Especially the model solution of the most recent time step shows a high dependency on the near surface geothermal gradient (Fox et al., 2014). This is expected for this interval as the youngest ages only provide an estimate of the exhumation from their closure depths to their present elevation, and the closure depth clearly depends on the geothermal gradient at the time of closure. In comparison, older ages in an age-elevation relationship constrain both the average exhumation since closure (which depends on the thermal field) but also the exhumation rate between the sample's age and the age of the sample directly below it in the profile. Therefore, parts of the model that are resolved by age-elevation relationships are less sensitive to the geothermal gradient than the youngest time step and time steps that are more recent than the youngest age. Furthermore, fast exhuming regions like the southern Principal Cordillera, the Sierra Aconquíja or the Subandean zone are more sensitive to the geothermal gradient (Fig. 12, Fig. 14C). This can be explained by the control of the exhumation rate on heat advection, which is elevated in case of faster exhumation rates.

Modelled exhumation rates in the southern Principal Cordillera (1.43 to 1.62 km/Ma; Fig. 14C) match better the rates derived from the age-elevation relationship (2.0 ± 3.7 km/Ma; Fig. 14A) under a G_0 of 25 °C/km, although the exhumation rate is still underestimated. Such an underestimation is expected because the age-elevation relationship approach assumes that the closure isotherm is flat and therefore tends to overestimate rates as the closure isotherm is likely to be perturbed by topography. A G_0 of 25 °C/km results in modern modelled geothermal gradients in the range of 24-34 °C/km ($\dot{e}_{prior}$ = 0.1 km/Ma) and 16-49 °C/km ($\dot{e}_{prior}$ = 0.5 km/Ma) (supplementary Fig. S4), which are consistent with most heat flow measurements of the Central Andes (Springer and Förster, 1998) and with present-day geothermal gradients from the Principal Cordillera (32-35°C/km; Höfer-Öllinger and Millen, 2010). Instead, a G_0 of 50 °C/km yields modern modelled geothermal gradients between 46 and 60 °C/km ($\dot{e}_{prior}$ = 0.1 km/Ma) that are significantly higher than the observed values. Thus, inversions using a G_0 of 25 °C/km are preferable over inversions with 50°C/km. This means however that the magnitude of modelled exhumation rates in regions where the true geothermal gradient is lower are underestimated, *i.e.*, in the Coastal Cordillera (8 °C/km) and Subandean zone (15 °C/km), whereas rates are overestimated in regions with a higher geothermal gradient such as in parts of the Principal Cordillera close to the magmatic arc (19-69 °C/km).

Furthermore, magmatic bodies in the Andean middle-to-upper crust locally alter the geothermal field. This can lead to a misinterpretation of exhumation rates derived from thermochronological data (*e.g.*, Calk and Naeser, 1973; Murray et al., 2018). For example, a large magma reservoir with a volume of up to 500'000 km^3 (Ward et al., 2014) sits in the upper crust below the Altiplano-Puna plateau (21-24°S, 68.5-66°W) since the late Miocene (de Silva, 1989). However, all thermochronological ages located less than 25 km away from the intrusion boundary are older than Miocene, except for one AHe age, and the latitudinal trend does not show any anomaly in this area (Fig. 9A,B). The data used in this study thus seem to be unaffected by the intrusion. Volcanic and plutonic activity in the Central Andes was common during the Mesozoic in the Coastal Cordillera and during the Cenozoic in the Principal/Western Cordilleras (Fig. 4). Our western thermochronological dataset shows a significant decrease in cooling ages south of 32°S (Fig. 7). This pattern is similar to the distribution of the magmatic intrusion ages (Fig. 4A) that shows mostly Miocene intrusions south of 33°S whereas pre-Miocene ages prevail to the north. Miocene and younger volcanic activity however is relatively uniformly distributed in the Principal Cordillera north of 33°S apart from the amagmatic zone delineating the modern flat slab segment between 28-32°S (Fig. 4B). This suggests that Miocene magmatic bodies were most probably also present in the northern segment of the Andes but are simply not exposed due to lower exhumation rates in this zone. Likewise, pre-Miocene intrusions are preserved in the north whereas higher exhumation rates in the southern Principal Cordillera may have caused their erosion and the exposure of younger magmatic bodies. No data are available in the Coastal Cordillera south of 32°S and we thus relate the absence of Cretaceous and Paleozoic igneous rocks in this area to a sampling bias. Our samples were taken at a minimum distance of 25 km from Holocene volcanoes in order to exclude possible hydrothermal disturbances of the geothermal field by volcanic activity. Few literature samples are located closer to Holocene volcanos, but their ages show no anomalies in the cross-sectional age trends depicted in Figures 7, 8 and 9. We thus conclude that magmatic effects on our thermochronological dataset are negligible.

Another factor that influences the magnitude of the modelled exhumation rates is the $\dot{e}_{prior}$ because it remains part of the solution (Equation 4) (Fox et al., 2014; Herman et al., 2013; Jiao et al., 2017; Willett et al., subm.). If the data resolution capacity is low, the model solution is especially sensitive to the prior model due to the impossibility of recovering a function not sampled by the age data. In such cases, our model parameter will not deviate from the prior value. Furthermore, this can lead to a spurious acceleration or deceleration of the exhumation rates as rates begin to deviate from the prior due to increased data resolution (*e.g.*, Fox et al., 2014; Willett et al., subm.). Fig. 14 shows that the impact of the $\dot{e}_{prior}$ on our model solution is especially important at the beginning when the oldest thermochronological ages become available but when data resolution is still poor. For example, an overestimated $\dot{e}_{prior}$ leads to a decrease in exhumation rates when the model starts to incorporate data that indicate a lower rate than the assumed $\dot{e}_{prior}$, as observed for an $\dot{e}_{prior}$ of 0.5 km/Ma between 14 and 8 Ma at the site of AER-a (Fig. 14C) and between at 80 Ma at the site of AER-b (Fig. 14D). In such cases, a diagnostic feature to recognize the validity of the inversion results is the reduced variance: if the deceleration/acceleration corresponds to an interval with reduced variance close to 1, than the model is poorly resolved over that period and the deceleration/acceleration is likely not a robust feature (*e.g.*, Fig. 14E,F). If the deceleration/acceleration instead corresponds to intervals with good data resolution, then the influence of the $\dot{e}_{prior}$ is negligible.

We prefer an $\dot{e}_{prior}$ value of 0.1 km/Ma over an $\dot{e}_{prior}$ of 0.5 km/Ma, despite the better model fit of the ZHe and ZFT ages with the higher prior value (supplementary Fig. S2). The reason for this is that during the late Cretaceous to the middle Eocene, a high $\dot{e}_{prior}$ predicts high exhumation rates due to the lack of resolution. However, exhumation rates were likely to be slow during this time period as there is evidence that little topography existed. It is important to note that the exhumation rates after the middle Eocene are similar for the different $\dot{e}_{prior}$ values, with the $\dot{e}_{prior}$ = 0.5 km/Ma model showing a decrease in rates during the early Eocene to values similar to the $\dot{e}_{prior}$ = 0.1 km/Ma model as resolution increases (supplementary Fig. S3 and movie InversionC). The misfit is especially large for the pre-Oligocene ZHe and ZFT ages (supplementary Fig. S2 A,A*), which are mainly located within the Western Cordillera and are locally close to or younger than their corresponding AHe or AFT age or surrounding AHe/AFT ages (supplementary Table S5). This could be related to issues with the kinetic parameters of the different systems or due to higher exhumation rates that are not recovered by the model due to damping. Yet, no evidence of higher rates during the Paleogene is observed in the inversion with a higher $\dot{e}_{prior}$ (supplementary Fig. S3 and movie, InversionC). Alternatively, the geothermal gradient could have been higher than assumed during this time interval due to the position of the Paleogene magmatic arc in the Western Cordillera (e.g., Charrier et al., 2007). This could explain the better fit of the ZHe ages in the inversion with a higher geothermal gradient (supplementary Fig. S2 B,B* and movie, InversionB) which predicts less age dispersion between the different systems due to smaller differences in the closure depth. Furthermore, a higher $\dot{e}_{prior}$ would be more appropriate in fast exhuming places like the southern Principal Cordillera, the eastern flank of the Andes, or the Sierra Aconquíja in the more recent time steps. Here, erosion rates might be underestimated which could explain the larger misfit of the Neogene AFT ages of the Sierra Aconquíja (supplementary Fig. S2 A).

Finally, the comparison of exhumation histories derived with and without fault blocks but with the same correlation length scale (Fig. 12A,12G and supplementary movies, InversionsA,G) shows that the two versions are similar and lead to the same pattern of exhumation rates. This implies that our model is robust regarding to the fault blocks and that observed increases are not due to potential correlations across faults as suggested by Schildgen et al. (2018).

Our analysis of the influence of the model parameters and model set up on the inversion results shows that the differences in the solution are minor and that the method used in this study is robust. Whereas all inversions show a similar pattern of exhumation rates (*i.e.*, deceleration/acceleration), the magnitude of the exhumation rate depends on the chosen geothermal gradient G_0 and on the $\dot{e}_{prior}$ especially when data resolution is poor.

7.2. Exhumation history of the Central Andes

The large-scale spatial pattern of thermochronological cooling ages and exhumation rates strikingly mimic the present-day climatic precipitation gradients of the Central Andes (Fig. 5). On the western side, the northern arid to semi-arid climate is replaced by more humid conditions south of ca. 30°S due to the influence of the Westerlies. Most ages north of 32°S are Paleogene and, with one exception (Rodríguez et al., 2018), no ages younger than 10 Ma are observed (Fig. 7). This results in generally low exhumation rates over the modelled time period (Fig. 10). South of 32°S, the ages decrease significantly and Plio-to-Pleistocene modelled exhumation rates are markedly increased relative to the north. On the eastern side, the South American Monsoon leads to high precipitation on the mountain front north of ca. 28°S, whereas the climate is semi-arid south of it (Fig. 5). Although no clear correlation between cooling ages and precipitation pattern is observed along the strike of the Andes on the eastern side (Fig. 8), latitudinal cross-sections show that ages north of 28°S are youngest along the eastern mountain front, whereas south of 32°S they are youngest on the western side (Fig. 9). Yet, the observed cooling patterns could also be explained by tectonic deformation that affected most parts of the Andes between the Eocene and the late Miocene and later focused at the eastern mountain front (Fig. 3). These first-order observations imply a complex interplay between tectonics, climate and erosion that is discussed below for the northern, central, and southern segments of the central-southern Central Andes.

7.2.1. Northern segment (18 - 28°S)

On the western side of the Andes, exhumation started in the Late Cretaceous to Paleocene as constrained by cooling ages mainly located in the Coastal Cordillera and Central Depression. This corroborates the idea that mountain building may have started during this time (e.g., Mpodozis et al., 2005; Arriagada et al., 2006; Henriquez et al., 2019). However, the inversion results do not sufficiently resolve possible changes in exhumation rates on the western side of the drainage divide (Fig. 11). In fact, the data can be fitted with relatively constant exhumation rates that did not exceeded 0.2 km/Ma since 80 Ma (Fig. 10). This is supported by the inversion with an $\dot{e}_{prior}$ value of 0.5 km/Ma that recovers equally low rates in places with better resolution (*e.g.*, Fig. 12, supplementary Fig. S3 and movie, InversionC). Our results do not exclude a pulse of exhumation during the Paleogene that is expected from the deformation record (Sec. 2.1) and suggested by the thermo-kinematic modelling of thermochronometric data in Reiners et al. (2015), but data resolution on the western side of the orogen is too low to discriminate between constant low erosion rates and migrating pulses of exhumation during this time interval. Furthermore, our assumption of monotonic cooling might not be appropriate due to volcanic reburial (Reiners et al., 2015).

In this arid zone of the Central Andes, deformation started in the Late Cretaceous in the Central Depression and Western/Principal Cordillera (Fig. 3A) and was active throughout the Cenozoic, but with low shortening rates (Fig. 2; Victor et al., 2004; Oncken et al., 2006). A major phase of mountain building took place in the Eocene with shortening rates up to 1.2 mm/a (Fig. 2, Fig. 3; Oncken et al., 2006). Our inversion resolves a localised pulse of enhanced exhumation (≤0.2 km/Ma) between 26°S and 28°S from 58 to 38 Ma (Fig. 10A, B), which might be associated with increased shortening rates during that time. Similar pulses of localized enhanced exhumation are also observed along the western Andean piedmont since the Miocene (Fig. 10G). These might be linked to the onset of deep canyon incision and intensified uplift of the western Andean flank since the middle Miocene (*e.g.*, *e.g.*, Farías et al., 2005; García and Hérail, 2005; Hoke et al., 2007; Jordan et al., 2010; García et al., 2011; Cooper et al., 2016). However, exhumation rates in this part of the Central Andes were generally low and are thus consistent with low amounts of horizontal shortening and low mean annual precipitation.

On the eastern side of the Central Andes, a first signal in exhumation is observed in the northern Sierra Pampeanas in the Late Cretaceous that can be related to extensional tectonics of the Salta rift system (e.g., Grier et al., 1999; Marquillas et al., 2005). Only by the middle-to-late Eocene, exhumation starts locally in the Eastern Cordillera and the Altiplano-Puna plateau and subsequently covers larger parts of these regions during the Oligocene. This is in good agreement with the onset of syntectonic sedimentation in these regions (Fig. 3A; *e.g.*, Coutand et al., 2001; Elger et al., 2005; McQuarrie et al., 2005; Montero-López et al., 2016) and with the early Oligocene onset of major crustal thickening in the northern segment (*e.g.*, Mamani et al., 2010a). Shortening rates in the northern part of the Eastern Cordillera culminated in the Oligocene to the early Miocene (Müller et al., 2002; Elger et al., 2005), but exhumation rates remained relatively constant during this time period (Fig. 10D, E). This indicates that episodes of horizontal shortening are not necessarily followed by pulses in exhumation. During the Miocene, exhumation affected large parts of the Puna, Eastern Cordillera, north-western Sierra Pampeanas and the Interandean zone (Fig. 10F, G). This exhumation pattern agrees well with major tectonic deformation that affected the whole Andes except for the Subandean zone from the Oligocene until ca. 10 Ma. It also correlates with intense shortening in the Puna (Coutand et al., 2001) and with the onset of basement block uplift in the Eastern Cordillera that led to the compartmentalization of the foreland (*e.g.*, Coutand et al., 2006). In the late Miocene (~12 Ma), exhumation propagated into the Subandean zone (Fig. 10G) and thus reflects the eastward propagation of deformation into this area (Fig. 3A). Similarly, exhumation in the southern Eastern Cordillera also spreads eastwards during this time, contemporaneously with the east-directed, yet unsystematic propagation of uplifting basement blocks (*e.g.*, Coutand et al., 2006; Hain et al., 2011) (supplementary movie, InversionA). However, exhumation rates in the southern Eastern Cordillera as resolved by our inversion appear relatively constant through time (Fig. 10) in spite of the successive aridification of the hinterland that is associated with growing orographic barriers (Coutand et al., 2006). This can be explained by low data resolution in the western part of the southern Eastern Cordillera where only data from single thermochronometric systems (either AFT or AHe) are available, which are older than 10 Ma, or ZHe older than 80 Ma, which are not included in the modelling (Deeken et al., 2006; Carrapa et al., 2011; Pearson et al., 2013; Carrapa et al., 2014; Reiners et al., 2015).

The initiation of the South American Monsoon in the late Miocene (10-7 Ma) led to important hydrological changes at the eastern mountain front (*e.g.*, Strecker et al., 2007; Uba et al., 2007; Mulch et al., 2010). Increased exhumation rates in the eastern Interandean zone and the Subandean belt since the latest Miocene (~6 Ma) could thus be an expression of enhanced precipitation and higher climate variability associated with the onset of the monsoonal climate (e.g., Mulch et al., 2010; Rohrmann et al., 2016) and the establishment of high-amplitude climatic oscillations in the Plio-Pleistocene (Shackleton et al., 1984) (Fig. 10H-K, supplementary movie, InversionA). Conversely, they can also be explained by augmented shortening rates (Echavarria et al., 2003) or a combination of both. Higher moisture availability might also account for higher exhumation rates observed locally in the Eastern Cordillera during the late Miocene. Finally, the Sierra Aconquíja in the northern Sierra Pampeanas shows a strong Plio-Pleistocene acceleration in exhumation, where rates increase from <0.1 km/Ma before 6 Ma to ca. 1.5 km/Ma in the Pleistocene (Fig. 10H-K). The Sierra Aconquíja is a major orographic barrier for westward moisture-bearing winds from the foreland and receives more than 800 mm/a rainfall on its eastern flank (Sobel and Strecker, 2003). Major tectonically-driven surface uplift and relief development started after 6 Ma along high-angle reverse faults, intensified during the Pliocene and was most pronounced after 3 Ma (Strecker et al., 1989; Bossi et al., 2001; Zapata et al., 2019). Ensuing aridification of the adjacent intermontane basin to the west has occurred between 3 and 2.5 Ma as a result of the establishment of an efficient orographic barrier at that time (Kleinert and Strecker, 2001). Taken together, the Pleistocene increase in exhumation rate in this area can be explained by the interplay of active tectonic uplift and efficient erosion related to very high precipitation and localized Pleistocene glaciation (*e.g.*, Sobel and Strecker, 2003; Löbens et al., 2013). A similar Pleistocene increase in the exhumation rate also occurred in the Fiambalá Basin (western northern Sierra Pampeanas) but is only based on one young AHe age of 2.3 ± 0.05 Ma (*e.g.*, Fig. 8, Fig. 9B) that has been attributed to Plio-Pleistocene tectonic activity in this area (Carrapa et al., 2008; Safipour et al., 2015).

In the northern segment of the Central Andes, the influence of both climate and tectonic processes can be observed. On the western side, exhumation rates are slow and correspond to very low shortening rates and high aridity. Although significant topography at the western flank of the Andes might have existed since the middle Miocene or earlier (Hoke and Garzione, 2008; Jordan et al., 2010; Evenstar et al., 2015; Scott et al., 2018), little exhumation has occurred during the Cenozoic in this part of the Andes. Reburial linked to volcanic covering and internal drainage of the Altiplano-Puna plateau, a consequence of dry climatic conditions, contributed to low exhumation rates (*e.g.*, Reiners et al., 2015). This suggests that erosion in the west is primarily inhibited due to the absence of precipitation and possibly would have been higher in a different climatic setting. The onset of exhumation on the eastern side of the Andes seems to be synchronous with the onset of tectonic activity (Fig. 3A). The observed exhumation pattern also generally agrees well with phases of major tectonic deformation, but increased horizontal shortening does not necessarily result in pulses of enhanced exhumation. However, as deformation propagates into areas that were previously not subjected to shortening, so does exhumation. This is clearly observed in the eastward migration of exhumation into the Subandean zone and in the southern Eastern Cordillera during the late Miocene that reflects the eastward propagation of deformation in these areas.

Exhumation rates in the east are higher than in the west. This can be explained by higher amounts of horizontal shortening and/or higher moisture availability in a semi-arid to humid environment. Increased exhumation rates in the eastern Interandean and the Subandean zone since the latest Miocene (ca. 6 Ma) can equally be explained by either increased shortening rates (Echavarria et al., 2003) or higher precipitation associated with the onset of the South American Monsoon (*e.g.*, Strecker et al., 2007; Uba et al., 2007; Mulch et al., 2010) and the establishment of high-amplitude climatic oscillations in the Plio-Pleistocene (Shackleton et al., 1984) associated with Late Cenozoic global cooling (Zachos et al., 2001). Yet, Pleistocene exhumation rates in the northern Sierra Pampeanas are significantly higher than in the Subandean range, although both were tectonically active and received high amounts of precipitation during the last 2 Myr. They differ, however, in their tectonic style. Whereas deformation in the Subandean belt is thin-skinned (*e.g.*, Echavarria et al., 2003;

Anderson et al., 2017), shortening in the northern Sierra Pampeanas is accommodated along steep (50-60° dip; Strecker et al., 1989), basement-involving reverse faults that result in important surface uplift (*e.g.*, Sobel and Strecker, 2003), steep topography and high exhumation rates. This suggest that the tectonic style that accommodates deformation is a major factor in setting the exhumation rate under similar precipitation conditions. Our results further show that the onset of exhumation agrees relatively well with the onset of tectonic activity, whereas the magnitude of exhumation rates seems to be strongly modulated by climatic conditions and the tectonic style which accommodates deformation. Therefore, in the northern segment of the Central Andes, we cannot disentangle the respective roles of deformation and climate on exhumation.

7.2.2. Central segment (28 - 32°S)

The central part of the orogen between 28° and 32°S is currently located above the Pampean flat slab segment which initiated in the latest early Miocene (*e.g.*, Kay and Mpodozis, 2002). On the western side of the range, where thermochronological data are abundant, little information about the timing and magnitude of tectonic activity exists. Contractional deformation initiated in the Late Cretaceous to the Paleocene in the Principal and Frontal Cordilleras. Similar to the northern segment, exhumation during the Paleogene is recorded with relatively low rates (< 0.2 km/Ma) although data resolution is too low to infer changes in exhumation rates. This supports previous interpretations of structural and sedimentary observations (Martínez et al., 2016; Rossel et al., 2016; Fosdick et al., 2017; Martínez et al., 2018) and thermochronological data (Cembrano et al., 2003; Lossada et al., 2017; Rodríguez et al., 2018) that indicate an early, pre-Oligocene onset of mountain building in this part of the Andes. In the Oligocene, contractional deformation was interrupted by extension and only resumed in the early Miocene by basin inversion and deformation in the Frontal Cordillera

(Fig. 3B; Winocur et al., 2015; Martínez et al., 2016; Rossel et al., 2016). At a regional scale, exhumation rates in the Frontal Cordillera are moderately higher (0.25 km/Ma) since the late Miocene compared to the northern segment (Fig. 10G). This correlates with the onset of crustal thickening and the peak of slab shallowing (*e.g.*, Kay and Mpodozis, 2002; Rodríguez et al., 2018) that could have led to isostatic uplift (*e.g.*, Dávila and Lithgow-Bertelloni, 2015; Flament et al., 2015) and, in turn, enhanced exhumation rates. Higher exhumation rates could also be explained by the influence of the Westerlies, which bring higher precipitation up to 30°S in austral winter (Garreaud et al., 2009). East of the drainage divide, thermochronological data are very sparse. The main recovered signal is a relatively high Pleistocene exhumation rate (ca. 0.75 km/Ma) in the Sierra Pampeanas which can be attributed to active deformation along reactivated normal faults in the Sierra de Valle Fértil (Ortiz et al., 2015).

7.2.3. Southern segment (32 - 36°S)

Pre-Neogene thermochronological ages are sparse and limited to the Coastal Cordillera, which shows low exhumation rates since the Oligocene (Fig. 10), or close to the mountain front in the Principal Cordillera. Therefore, our reconstruction of the exhumation rate is restricted to the middle Miocene and onwards. Compressional deformation in the southern segment has occurred in the early Miocene after a period of regional extension (Fig. 3C) (*e.g.*, Jordan et al., 2001b; Horton et al., 2018b). A first signal in exhumation rate is recorded after 16 Ma in most parts of the Principal and Frontal Cordilleras (supplementary movie, InversionA). This is later than the suggested onset of tectonic activity in the West-Andean fault-and-thrust belt at ca. 25 Ma (Riesner et al., 2017) and crustal thickening (Kay et al., 2005), but around the same time of the initiation of the Aconcagua fold-and-thrust belt at 18-15 Ma (Giambiagi et al., 2015a). Exhumation rates on the eastern side of the drainage divide continuously accelerated since the late Miocene from 0.15 km/Ma to ca. 0.4 km/Ma in the Pleistocene (Fig. 10) despite decreasing (Giambiagi et al., 2015a) or constant (Riesner et al., 2017) shortening rates (Fig. 2). This might be explained by higher erosional efficiency related to increasing topography associated with Andean mountain building (e.g., Hoke et al., 2014) and by the onset of more humid conditions in the middle Miocene (Jordan et al., 2001a; Ruskin and Jordan, 2007; Ciccioli et al., 2014; Buelow et al., 2018) and the South American Monsoon system in the late Miocene (Strecker et al., 2007; Mulch et al., 2010; Rohrmann et al., 2016). The Principal Cordillera on the western side of the Andes shows low rates (0.1-0.25 km/Ma) during the late Miocene to the late Pliocene that drastically increase to values exceeding 2 km/Ma in the Pleistocene (Fig. 10H-K). These high erosion rates are observed 2 Ma after the period of high surface uplift (10.5-4.6 Ma) (Farías et al., 2008), and although the Principal Cordillera was and is tectonically active, no evidence for intensified Pleistocene rates of horizontal shortening exists (Riesner et al., 2017). Therefore, we cannot explain this change in erosion nor the magnitude of Pleistocene erosion rates by tectonically-driven rock uplift only. Interestingly, this region experienced important glaciation (*e.g.*, Clapperton, 1994) and intensified precipitation (Lamy et al., 1999; Valero-Garcés et al., 2005) during the Pleistocene, processes that are commonly associated to a northward shift of the Westerlies during colder conditions (*e.g.*, Lamy et al., 1999; Zech et al., 2008). We therefore attribute the high Pleistocene erosion rates on the western side of the Andes to glacial erosion and intensified precipitation, reinforced by isostatic rock-uplift and active tectonics. Glacial overprint in this region is also evidenced by glacial relief observed from morphometric analyses (Rehak et al., 2010). Consequently, we conclude that increased erosion caused by the onset of glaciations produced a perturbation to the prevailing conditions in this part of the Central Andes that could have resulted in increased rock uplift and, in turn, further enhanced erosion in a feedback mechanism (*e.g.*, Molnar and England, 1990; Whipple and Meade, 2006).

7.2.4. Integrated view on the exhumation rate pattern from north to south

As shown by the critical wedge theory (*e.g.*, Dahlen and Suppe, 1988; Willett, 1999) and implied by previous case studies of the Central Andes (Masek et al., 1994; Horton, 1999; Montgomery et al., 2001), climatic conditions may control the shape of the mountain belt by influencing the erosion rate. Our study shows that the wide mountain belt in the northern segment indeed correlates with low erosion rates that prevail over most parts of the orogen, apart from focused erosion on its eastern orogenic front. Yet, reconstructed Miocene erosion rates in the southern segment, where the Andes are narrow, are comparably low as in the northern segment and only accelerated in the Plio-Pleistocene. It seems thus likely that processes such as mantle dynamics, tectonic activity and crustal thickening set the topographic expression of the Central Andes, which is then modulated by climatic conditions. In particular, the northern Central Andes experienced more horizontal shortening and crustal thickening than the southern segment, and both processes initiated earlier in the northern segment. This may have resulted in orographic growth before (*e.g.*, Canavan et al., 2014; Scott et al., 2018) or during (*e.g.*, Fiorella et al., 2015) the Oligocene. On the contrary, the southern segment experienced a period of Oligocene extension and horizontal shortening resumed only in the early Miocene, with values significantly lower than in the north (Fig. 2, Fig. 3). Given these different tectonic settings, it remains open if the southern segment of the Central Andes would have reached similar width and height as the northern segment, although significant growth seems to be unlikely under the such high Plio-Pleistocene erosion rates. Similarly, the building up of the Altiplano-Puna plateau might not have been possible under higher erosion rates.

Our analysis of the exhumation rate in the Central Andes indicates that the onset of tectonic activity and major crustal thickening mainly correlates with the onset of exhumation as constrained by the oldest cooling ages in a given region. However, these ages could be younger than the true onset of exhumation and therefore they represent minimum ages for initial cooling. Our results also highlight the influence of climatic conditions on the magnitude of upper crustal exhumation. Exhumation rates in the Central Andes vary most commonly between 0.05 km/Ma and 0.25 km/Ma with important regional exceptions. The highest rates are observed during the Plio-Pleistocene in the Subandean range, the Sierra Aconquíja in the northern Sierra Pampeanas and in the Principal Cordillera south of 33°S. These regions are all characterized by active tectonics and high moisture availability but show important differences that highlight several aspects of the relationships between tectonics, climate and exhumation. First, inherited structures and the presence of sediments and decollement layers in the foreland control the way how deformation is accommodated (*e.g.*, Allmendinger et al., 1983) and directly influence the exhumation rate by determining the steepness of faults and thus the amount of vertical displacement. Second, we observe similar Mio-to-Pliocene erosion rates in the western part of the southern segment (Principal Cordillera) and in the eastern part of the northern segment (Eastern Cordillera, Inter- and Subandean zones), although shortening rates are much higher in the north than in the south (Fig. 2). This suggests that the magnitude of erosion does not necessarily correlate with the amount of horizontal shortening and that moisture availability and the structural style of deformation have an important role in setting the exhumation rate. Finally, glacial erosion in the southern Principal Cordillera increases the exhumation rate previously set by deformation and fluvial processes by ca. one order of magnitude.

8. Conclusion

In this study, we provide 238 new thermochronological ages from 146 samples that we complement with 824 ages from literature to constrain the exhumation rate history of the Central Andes. To gain insights about feedback mechanisms between climate, tectonics and erosion, we compare the exhumation rate history to the past and present climatic setting and to the deformation record of the Central Andes.

In the arid region west of the Andes (18 - 32°S), exhumation rates are generally low (<0.2 km/Ma) and correlate well with low shortening rates and high aridity. On the eastern side of the Andes in the northern segment, the subsequent onset of exhumation in the Eastern Cordillera, Altiplano-Puna plateau and Inter- and Subandean zones reflects the onset and eastward propagation of deformation observed in this region. Accelerated exhumation since the latest Miocene in the eastern Interandean and the Subandean zone can be either related to increased horizontal shortening rates, the onset of the South American Monsoon, or the coupling between the two.

Highest exhumation rates are observed during the Pleistocene in the Sierra Aconquíja in the northern Sierra Pampeanas and in the Principal Cordillera south of 33°S and west of the Andes. These regions are characterized by active tectonics accommodated along steep, reactivated normal faults and affected by either particularly high rainfall (Sierra Aconquíja) or intense glacial erosion (southern Principal Cordillera). The observed exhumation rates in these regions are higher than the ones observed in the Subandean range, which is characterized by high shortening rates accommodated by thin-skinned deformation. This indicates that the style of deformation, which is largely set by inherited structures and the presence of sediments in the foreland, has a significant impact on the magnitude of exhumation rates, as does glacial erosion and increased precipitation in an active tectonic setting.

Acknowledgements

We thank Alexej Ulianov for his support with the U–Pb analysis and Djordje Grujic and team at Dalhousie University for efficient analyses of ZHe data. B. Horton and an anonymous reviewer significantly helped improving the manuscript. First Quantum Minerals Ltd funded two sampling campaigns and the data analyzed at the University of Arizona.

References

Aguilar, G., Riquelme, R., Martinod, J., Darrozes, J., Maire, E., 2011. Variability in erosion rates related to the state of landscape transience in the semi-arid Chilean Andes: Earth Surface Processes and Landforms, 36 (13), 1736-1748.

Allmendinger, R.W., Gubbels, T., 1996. Pure and simple shear plateau uplift, Altiplano-Puna, Argentina and Bolivia. Tectonophysics, 259 (1-3), 1-13.

Allmendinger, R.W., Judge, P.A., 2014. The Argentine Precordillera: A foreland thrust belt proximal to the subducted plate. Geosphere, 10 (6), 1203-1218.

Allmendinger, R.W, Ramos, V.A., Jordan, T.E., Palma, M., Isacks, B.L., 1983. Paleogeography and Andean structural geometry, northwest Argentina. Tectonics, 2, 1–16.

Allmendinger, R. W., Figueroa, D., Snyder, D., Beer, J., Mpodozis, C., Isacks, B. L., 1990. Foreland shortening and crustal balancing in the Andes at 30°S latitude. Tectonics, 9 (4), 789-809.

Allmendinger, W., Jordan, E., Kay, M., Isacks, B.L., 1997. The evolution of the Altiplano-Puna plateau of the Central Andes. Annu. Rev. Earth Planet. Sci., 25, 139–174.

Amilibia, A., Sàbat, F., McClay, K.R., Muñoz, J.A., Roca, E., Chong, G., 2008. The role of inherited tectono-sedimentary architecture in the development of the central Andean mountain belt: Insights from the Cordillera de Domeyko. J. Struct. Geol., 30 (12), 1520-1539.

Ammann, C., Jenny, B., Kammer, K., Messerli, B., 2001. Late Quaternary glacier response to humidity changes in the arid Andes of Chile (18–29°S). Palaeogeogr., Palaeoclimatol., Palaeoecol., 172 (3-4), 313-326.

Anderson, R.B., Long, S.P., Horton, B.K., Calle, A.Z., Ramirez, V., 2017. Shortening and structural architecture of the Andean fold-thrust belt of southern Bolivia (21°S): Implications for kinematic development and crustal thickening of the central Andes. Geosphere, 13 (2), 538–558. doi:10.1130/GES01433.1.

Armijo, R., Rauld, R., Thiele, R., Vargas, G., Campos, J., Lacassin, R., Kausel, E., 2010. The West Andean thrust, the San Ramon fault, and the seismic hazard for Santiago, Chile. Tectonics, 29 (TC2007). doi:10.1029/2008TC002427.

Armijo, R., Lacassin, R., Coudurier-Curveur, A., Carrizo, D., 2015. Coupled tectonic evolution of Andean orogeny and global climate. Earth-Sci. Rev., 143, 1-35. http://dx.doi.org/10.1016/j.earscirev.2015.01.005

Arriagada, C., Cobbold, P.R., Roperch, P., 2006. Salar de Atacama basin: A record of compressional tectonics in the central Andes since the mid-Cretaceous. Tectonics, 25 (TC1008). doi:10.1029/2004TC001770.

Assumpção, M., Feng, M., Tassara, A., Julià, J., 2013. Models of crustal thickness for South America from seismic refraction, receiver functions and surface wave tomography. Tectonophysics, 609, 82-96.

Aster, R.C., Borchers, B., Thurber, C.H., 2011. Parameter estimation and inverse problems, Academic Press, Elsevier, Vol. 90.

Avdievitch, N.N., Ehlers, T.A., Glotzbach, C., 2018. Slow Long-Term Exhumation of the West Central Andean Plate Boundary, Chile. Tectonics, 37 (7), 2243–2267. doi:10.1029/2017TC004944

Baby, P., Hérail, G., Salinas, R., Sempere, T., 1992. Geometry and kinematic evolution of passive roof duplexes deduced from cross section balancing: example from the foreland thrust system of the southern Bolivian Subandean Zone. Tectonics, 11, 523–536.

Baker, P.A., Fritz, S.C., 2015. Nature and causes of Quaternary climate variation of tropical South America. Quat. Sci. Rev., 124, 31-47.

Barazangi, M., Isacks, B.L., 1976. Spatial distribution of earthquakes and subduction of the Nazca plate beneath South America. geology, 4(11), 686-692.

Barnes, J.B., Ehlers, T.A., McQuarrie, N., O'Sullivan, P.B., Pelletier, J.D., 2006. Eocene to recent variations in erosion across the central Andean fold-thrust belt, northern Bolivia: implications for plateau evolution. Earth Planet. Sci. Lett. 248, 118–133.

Barnes, J.B., Ehlers, T.A., 2009. End member models for Andean Plateau uplift. Earth-Sci. Rev., 97, 105-132. doi:10.1016/j.earscirev.2009.08.003.

Barnes, J.B., Ehlers, T.A., Insel, N., McQuarrie, N., Poulsen, C.J., 2012. Linking orography, climate, and exhumation across the central Andes. Geology, 40 (12), 1135-1138. doi:10.1130/G33229.1

Barrientos, S., Vera, E., Alvarado, P., Monfret, T., 2004. Crustal seismicity in central Chile. J. S. Am. Earth Sci., 16, 759-768. doi:10.1016/j.jsames.2003.12.001

Bascuñán, S., Arriagada, C., Le Roux, J., Deckart, K., 2016. Unraveling the Peruvian Phase of the Central Andes: stratigraphy, sedimentology and geochronology of the Salar de Atacama Basin (22°30–23°S), northern Chile. Basin Research, 28(3), 365-392.

Bascuñán, S., Maksymowicz, A., Martínez, F., Becerra, J., Arriagada, C., Deckart, K., 2019. Geometry and late Mesozoic-Cenozoic evolution of the Salar de Atacama Basin (22° 30′-24° 30′ S) in the northern Central Andes: New constraints from geophysical, geochronological and field data. Tectonophysics, 759, 58-78.

Batt, G.E., Braun, J., 1997. On the thermomechanical evolution of compressional orogens. Geophys. Jour. Internat., 128(2), 364-382.

Beaumont, C., Quinlan, G., Hamilton, J., 1988. Orogeny and stratigraphy: Numerical models of the Paleozoic in the eastern interior of North America. Tectonics, 7(3), 389-416.

Beaumont, C., Fullsack, P., Hamilton, J., 1992. Erosional control of active compressional orogens, in: McClay, K.R. (Eds.), Thrust tectonics, Springer, Dordrecht, pp. 1-18. doi: 10.1007/978-94-011-3066-0

Beck, S.L., Zandt, G., Myers, S.C., Wallace, T.C., Silver, P.G., Drake, L., 1996. Crustal-thickness variations in the central Andes. Geology, 24 (5), 407-410.

Becker, J. J., Sandwell, D.T., Smith, W.H.F. , Braud, J., Binder, B., Depner, J., Fabre, D., Factor, J., Ingalls, S., Kim, S-H., Ladner, R., Marks, K., Nelson, S., Pharaoh, A., Trimmer, R., Von Rosenberg, J., Wallace, G., Weatherall., P., 2009. Global Bathymetry and Elevation Data at 30 Arc Seconds Resolution: SRTM30_PLUS. Mar. Geod., 32 (4), 355-371. doi: 10.1080/01490410903297766

Bossi, G.E., Georgieff, S.M., Gavriloff, I.J., Ibañez, L.M., Muruaga, C.M., 2001. Cenozoic evolution of the intramontane Santa María basin, Pampean Ranges, northwestern Argentina. J. S. Am. Earth Sci., 14 (7), 725-734.

Brandon, M., 2002. Decomposition of mixed grain age distributions using BinomFit. On Track, 24, 13-18.

Braun, J.B., 2002a. Quantifying the effect of recent relief changes on age-elevation relationships. Earth Planet. Sci. Lett. 200, 331-343.

Braun, J.B., 2002b. Estimating exhumation rate and relief evolution by spectral analysis of age–elevation datasets. Terra Nova, 14 (3), 210-214.

Braun, J.B., 2010. The many surface expressions of mantle dynamics. Nat. Geosci., 3, 825-833.

Buelow, E. K., Suriano, J., Mahoney, J. B., Kimbrough, D. L., Mescua, J. F., Giambiagi, L. B., & Hoke, G. D. (2018). Sedimentologic and stratigraphic evolution of the Cacheuta basin: Constraints on the development of the Miocene retroarc foreland basin, south-central Andes. Lithosphere, 10(3), 366-391.

Burns, W.M., Jordan, T.E., Copeland, P., Kelley, S.A., 2006. The case for extensional tectonics in the Oligocene-Miocene southern Andes as recorded in the Cura-Mallín Basin (36°-38°S). Spec. Pub. Geol. Soc. Am., 407, 163–184.

Cahill, T., Isacks, B.L., 1992. Seismicity and shape of the subducted Nazca Plate. J. Geophys. Res., 97 (B12), 17503–17529, doi: 10.1029/92JB00493.

Calk, L.C., Naeser, C.W., 1973. The Thermal Effect of a Basalt Intrusion on Fission Tracks in Quartz Monzonite. J. Geol., 81 (2), 189-198.

Calle, A.Z., Horton, B.K., Limachi, R., Stockli, D.F., Uzeda-Orellana, G.V., Anderson, R.B., Long, S.P., 2018. Cenozoic provenance and depositional record of the Subandean foreland basin during growth and advance of the central Andean fold-thrust belt, southern Bolivia, in: Zamora, G., McClay, K., Ramos, V. (Eds.), Petroleum Basins and Hydrocarbon Potential of the Andes of Peru and Bolivia. Am. Assoc. Petr. Geol. Mem., 117, pp. 483-530. doi: 10.1306/13622132m1173777.

Campetella, C. M., Vera, C. S., 2002. The influence of the Andes mountains on the South American low-level flow. Geophy. Res. Lett., 29(17), 7-1.

Canavan, R.R., Carrapa, B., Clementz, M.T., Quade, J., DeCelles, P.G., Schoenbohm, L.M., 2014. Early Cenozoic uplift of the Puna Plateau, Central Andes, based on stable isotope paleoaltimetry of hydrated volcanic glass. Geology, 42 (5), 447-450.

Carrapa, B., DeCelles, P.G., 2008. Eocene exhumation and basin development in the Puna of northwestern Argentina. Tectonics, 27 (1). doi:10.1029/2007TC002127

Carrapa, B., DeCelles, P.G., 2015, Regional exhumation and kinematic history of the central Andes in response to cyclical orogenic processes. Geol. Soc. Am. Mem., 212, 201-213.

Carrapa, B., Adelmann, D., Hilley, G.E., Mortimer, E., Sobel, E.R., Strecker, M.R., 2005. Oligocene range uplift and development of plateau morphology in the southern central Andes. Tectonics, 24, TC4011, doi:10.1029/2004TC001762

Carrapa, B., Hauer, J., Schoenbohm, L., Strecker, M.R., Schmitt, A.K., Villanueva, A., Sosa Gomez, J., 2008. Dynamics of deformation and sedimentation in the northern Sierras Pampeanas: An integrated study of the Neogene Fiambalá basin, NW Argentina. Geol. Soc. Am. Bull., 120 (11-12), 1518-1543. doi: 10.1130/B26111.1

Carrapa, B., Trimble, J.D., Stockli, D.F., 2011. Patterns and timing of exhumation and deformation in the Eastern Cordillera of NW Argentina revealed by (U-Th)/He thermochronology. Tectonics, 30, TC3003. doi: 10.1029/2010TC002707

Carrapa, B., Reyes-Bywater, S., Safipour, R., Sobel, E.R., Schoenbohm, L.M., DeCelles, P.G., Reiners, P.W., Stockli, D., 2014. The effect of inherited paleotopography on exhumation of the Central Andes of NW Argentina. Geol. Soc. Am. Bull., 126 (1-2), 66-77.

Carrera, N., Muñoz, J.A., 2008. Thrusting evolution in the southern Cordillera Oriental (northern Argentine Andes): Constraints from growth strata. Tectonophysics, 459, 107-122. doi:10.1016/j.tecto.2007.11.068

Carretier, S., Regard, V., Vassallo, R., Aguilar, G., Martinod, J., Riquelme, R., Pepin, E., Charrier, R., Hérail, G., Farías, M., Guyot, J.L., 2013. Slope and climate variability control of erosion in the Andes of central Chile. Geology, 41 (2), 195-198.

Carretier, S., Tolorza, V., Regard, V., Aguilar, G., Bermúdez, M.A., Martinod, J., Guyot, J.L., Hérail, G., Riquelme, R., 2018. Review of erosion dynamics along the major NS climatic gradient in Chile and perspectives. Geomorphology, 300, 45-68.

Carvalho, L.M., Jones, C., Liebmann, B., 2004. The South Atlantic convergence zone: Intensity, form, persistence, and relationships with intraseasonal to interannual activity and extreme rainfall. J. Climate, 17 (1), 88-108.

Champagnac, J. D., Molnar, P., Sue, C., Herman, F., 2012. Tectonics, climate, and mountain topography. J. Geophys. Res. Solid Earth, 117, B02403. doi:10.1029/2011JB008348

Charrier, R., Baeza, O., Elgueta, S., Flynn, J.J., Gans, P., Kay, S. M., Muñoz, N., Wyss, A.R., Zurita, E., 2002. Evidence for Cenozoic extensional basin development and tectonic inversion south of the flat-slab segment, southern central Andes, Chile (33°–36°S.L.). J. S. Am. Earth Sci., 15, 117–139.

Charrier, R., Pinto, L., Rodríguez, M.P., 2007. Tectonostratigraphic evolution of the Andean Orogen in Chile, in: Moreno, T., Gibbons, W. (Eds.), The Geology of Chile. Geol. Soc. London, pp. 21–114.

Charrier, R., Hérail, G., Pinto, L., García, M., Riquelme, R., Farías, M., Muñoz, N., 2013. Cenozoic tectonic evolution in the Central Andes in northern Chile and west central Bolivia: implications for paleogeographic, magmatic and mountain building evolution. Int. J. Earth Sci., 102 (1), 235-264.

Charrier, R., Ramos, V.A., Tapia, F., Sagripanti, L., 2015. Tectono-stratigraphic evolution of the Andean Orogen between 31° and 37°S (Chile and Western Argentina). J. Geol. Soc. Spec. Publ. 399, 13–61. http://dx.doi.org/10.1144/SP399.20.

Charrier, R., Iturrizaga, L., Carretier, S., Regard, V., 2019. Geomorphologic and Glacial Evolution of the Cachapoal and southern Maipo catchments in the Andean Principal Cordillera, Central Chile (34°-35º S). Andean Geology, 46(2), 240-278.

Chulick, G.S., Detweiler, S., Mooney, W.D., 2013. Seismic structure of the crust and uppermost mantle of South America and surrounding oceanic basins. J. S. Am. Earth Sci., 42, 260-276.

Čermák, V., Rybach, L., 1982. Thermal properties: Thermal conductivity and specific heat of minerals and rocks, in: Angeneister, A. (Ed), Landolt-Börnstein Zahlenwerte und Funktionen aus Naturwissenschaften und Technik, Neue Serie, Physikalische Eigenschaften der Gesteine. Springer Verlag, Berlin, V/1a, pp. 305 – 343.

Ciccioli, P. L., Limarino, C. O., Friedman, R., Marenssi, S. A., 2014. New high precision U-Pb ages for the Vinchina Formation: implications for the stratigraphy of the Bermejo Andean foreland basin (La Rioja province, western Argentina). Journal of South American Earth Sciences, 56, 200-213.

Clapperton, C.M., 1983. The glaciation of the Andes. Quat. Sci. Rev., 2 (2-3), 83-155.

Clapperton, C. M., 1994. The quaternary glaciation of Chile: a review. Rev. Chil. Hist. Nat., 67 (4), 369-383.

Clark, P.U., Dyke, A.S., Shakun, J.D., Carlson, A.E., Clark, J., Wohlfarth, B., Mitrovica, J.X., Hostetler, S.W., McCabe, A.M., 2009. The last glacial maximum. Science, 325 (5941), 710-714.

Cooper, F.J., Adams, B.A., Blundy, J.D., Farley, K.A., McKeon, R.E., Ruggiero, A., 2016. Aridity-induced Miocene canyon incision in the Central Andes. Geology, 44 (8), 675-678.

Cornejo, P.C., Mahood, G.A., 1997. Seeing past the effects of re-equilibration to reconstruct magmatic gradients in plutons: La Gloria Pluton, central Chilean Andes. Contr. Mineral. Petrol., 127, 159-175.

Coutand, I., Cobbold, P.R., de Urreiztieta, M., Gautier, P., Chauvin, A., Gapais, D., Rossello, E.A., López-Gamundí, O., 2001. Style and history of Andean deformation, Puna plateau, northwestern Argentina. Tectonics, 20, 210 – 234.

Coutand, I., Carrapa B., Deeken., A., Schmitt, A.K., Sobel., W.R., Strecker, M.R., 2006. Propagation of orographic barriers along an active range front: insights from sandstone petrography and detrital apatite fission-track thermochronology in the intramontane Angastaco basin, NW Argentina. Basin Res., 18, 1-26, doi:10.1111/j.1365-2117.2006.00283.x

Dahlen, F., Suppe, J., 1988. Mechanics, growth, and erosion of mountain belts. Geol. Soc. Am. Spec. Publ., 218, 161-178.

Danielson, J.J., Gesch, D.B., 2011. Global multi-resolution terrain elevation data 2010 (GMTED2010) (No. 2011-1073). US Geological Survey.

D'Arcy, M., Schildgen, T.F., Strecker, M.R., Wittmann, H., Duesing, W., Mey, J., Tofelde, S., Weissmann, P., Alonso, R.N., 2019. Timing of past glaciation at the Sierra de Aconquíja, northwestern Argentina, and throughout the Central Andes. Quat. Sci. Rev, 204, 37-57.

Dávila, F.M., Lithgow-Bertelloni, C., 2015. Dynamic uplift during slab flattening. Earth Planet. Sci. Lett., 425, 34-43.

Davis, D., Suppe, J., Dahlen, F. A., 1983. Mechanics of fold-and-thrust belts and accretionary wedges. Jour. Geophys. Res.: Solid Earth, 88(B2), 1153-1172.

DeCelles, P.G., Horton, B.K., 2003. Early to middle Tertiary foreland basin development and the history of Andean crustal shortening in Bolivia. Geol. Soc. Am. Bull., 115, 58–77.

DeCelles, P. G., Carrapa, B., Horton, B.K., Gehrels, G.E., 2011. Cenozoic foreland basin system in the central Andes of northwestern Argentina: Implications for Andean geodynamics and modes of deformation. Tectonics, 30 (TC6013). doi:10.1029/2011TC002948

Deckart, K., Clark, A.H., Celso, A.A., Ricardo, V.R., Bertens, A.N., Mortensen, J.K., Fanning, M., 2005. Magmatic and hydrothermal chronology of the giant Río Blanco porphyry copper deposit, central Chile: Implications of an integrated U-Pb and ^{40}Ar/^{39}Ar database. Econ. Geol., 100 (5), 905-934.

Deeken, A., Sobel, E.R., Coutand, I., Haschke, M., Riller, U., Strecker, M.R., 2006. Development of the southern Eastern Cordillera, NW Argentina, constrained by apatite fission track thermochronology: From early Cretaceous extension to middle Miocene shortening. Tectonics, 25 (TC6003). doi:10.1029/2005TC001894.

del Papa, C., Hongn, F., Powell, J., Payrola, P., Do Campo, M., Strecker, M.R., Petrinovic, I., Schmitt, A.K., Pereyra, R., 2013. Middle Eocene-Oligocene broken-foreland evolution in the Andean Calchaqui Valley, NW Argentina: insights from stratigraphic, structural and provenance studies. Basin Res., 25, 574-593. doi: 10.1111/bre.12018 del Rey, A., Deckart, K., Arriagada, C., Martínez, F., 2016. Resolving the paradigm of the late Paleozoic–Triassic Chilean magmatism: Isotopic approach. Gondwana Res., 37, 172-181. doi: 10.1016/j.gr.2016.06.008

De Martonne, E., 1925. Traité de Géographie Physique. Librairie Armand Colin, Paris.

de Silva, S.L., 1989. Altiplano-Puna volcanic complex of the central Andes. Geology, 17, 1102–1106.

de Silva, S.L., Kay, S.M., 2018. Turning up the Heat: High-flux Magmatism in the Central Andes. Elements, 14, 245-250.

Dewey, J.F., Bird, J.M., 1970. Mountain belts and the new global tectonics. J. Geophys. Res., 75 (14), 2625– 2647. doi:10.1029/JB075i014p02625.

Di Giulio, A., Ronchi, A., Sanfilippo, A., Tiepolo, M., Pimentel, M., Ramos, V.A., 2012. Detrital zircon provenance from the Neuquén Basin (south-central Andes): Cretaceous geodynamic evolution and sedimentary response in a retroarc-foreland basin. Geology, 40, 559-562.

Dodson, M.H., 1973. Closure Temperature in Cooling Geochronological and Petrological Systems. Contr. Mineral. Petrol., 40, 259-274.

Dunai, T.J., López, G.A.G., Juez-Larré, J., 2005. Oligocene–Miocene age of aridity in the Atacama Desert revealed by exposure dating of erosion-sensitive landforms. Geology, 33 (4), 321-324.

Dunn, J.F., Hartshorn, K.G., Hartshorn, P.W., 1995. Structural styles and hydrocarbon potential of the Sub-Andean thrust belt of southern Bolivia, in: Tankard, A.J., Suárez, R., Welsink, H.J. (Eds.), Petroleum basins of South America. Am. Assoc. Petrol. Geol. Mem., 62, 523–543

Echavarria, L., Hernández, R., Allmendinger, R., Reynolds, J., 2003. Subandean thrust and fold belt of northwestern Argentina: geometry and timing of the Andean evolution. Am. Assoc. Petrol. Geol. Bull. 87, 965–985.

Ege, H., Sobel, E.R., Scheuber, E., Jacobshagen, V., 2007. Exhumation history of the southern Altiplano plateau (southern Bolivia) constrained by apatite fission track thermochronology. Tectonics, 26 (TC1004). doi:10.1029/2005TC001869

Egholm, D.L., Nielsen, S.B., Pedersen, V.K., Lesemann, J.E., 2009. Glacial effects limiting mountain height. Nature, 460 (7257), 884.

Ehlers, T.A., Poulsen, C.J., 2009. Influence of Andean uplift on climate and paleoaltimetry estimates. Earth Planet Sci. Lett., 281 (3), 238-248.

Elger, K., Oncken, O., Glodny, J., 2005. Plateau-style accumulation of deformation: Southern Altiplano. Tectonics, 24 (TC4020). doi: 10.1029/2004TC001675

Eichelberger, N., McQuarrie, N., Ehlers, T.A., Enkelmann, E., Barnes, J. B., Lease, R.O., 2013. New constraints on the chronology, magnitude, and distribution of deformation within the central Andean orocline. Tectonics, 32 (5), 1432-1453.

England, P., Molnar, P., 1990. Surface uplift, uplift of rocks, and exhumation of rocks. Geology, 18, 1173-1177.

Evenstar, L.A., Hartley, A.J., Stuart, F.M., Mather, A.E., Rice, C.M., Chong, G., 2009. Multiphase development of the Atacama Planation Surface recorded by cosmogenic ^{3}He exposure ages: Implications for uplift and Cenozoic climate change in western South America. Geology, 37 (1): 27–30. doi:10.1130/G25437A.1

Evenstar, L.A., Stuart, F.M., Hartley, A.J., Tattitch, B., 2015. Slow Cenozoic uplift of the western Andean Cordillera indicated by cosmogenic ^{3}He in alluvial boulders from the Pacific Planation Surface. Geophys. Res. Lett., 42 (20), 8448-8455.

Faccenna, C., Oncken, O., Holt, A.F., Becker, T.W., 2017. Initiation of the Andean orogeny by lower mantle subduction. Earth Planet. Sci. Lett., 463, 189-201.

Farías, M., Charrier, R., Comte, D., Martinod, J., Hérail, G., 2005. Late Cenozoic deformation and uplift of the western flank of the Altiplano: Evidence from the depositional, tectonic, and geomorphologic evolution and shallow seismic activity (northern Chile at 19°30S). Tectonics, 24, TC4001. doi: 10.1029/2004TC001667

Farías, M., Charrier, R., Carretier, S., Martinod, J., Fock, A., Campbell, D., Cáceres, J., Comte, D., 2008. Late Miocene high and rapid surface uplift and its erosional response in the Andes of central Chile (33°–35°S). Tectonics, 27 (1). doi:10.1029/2006TC002046

Farías, M., Comte, D., Charrier, R., Martinod, J., David, C., Tassara, A., Tapia, F., Fock, A., 2010. Crustal-scale structural architecture in central Chile based on seismicity and surface geology: Implications for Andean mountain building. Tectonics, 29 (3).

Farley, K.A., 2000. Helium diffusion from apatite: general behavior as illustrated by Durango fluorapatite. J. Geophys. Res., 105, 2903-2914

Fiorella, R.P., Poulsen, C.J., Zolá, R.S.P., Jeffery, M.L., Ehlers, T.A., 2015. Modern and long-term evaporation of central Andes surface waters suggests paleo archives underestimate Neogene elevations. Earth Planet Sci. Lett., 432, 59-72.

Fitzgerald, P. G., Sorkhabi, R.B., Redfield, T.F., Stump, E., 1995. Uplift and denudation of the central Alaska Range: A case study in the use of apatite fission track thermochronology to determine absolute uplift parameters. J. Geophys. Res., 100 (B10), 175-191. doi:10.1029/95JB02150.

Flament, N., Gurnis, M., Müller, R.D., Bower, D.J, Husson, L., 2015. Influence of subduction history on South American topography. Earth Planet Sci. Lett., 430, 9-18.

Fennell, L.M., Folguera, A., Naipauer, M., Gianni, G., Rojas Vera, E.A., Bottesi, G. Ramos, V.A., 2017. Cretaceous deformation of the southern Central Andes: synorogenic growth strata in the Neuquén Group (35° 30′–37°S). Basin Res., 29, 51-72.

Fock, A., Charrier, R., Farías, M., Muñoz, M., 2006. Fallas de vergencia oeste en la Cordillera Principal de Chile central: Inversión de la cuenca de Abanico (33°–34°S). Asoc. Geol. Argent., Publ. Espec. 6, 48–55.

Folguera, A., Rojas Vera, E., Bottessi, G., Zamora Valcarce, G., Ramos, V.A., 2010. The Loncopué trough: A Cenozoic basin produced by extension in the southern central Andes. J. Geodyn., 49, 287–295.

Fosdick, J.C., Reat, E.J., Carrapa, B., Ortiz, G., Alvarado, A., 2017. Retroarc basin reorganization and aridification during Paleogene uplift of the southern central Andes. Tectonics, 36, 493-514. doi:10.1002/2016TC004400

Fox, M., Herman, F., Willett, S.D., May, D.A., 2014. A linear inversion method to infer exhumation rates in space and time from thermochronometric data. Earth Surf. Dyn., 2, 47-65. doi:10.5194/esurf-2-47-2014.

Fox, M., Herman, F., Kissling, E., Willett, S.D., 2015. Rapid exhumation in the Western Alps driven by slab detachment and glacial erosion. Geology, 43 (5), 379–382. doi: 10.1130/G36411.1

Francis, P.W., Hawkesworth, C.J., 1994. Late Cenozoic rats of magmatic activity in the Central Andes and the relationships to continental crust formation and thickening. J. Geol. Soc. London, 151, 845-854.

Gans, C.R., Beck, S.L., Zandt, G., Gilbert, H., Alvarado, P., Anderson, M., Linkimer, L., 2011. Continental and oceanic crustal structure of the Pampean flat slab region, western Argentina, using receiver function analysis: new high-resolution results. Geophys. J. Int., 186 (1), 45-58.

Gansser, A. (1973). Facts and theories on the Andes: twenty-sixth William Smith Lecture. Journal of the Geological Society, 129(2), 93-131.

Garcia, M., Hérail, G., 2005. Fault-related folding, drainage network evolution and valley incision during the Neogene in the Andean Precordillera of Northern Chile. Geomorphology, 65(3-4), 279-300.

García, M., Riquelme, R., Farías, M., Hérail, G., Charrier, R., 2011. Late Miocene–Holocene canyon incision in the western Altiplano, northern Chile: tectonic or climatic forcing?. Journal of the Geological Society, 168 (4), 1047-1060.

García, V.H., Casa A.L., 2014. Quaternary tectonics and seismic potential of the Andean retrowedge at 33–34°S, in: Sepúlveda, S.A., Giambiagi, L.B., Moreiras, S.M., Pinto, L., Tunik, M., Hoke, G.D., Farías, M. (Eds.), Geodynamic Processes in the Andes of Central Chile and Argentina. Geol. Soc. London Spec. Pub., 399, pp. 311-327. doi: 10.1144/SP399.14.

Garreaud, R.D., 2007. Precipitation and circulation covariability in the extratropics. Jour. Clim., 20(18), 4789-4797.

Garreaud, R.D., 2009. The Andes climate and weather. Adv. Geosci., 22, 3-11.

Garreaud, R.D., Vuille, M., Compagnucci, R., Marengo, J., 2009. Present-day South American climate. Palaeogeogr., Palaeoclimatol., Palaeoecol., 281 (3-4), 180-195.

Garzione, C.N., McQuarrie, N., Perez, N.D., Ehlers, T.A., Beck, S.L., Kar, N., Eichelberger, N., Chapman, A.D., Ward, K.M., Ducea, M.N., Lease, R.O., Poulsen, C.J., Wagner, L.S., Saylor, J.E., Zandt, G., Horton, B.K., 2017. Tectonic evolution of the Central Andean plateau and implications for the growth of plateaus. Ann. Rev. Earth Planet. Sci., 45, 529-559.

Gayó, E., Hinojosa, L.F., Villagrán, C., 2005. On the persistence of Tropical Paleofloras in central Chile during the Early Eocene. Rev. Palaeobot. Palyno., 137(1-2), 41-50.

Gephart, J.W., 1994. Topography and subduction geometry in the central Andes: Clues to the mechanics of a noncollisional orogen. Journal of Geophysical Research: Solid Earth, 99(B6), 12279-12288.

Giambiagi, L.B., Ramos, V.A., 2002. Structural evolution of the Andes in a transitional zone between flat and normal subduction (33°30′–33°45′S), Argentina and Chile. J. S. Am. Earth Sci., 15 (1), 101-116.

Giambiagi, L.B., Tunik, M.A., Ghiglione, M., 2001. Cenozoic tectonic evolution of the Alto Tunuyán foreland basin above the transition zone between the flat and normal subduction segment (33°30′–34°S), western Argentina. J. S. Am. Earth Sci., 14 (7), 707-724.

Giambiagi, L.B., Ramos, V.A., Godoy, E., Pamela Alvarez, P., Orts, S., 2003. Cenozoic deformation and tectonic style of the Andes, between 33° and 34° south latitude. Tectonics, 22, 4, 1041, doi:10.1029/2001TC001354

Giambiagi, L., Mescua, J., Bechis, F., Tassara, A., Hoke, G., 2012. Thrust belts of the southern Central Andes: Along-strike variations in shortening, topography, crustal geometry, and denudation. Geol. Soc. Am. Bull., 124 (7-8), 1339–1351. doi: 10.1130/B30609.1.

Giambiagi, L., Tassara, A., Mescua, J., Tunik, M., Alvarez, P.P., Godoy, E., Hoke, G., Pinto, L., Spagnotto, S., Porras, H., Tapia, F., Jara, P., Bechis, F., Garcia, V.H., Suriano, J., Moreira, S.M, Pagano, S.D., 2015a. Evolution of shallow and deep structures along the Maipo-Tunuyan transect (33°40'S): from the Pacific coast to the Andean foreland, in: Sepúlveda, S.A., Giambiagi, L.B., Moreiras, S.M., Pinto, L., Tunik, M., Hoke, G.D., Farías, M. (Eds.), Geodynamic Processes in the Andes of Central Chile and Argentina. Geol. Soc. London. Spec. Publ., 399, doi: 10.1144/SP399.14.

Giambiagi, L., Spagnotto, S., Moreiras, S.M., Gómez, G., Stahlschmidt, E., Mescua, J., 2015b. Three-dimensional approach to understanding the relationship between the Plio-Quaternary stress field and tectonic inversion in the Triassic Cuyo Basin, Argentina. Solid Earth, 6 (2), 747-763. doi: 10.5194/se-6-747-2015

Giese, P., Scheuber, E., Schilling, F., Schmitz, M., Wigger, P., 1999. Crustal thickening processes in the Central Andes and the different natures of the Moho-discontinuity. J. S. Am. Earth Sci., 12 (2), 201-220.

Gillis, R.J., Horton, B. K., Grove, M., 2006. Thermochronology, geochronology, and upper crustal structure of the Cordillera Real: Implications for Cenozoic exhumation of the central Andean plateau. Tectonics, 25(6).

Gleadow, A.J.W, Fitzgerald, P.G., 1987. Uplift history and structure of the Transantarctic Mountains: new evidence from fission track dating of basement apatites in the Dry Valleys area, southern Victoria Land. Earth Planet. Sci. Lett., 82 (1–2), 1-14. doi:10.1016/0012-821X(87)90102-6.

Gleadow, A.J.W, Duddy, I.R., Green, P.F., Lovering, J.F., 1986. Confined fission track lengths in apatite: a diagnostic tool for thermal history analysis. Contrib. Mineral. Petrol., 94, 405-415.

Gourou, P., Papy, L., 1966. Compendio de geografía general. Ediciones RIALP, Madrid.

Grier, M.E., Salfity, J.A., Allmendinger, R.W., 1991. Andean reactivation of the Cretaceous Salta rift, northwestern Argentina, J. S. Am. Earth Sci., 4, 351 – 372.

Gregori, D., Benedini, L., 2013. The Cordon del Portillo Permian magmatism, Mendoza, Argentina, plutonic and volcanic sequences at the western margin of Gondwana. J. S. Am. Earth Sci., 42, 61-73.

Gubbels, T.L., Isacks, B.L., Farrar, E., 1993. High-level surfaces, plateau uplift, and foreland development, Bolivian central Andes. Geology, 21, 695-698.

Godoy, E., Yañez, G., Vera, E., 1999. Inversion of an Oligocene volcano-tectonic basin and uplifting of its superimposed Miocene magmatic arc in the central Chilean Andes: first seismic and gravity evidences. Tectonophysics, 306, 217-236.

Hain, M.P., Strecker, M.R., Bookhagen, B., Alonso, R.N., Pingel, H. Schmitt, A.K., 2011. Neogene to Quaternary broken foreland formation and sedimentation dynamics in the Andes of NW Argentina (25°S). Tectonics, 30, TC2006. doi:10.1029/2010TC002703

Harrison, S., 2004. The Pleistocene glaciations of Chile, in: Ehlers., J., Gibbard, P.L. (Eds.), Quaternary Glaciations – Extent and Chronology. Part III: South America, Asia, Africa, Australasia, Antarctica. Elsevier, Cambridge, pp. 89-103.

Haselton, K., Hilley, G., Strecker, M.R., 2002. Average Pleistocene climatic patterns in the southern central Andes: Controls on mountain glaciation and paleoclimate implications. J. Geol., 110 (2), 211-226.

Hartley, A.J., Flint, S., Turner, P., Jolley, E.J., 1992. Tectonic controls on the development of a semi-arid, alluvial basin as reflected in the stratigraphy of the Purilactis Group (Upper Cretaceous–Eocene), northern Chile. J. S. Am. Earth Sci., 5, 273–294.

Hartley, A.J., Chong, G., Houston, J., Mather, A.E., 2005. 150 million years of climatic stability: evidence from the Atacama Desert, northern Chile. J. Geol. Soc., 162 (3), 421-424.

Hein, A.S., Cogez, A., Darvill, C.M., Mendelova, M., Kaplan, M.R., Herman, F., Dunai, T.J., Norton, K., Xu, S., Christl, M., Rodés, Á., 2017. Regional mid-Pleistocene glaciation in central Patagonia. Quat. Sci. Rev., 164, 77-94.

Herman, F., Brandon, M., 2015. Mid-latitude glacial erosion hotspot related to equatorial shift in southern Westerlies. Geology, 43 (11), 987-990. doi: 10.1130/G37008.1

Herman, F., Champagnac, J.D., 2016. Plio-Pleistocene increase of erosion rates in mountain belts in response to climate change. Terra Nova, 28 (1), 2-10.

Herman, F., Seward, D., Valla, P.G., Carter, A., Kohn, B., Willett, S.D., Ehlers, T.A., 2013. Worldwide acceleration of mountain erosion under a cooling climate. Nature, 504, 423-426. doi:10.1038/nature12877

Herman, F., Braun, J., Deal, E., Prasiçek, G., 2018. The response time of glacial erosion. J. Geophys. Res. Earth Surf., 123 (4), 801-817.

Herrera, M. (2016). Estimación de las altitudes de las líneas de equilibrio en glaciares de montaña para el último ciclo glacial-interglacial en los Andes de Santiago, Chile Central. Tesis de Posgrado. Universidad de Chile, Departamento de Geología, Santiago, Chile.

Herrera, S., Pinto, L., Deckart, K., Cortés, J., Valenzuela, J., 2017. Cenozoic tectonostratigraphic evolution and architecture of the Central Andes in northern Chile based on the Aquine region, Western Cordillera (19°-19°30’ S). Andean Geol., 44 (2), 87-122. doi: 10.5027/andgeoV44n2-a01

Hervé, F., Fanning, C.M., Calderón, M., Mpodozis, C., 2014. Early Permian to Late Triassic batholiths of the Chilean Frontal Cordillera (28°–31°S): SHRIMP U–Pb zircon ages and Lu–Hf and O isotope systematics. Lithos, 184, 436-446.

Heusser C.J. 1983. Quaternary pollen record from Laguna de Tagua Tagua, Chile. Science 219: 1429–1432.

Hijmans, R.J., Cameron, S.E., Parra, J.L., Jones, P.G., Jarvis, A., 2005. Very high resolution interpolated climate surfaces for global land areas. Int. J. Climatol., 25 (15), 1965-1978.

Hilley, G.E., Strecker, M.R., 2005. Processes of oscillatory basin filling and excavation in a tectonically active orogen: Quebrada del Toro Basin, NW Argentina. Geol. Soc. Am. Bull., 117 (7-8), 887-901.

Hilley, G.E., Coutand, I., 2010. Links between topography, erosion, rheological heterogeneity, and deformation in contractional settings: Insights from the central Andes. Tectonophysics, 495, 78-92, doi:10.1016/j.tecto.2009.06.017.

Hilley, G.E., Blisniuk, P.M., Strecker, M.R., 2005. Mechanics and erosion of basement-cored uplift provinces. Jour. Geophys. Res., 110, B12409

Hinojosa, L.F., 2005. Cambios climáticos y vegetacionales inferidos a partir de paleofloras cenozoicas del sur de Sudamérica. Rev. Geol. Chile, 32(1), 95-115.

Höfer-Öllinger, G., Millen, B., 2010. Geothermal prognoses for tunnels in the Andes. Geomech. Tunnelling, 3 (5), 622-633.

Hoke, G.D., Garzione, C.N., 2008. Paleosurfaces, paleoelevation, and the mechanisms for the late Miocene topographic development of the Altiplano plateau. Earth Planet. Sci. Lett., 271(1-4), 192-201.

Hoke, G. D., Isacks, B. L., Jordan, T. E., Blanco, N., Tomlinson, A. J., Ramezani, J., 2007. Geomorphic evidence for post-10 Ma uplift of the western flank of the central Andes 18 30′–22 S. Tectonics, 26(5).

Hoke, G.D., Giambiagi, L.B., Garzione, C.N., Mahoney, J.B. and Strecker, M.R., 2014. Neogene paleoelevation of intermontane basins in a narrow, compressional mountain range, southern Central Andes of Argentina. Earth and Planetary Science Letters, 406, pp.153-164.

Hongn, F., del Papa, C., Powell, J., Petrinovic, I., Mon, R., Deraco, V., 2007. Middle Eocene deformation and sedimentation in the Puna-Eastern Cordillera transition (23-26°S): Control by preexisting heterogeneities on the pattern of initial Andean shortening. Geology, 35 (3), 271-274.

Houston, J., Hartley, A.J., 2003. The central Andean west-slope rainshadow and its potential contribution to the origin of hyper-aridity in the Atacama Desert. Int. J. Climatol., 23, 1453-1464. doi:10.1002/joc.938

Horton, B.K., 1999. Erosional control on the geometry and kinematics of thrust belt development in the central Andes. Tectonics, 18, 1292–304

Horton, B.K., 2005. Revised deformation history of the central Andes: Inferences from Cenozoic foredeep and intermontane basins of the Eastern Cordillera, Bolivia. Tectonics, 24, doi:10.1029/2003TC001619.

Horton, B.K., 2018a. Sedimentary record of Andean mountain building. Earth-Sci. Rev., 178, 279-309.

Horton, B.K., 2018b. Tectonic regimes of the central and southern Andes: Responses to variations in plate coupling during subduction. Tectonics, 37. doi:10.1002/2017TC004624

Horton, B.K., DeCelles, P.G., 1997. The modern foreland basin system adjacent to the Central Andes. Geology 25, 895–898.

Horton B.K, DeCelles P.G., 2001. Modern and ancient fluvial megafans in the foreland basin system of the central Andes, southern Bolivia: implications for drainage network evolution in fold-thrust belts. Basin Res., 13, 43–63.

Horton, B.K., Hampton, B.A., Waanders, G.L., 2001. Paleogene synorogenic sedimentation in the Altiplano plateau and implications for initial mountain building in the central Andes. Geol. Soc. Am. Bull., 113 (11), 1387-1400.

Horton, B.K., Fuentes, F., Boll, A., Starck, D., Ramirez, S. G., Stockli, D.F., 2016. Andean stratigraphic record of the transition from backarc extension to orogenic shortening: A case study from the northern Neuquén Basin, Argentina. J. S. Am. Earth Sci., 71, 17-40.

Insel, N., Poulsen, C.J., Ehlers, T.A., 2010. Influence of the Andes Mountains on South American moisture transport, convection, and precipitation. Clim. Dyn., 35 (7-8), 1477-1492.

Irigoyen, M.V., Buchan, K.L. Brown, R.L., 2000. Magnetostratigraphy of Neogene Andean foreland-basin strata, lat 33°S, Mendoza Province, Argentina. Geol. Soc. Am. Bull., 112 (6), 803-816.

Isacks, B.,1988. Uplift of the central Andean plateau and bending of the Bolivian orocline. Jour. Geophys. Res., Solid Earth and Planets, 93, 3211–3231.

Jamieson, R.A., Beaumont, C., 1988. Orogeny and metamorphism: A model for deformation and pressure-temperature-time paths with application to the central and southern Appalachians. Tectonics, 7, 417-445.

Jenny B., Wilhelm D., Valero-Garcés B.L., 2003. The southern westerlies in Central Chile: Holocene precipitation estimates based on a water balance model for Laguna Aculeo (33° 50’ S). Climate Dynamics, 20, 269–280.

Jiao, R., Herman, F., Seward, D., 2017. Late Cenozoic exhumation model of New Zealand: Impacts from tectonics and climate. Earth-Sci. Rev., 166, 286-298.

Jones, R.E., Kirstein, L.A., Kasemann, S.A., Dhuime, B., Elliott, T., Litvak, V.D., Alonso, R., Hinton, R., Facility, E.I.M., 2015. Geodynamic controls on the contamination of Cenozoic arc magmas in the southern Central Andes: Insights from the O and Hf isotopic composition of zircon. Geochim. Cosmochim. Acta, 164, 386-402. doi.org/10.1016/j.gca.2015.05.007

Jordan, T.E., Isacks, B.L., Allmendinger, R.W., Brewer, J.A., Ramos, V.A., Ando, C.J., 1983. Andean tectonics related to the geometry of the subducted Nazca Plate. Geol. Soc. Am. Bull., 94, 341–61.

Jordan, T.E., Allmendinger, R.W., Damanti, J.F., Drake, R., 1993. Chronology of Motion in a Complete Thrust Belt: The Precordillera, 30-31°S, Andes Mountains. J. Geol., 101, 135-156.

Jordan, T.E., Schlunegger, F., Cardazo, N., 2001a. Unsteady and spatially variable evolution of the Neogene Andean Bermejo foreland basin, Argentina. J. S. Am. Earth Sci., 14, 775-798.

Jordan, T.E., Burns, W.M., Veiga, R., Pángaro, F., Copeland, P., Kelley, S., Mpodozis, C., 2001b. Extension and basin formation in the southern Andes caused by increased convergence rate: A mid-Cenozoic trigger for the Andes. Tectonics, 20, 308–324. doi:10.1029/1999TC001181.

Jordan, T.E., Mpodozis, C., Muñoz, N., Blanco, N., Pananont, P., Gardeweg, M., 2007. Cenozoic subsurface stratigraphy and structure of the Salar de Atacama Basin, northern Chile. J. S. Am. Earth Sci., 23, 122–146. doi:10.1016/j.jsames.2006.09.024

Jordan, T.E., Nester, P.L., Blanco, N., Hoke, G. D., Dávila, F., Tomlinson, A.J., 2010. Uplift of the Altiplano-Puna plateau: A view from the west. Tectonics, 29 (TC5007). doi:10.1029/2010TC002661

Jordan, T.E., Kirk-Lawlor, N.E., Blanco, N.P, Rech, J.A., Cosentino, N.J., 2014. Landscape modification in response to repeated onset of hyperarid paleoclimate states since 14 Ma, Atacama Desert, Chile. Geol. Am. Soc. Bull., 126 (7-8), 1016-1046. doi:10.1130/B30978.1

Kay, S.M., Mpodozis, C., 2002. Magmatism as a probe to the Neogene shallowing of the Nazca plate beneath the modern Chilean flat-slab. Earth Planet. Sci. Lett., 15, 39-57.

Kay, S.M., Mpodozis, C., Ramos, V.A., Munizaga, F., 1991. Magma source variations for mid-late Tertiary magmatic rocks associated with a shallowing subduction zone and a thickening crust in the central Andes (28 to 33°S). Geol. Soc. Am. Spec. Publ., 265, 113-137.

Kay, S.M., Mpodozis, C., Tittler, A., Cornejo, P., 1994. Tertiary magmatic evolution of the Maricunga mineral belt in Chile. Int. Geol. Rev., 36 (12), 1079-1112.

Kay, S.M., Godoy, E., Kurtz, A., 2005. Episodic arc migration, crustal thickening, subduction erosion, and magmatism in the south-central Andes. Geol. Am. Soc. Bull., 117 (1), 67-88.

Kay, S.M., Coira, B.L., Caffe, P.J., Chen, C.H., 2010. Regional chemical diversity, crustal and mantle sources and evolution of central Andean Puna plateau ignimbrites. J. Volcanol. Geotherm. Res., 198 (1-2), 81-111.

Kay, S.M., Mpodozis, C., Gardeweg, M., 2014. Magma sources and tectonic setting of Central Andean andesites (25.5–28°S) related to crustal thickening, forearc subduction erosion and delamination. Geol. Soc. London Spec. Publ., 385 (1), 303-334.

Ketcham R.A., Donelick, R.A, Carlson, W.D., 1999. Variability of apatite fission-track annealing kinetics. III. Extrapolation to geological time scales. Am. Mineral., 84, 1235-1255.

Klein, A.G., Seltzer, G.O., Isacks, B.L., 1999. Modern and last local glacial maximum snowlines in the Central Andes of Peru, Bolivia, and Northern Chile. Quat. Sci. Rev., 18 (1), 63-84.

Kleinert, K., Strecker, M.R., 2001. Climate change in response to orographic barrier uplift: Paleosol and stable isotope evidence from the late Neogene Santa Maria basin, northwestern Argentina. Geol. Soc. Am. Bull., 113 (6), 728-742.

Kley, J., 1996. Transition from basement involved to thin-skinned thrusting in the Cordillera Oriental of southern Bolivia. Tectonics, 15, 763– 775.

Kley, J., Monaldi, C.R., 1998. Tectonic shortening and crustal thickness in the Central Andes: how good is the correlation?. Geology, 26, 723–726.

Kley, J., Monaldi, C.R., 2002. Tectonic inversion in the Santa Barbara System of the central Andean foreland thrust belt, northwestern Argentina. Tectonics, 21 (6), 1061, 1-18. doi:10.1029/2002TC902003

Kley, J., Monaldi, C.R., Salfity, J. A., 1999. Along-strike segmentation of the Andean foreland: causes and consequences. Tectonophysics, 301(1-2), 75-94.

Kodama, Y.-M., 1992. Large-scale common features of subtropical precipitation zones (the Baiu Frontal Zone, the SPCZ, and the SACZ): Part I: Characteristics of subtropical frontal zones. J. Meteor. Soc. Japan, 70, 813-835.

Konstantinovskaia, E., Malavieille, J., 2005. Erosion and exhumation in accretionary orogens: Experimental and geological approaches. Geochemistry, Geophysics, Geosystems, 6(2).

Koons, P.O., 1989. The topographic evolution of collisional mountain belts: A numerical look at the Southern Alps, New Zealand. Am. Jour. Sci., 289, 1041-1069.

Koons, P.O, 1990. Two-sided orogen: Collision and erosion from the sandbox to the Southern Alps, New Zealand. Geology, 18 (8), 679-682.

Kraemer, B., Adelmann, D., Alten, M., Schnurr, W., Erpenstein, K., Kiefer, E., Van den Bogaard, P., Görler, K., 1999. Incorporation of the Paleogene foreland into the Neogene Puna plateau: the Salar de Antofalla area, NW Argentina. J. S. Am. Earth Sci., 12 (2), 157-182.

Kurtz, A.C., Kay, S.M., Charrier, R. and Farrar, E., 1997. Geochronology of Miocene plutons and exhumation history of the El Teniente region, Central Chile (34-35°S). Andean Geol., 24 (1), 75-90.

Lamb, S., Davis, P., 2003. Cenozoic climate change as a possible cause for the rise of the Andes. Nature, 425 (6960), 792-797.

Lamb, S., Hoke, L., Kennan, L., Dewey, J. 1997. Cenozoic evolution of the Central Andes in Bolivia and northern Chile. Geol. Soc. Lond. Spec. Publ., 121, 237–264.

Lamy, F., Hebbeln, D., Wefer, G., 1999. High-resolution marine record of climatic change in mid-latitude Chile during the last 28,000 years based on terrigenous sediment parameters. Quat. Res., 51, 83– 93.

Lamy, F., Hebbeln, D., Röhl, U., Wefer, G., 2001. Holocene rainfall variability in southern Chile: a marine record of latitudinal shifts of the Southern Westerlies. Earth Planet. Sci. Lett., 185 (3-4), 369-382.

Lamy, F., Kilian, R., Arz, H.W., Francois, J.P., Kaiser, J., Prange, M., Steinke, T., 2010. Holocene changes in the position and intensity of the southern westerly wind belt. Nat. Geosci., 3(10), 695-699.

Leeman, W.P., 1983. The influence of crustal structure on compositions of subduction-related magmas. J. Volcanol. Geoth. Res., 18, 561-588. doi: 10.1016/0377-0273(83)90026-4.

Lehner, B., Grill G., 2013. Global river hydrography and network routing: baseline data and new approaches to study the world's large river systems. Hydrol. Process., 27 (15), 2171–2186.

Leier, A.L., DeCelles, P.G., Pelletier, J.D., 2005. Mountains, monsoons, and megafans. Geolog, 33(4), 289-292.

Lenters, J.D., Cook, K.H., 1995. Simulation and Diagnosis of the Regional Summertime Precipitation Climatology of South America. Jour. Clim., 8, 2988-3005.

Lenters, J.D., Cook, K.H., 1997. On the Origin of the Bolivian High and Related Circulation Features of the South American Climate. Jour. Atm. Sci., 54, 656-677.

Lenters, J.D., Cook, K.H., 1999. Summertime precipitation variability over South America: Role of the large-scale circulation. Monthly Weather Rev., 127 (3), 409-431.

Le Roux, J.P., 2012. A review of Tertiary climate changes in southern South America and the Antarctic Peninsula. Part 2: continental conditions. Sediment. Geol., 247, 21-38.

Litvak, V. D., Poma, S., Kay, S. M., Valle, E., 2007. Paleogene and Neogene magmatism in the Valle del Cura region: New perspective on the evolution of the Pampean flat slab, San Juan province, Argentina. J. S. Am. Earth Sci., 24, 117–137.

Löbens, S., Sobel, E.R., Bense, F.A., Wemmer, K., Dunkl, I., Siegesmund, S., 2013. Refined exhumation history of the northern Sierras Pampeanas, Argentina. Tectonics, 32(3), 453-472.

Lossada, A.C., Giambiagi, L., Hoke, G.D., Fitzgerald, P.G., Creixell, C., Murillo, I., Mardonez, D., Velásquez, R., Suriano, J., 2017. Thermochronologic evidence for late Eocene Andean mountain building at 30°S. Tectonics, 36 (11), 2693-2713.

Maksaev, V., Zentilli, M., 1999. Fission Track Thermochronology of the Domeyko Cordillera, Northern Chile: Implication for Andean Tectonics and Porphyry Copper Metallogenesis. Explor. Min. Geol., 8(1-2); 65-89.

Maksaev, V., Munizaga, F., Zentilli, M., Charrier, R., 2009. Fission track thermochronology of Neogene plutons in the Principal Andean Cordillera of central Chile (33-35°S): Implications for tectonic evolution and porphyry Cu-Mo mineralization. Andean Geol., 36(2), 153-171.

Malavieille, J. (1984), Modélisation expérimentale des chevauchements imbriques: Application aux chaînes de montagnes, Bull. Soc. Geol. Fr., 26, 129–138.

Mamani, M., Wörner, G., Sempere, T., 2010a. Geochemical variations in igneous rocks of the Central Andean orocline (13°S to 18°S): Tracing crustal thickening and magma generation through time and space. Geol. Soc. Am. Bull., 122(1-2), 162-182. doi: 10.1130/B26538.1

[dataset] Mamani, M., Wörner, G., Sempere, T., 2010b. The Central Andes Geochemical GPS database. University of Göttingen. http://www.uni-geochem.gwdg.de/en/andes-database.

Mancktelow, N.S., Grasemann, B., 1997. Time-dependent effects of heat advection and topography on cooling histories during erosion. Tectonophysics, 270, 167-195.

Marengo, J. A., Soares, W. R., Saulo, C., Nicolini, M., 2004. Climatology of the Low-Level Jet East of the Andes as derived from the NCEP–NCAR Reanalyses: Characteristics and Temporal Variability. Journal of climate, 17(12), 2261-2280.

Marengo, J. A., Liebmann, B., Grimm, A. M., Misra, V., Silva Dias, P. L. D., Cavalcanti, I. F. A., Carvalho, L. M. V., …, Alves, L.M., 2012. Recent developments on the South American monsoon system. International Journal of Climatology, 32(1), 1-21.

Marquillas, R.A., Del Papa, C., Sabino, I.F., 2005. Sedimentary aspects and paleoenvironmental evolution of a rift basin: Salta Group (Cretaceous–Paleogene), northwestern Argentina. International Journal of Earth Sciences, 94(1), pp.94-113.

Martínez, F., Arriagada, C., Peña, M., Deckart, K., Charrier, R., 2016. Tectonic styles and crustal shortening of the Central Andes “Pampean” flat-slab segment in northern Chile (27°–29°S). Tectonophysics, 667, 144–162.

Martínez F., Arriagada C., Bascuñán S., 2018. Mechanisms and episodes of deformation along the Chilean–Pampean flat-slab subduction segment of the Central Andes in Northern Chile, in: Folguera, A., Contreras Reyes, E., Heredia, N., Encinas, A., B. Iannelli, S., Oliveros, V., M. Dávila, F., Collo, G., Giambiagi, L., Maksymowicz, A., Iglesia Llanos, M.P., Turienzo, M., Naipauer, M., Orts, D., D. Litvak, V., Alvarez, O., Arriagada, C. (Eds.), The Evolution of the Chilean-Argentinean Andes. Springer Earth System Sciences. Springer, Cham, Switzerland, pp. 273-290.

Martinod, J., Husson, L., Roperch, P., Guillaume, B., Espurt, N., 2010. Horizontal subduction zones, convergence velocity and the building of the Andes. Earth Planet. Sci. Lett., 299 (3), 299-309.

Masek, J.G., Isacks, B.L., Gubbels, T.L., Fielding, E.J., 1994. Erosion and tectonics at the margins of continental plateaus. J. Geophys. Res., 99 (B7), 13,941-13,956.

McNutt, R.H., Crocket, J.H., Clark, A.H., Caelles, J.C., Farrar, E., Haynes, S.J., Zentilli, M., 1975. Initial ^{87}Sr/^{86}Sr ratios of plutonic and volcanic rocks of the central Andes between latitudes 26° and 29°South. Earth Planet. Sci. Lett., 27(2), 305-313. doi: 10.1016/0012-821X(75)90042-4

McQuarrie, N., 2002, The kinematic history of the central Andean fold-thrust belt, Bolivia: Implications for building a high plateau: Geol. Soc. Am. Bull., 114, 950–963.

McQuarrie, N., DeCelles, P., 2001. Geometry and structural evolution of the central Andean backthrust belt, Bolivia. Tectonics, 20 (5), 669-692.

McQuarrie, N., Horton, B.K., Zandt, G., Beck, S. DeCelles, P.G., 2005. Lithospheric evolution of the Andean fold–thrust belt, Bolivia, and the origin of the central Andean plateau. Tectonophysics, 399 (1-4), 15-37.

Mercer, J.H., Sutter, J.F., 1982. Late Miocene - earliest Pliocene glaciation in southern Argentina: Implications for global ice sheet history. Palaeogeogr., Palaeoclimatol., Palaeoecol., 38, 185-206.

Mitrovica, J.X., Beaumont, C., Jarvis, G.T., 1989. Tilting of continental interiors by the dynamical effects of subduction. Tectonics, 8 (5), 1079-1094.

Molnar, P., 2004. Late Cenozoic increase in accumulation rates of terrestrial sediment: How might climate change have affected erosion rates?, Annu. Rev. Earth Planet. Sci., 32, 67-89.

Molnar, P., 2009. The state of interactions among tectonics, erosion, and climate: A polemic. Geol. Soc. Am. Today, 19 (7), 44-45.

Molnar, P., England, P., 1990. Late Cenozoic Uplift of Mountain-Ranges and Global Climate Change - Chicken or Egg?. Nature, 346(6279), 29-34.

Montero-López, C., del Papa, C., Hongn, F., Strecker, M. R. and Aramayo, A., 2016. Synsedimentary broken-foreland tectonics during the Paleogene in the Andes of NW Argentine: new evidence from regional to centimetre-scale deformation features. Basin Res., 30, 142-159. doi:10.1111/bre.12212

Montgomery, D.R., Balco, G., Willett, S.D., 2001. Climate, tectonics, and the morphology of the Andes. Geology, 29 (7), 579-582.

Mpodozis, C., Ramos, V., 1989. The Andes of Chile and Argentina, in: Ericksen, G.E., Cañas Pinochet, M.T., Reinemund, J.A. (Eds.), Geology of the Andes and its relation to hydrocarbon and mineral resources. Circum-Pacific Counc. Energy Miner. Resour. Earth Sci. Ser. 11, Housten, Texas, pp. 59-90.

Mpodozis, C., Arriagada, C., Basso, M., Roperch, P., Cobbold, P., Reich, M., 2005. Late Mesozoic to Paleogene stratigraphy of the Salar de Atacama Basin, Antofagasta, Northern Chile: Implications for the tectonic evolution of the Central Andes. Tectonophysics, 399 (1-4), 125-154. doi: 10.1016/j.tecto.2004.12.019

Muir, D.D., Barfod, D.N., Blundy, J.D., Rust, A.C., Sparks, R.S.J., Clarke, K.M., 2015. The temporal record of magmatism at Cerro Uturuncu, Bolivian Altiplano, in: Caricchi, L., Blundy, J.D. (Eds.), Chemical, Physical and Temporal Evolution of Magmatic Systems. Geol. Soc. London Spec. Publ., 422, 1-27. doi: 10.1144/SP422.1

Mulch, A., Uba, C.E., Strecker, M.R., Schoenberg, R., Chamberlain, C. P., 2010. Late Miocene climate variability and surface elevation in the central Andes. Earth Planet. Sci. Lett., 290 (1-2), 173-182

Müller, J.P., Kley, J., Jacobshagen, V., 2002. Structure and Cenozoic kinematics of the Eastern Cordillera, southern Bolivia (21°S). Tectonics, 21 (5), 1037. doi:10.1029/2001TC001340.

Muñoz, N., Charrier, R., 1996. Uplift of the western border of the Altiplano on a west-vergent thrust system, northern Chile. J. S. Am. Earth Sci., 9, 171–181.

Murray, K.E., Braun, J., Reiners, P.W., 2018. Toward robust interpretation of low-temperature thermochronometers in magmatic terranes. Geochem., Geophys., Geosyst., 19(10), 3739-3763.

[dataset] Mutschler, F.E., Ludington, S., Bookstrom, A. 2001. Giant porphyry-related metal camps of the world – a database. U.S. Geological Survey Open-file Report 99-556. https://pubs.usgs.gov/of/1999/of99-556/

Nalpas, T., Dabard, M.P., Ruffet, G., Vernon, A., Mpodozis, C., Loi, A., Hérail, G., 2008. Sedimentation and preservation of the Miocene Atacama Gravels in the Pedernales–Chañaral area, Northern Chile: climatic or tectonic control?. Tectonophysics, 459 (1-4), 161-173.

Naranjo, J.A., Villa, V., Ramírez, C., Pérez de Arce, C., 2018. Volcanism and tectonism in the southern Central Andes: Tempo, styles, and relationships. Geosphere, 14 (2), 626-641.

Nielsen, S.N., Glodny, J., 2009. Early Miocene subtropical water temperatures in the southeast Pacific. Palaeogeography, Palaeoclimatology, Palaeoecology, 280 (3-4), 480-488.

Nogués-Paegle, J., Mechoso, C. R., Fu, R., Berbery, E. H., Chao, W. C., Chen, T. C., Cook, K, and others (2002). Progress in Pan American CLIVAR research: understanding the South American monsoon. Meteorologica, 27(12), 1-30.

Nyström, J., O., Vergara, M., Morata, D., Levi, B., 2003. Tertiary volcanism during extension in the Andean foothills of central Chile (33°15’-33°45’). Geol. Am. Soc. Bull., 115 (12), 1523-1537.

Oerter, E., Amundson, R., Heimsath, A., Jungers, M., Chong, G., Renne, P., 2016. Early to Middle Miocene climate in the Atacama Desert of Northern Chile. Paleogeogr., Paleoclimatol., Paleoecol., 441, 890-900.

Oliveros, V., Morata, D., Aguirre, L., Féraud, G., Fornari, M., 2007. Jurassic to Early Cretaceous subduction–related magmatism in the Coastal Cordillera of northern Chile (18°30’–24°S): geochemistry and petrogenesis. Rev. Geol. Chile, 34, 209-232.

Oliveros, V., González, J., Vargas, M.E., Vásquez, P., Rossel, P., Creixell, C., Sepúlveda, F., Bastias, F., 2018. The early stages of the magmatic arc in the southern Central Andes, in: Folguera, A., Contreras-Reyes, E., Heredia, N., Encinas, A., Iannelli, S.B., Oliveros, V., Dávila, F.M., Collo, G., Giambiagi, L., Maksymowicz, A., Iglesia Llanos, M.P., Turienzo, M., Naipauer, M., Orts, D., Litvak, V.D., Alvarez, O., Arriagada, C. (Eds.), The Evolution of the Chilean-Argentinean Andes. Springer Earth System Sciences, Springer, Cham, Switzerland, pp. 165-190.

Oncken O., Hindle D., Kley J., Elger K., Victor P., Schemmann K., 2006. Deformation of the Central Andean Upper Plate System - Facts, Fiction, and Constraints for Plateau Models, in: Oncken O., Chong., G., Franz, G., Giese, P., Götze, H., Ramos, V.A., Strecker, M.R., Wigger, P. (Eds.), The Andes. Frontiers in Earth Sciences. Springer, Berlin, Heidelberg, pp. 3-27.

Oncken, O., Boutelier, D., Dresen, G., Schemmann, K., 2012. Strain accumulation controls failure of a plate boundary zone: Linking deformation of the Central Andes and lithosphere mechanics. Geochemistry Geophysics Geosystems, 13 (12), 1-22. doi: 10.1029/2012GC004280

Ortiz, G., Alvarado, P., Fosdick, J.C., Perucca, L., Sáez, M., Venerdini, A., 2015. Active deformation in the northern Sierra de Valle Fértil, Sierras Pampeanas, Argentina. J. S. Am. Earth Sci., 64, 339-350.

Pananont, P., Mpodozis, C., Blanco, N., Jordan, T. E., Brown, L. D., 2004. Cenozoic evolution of the northwestern Salar de Atacama Basin, northern Chile. Tectonics, 23, TC6007. doi: 10.1029/2003TC001595

Parrish J.T., Ziegler A.M., Scotese C.R., 1982. Rainfall patterns and the distribution of coals and evaporites in the Mesozoic and Cenozoic. Palaeogeogr., Palaeoclim., Palaeoecol., 40, 67-101.

Pearson, D.M., Kapp, P., DeCelles, P.G., Reiners, P.W., Gehrels, G.E., Ducea, M.N., Pullen, A., 2013. Influence of pre-Andean crustal structure on Cenozoic thrust belt kinematics and shortening magnitude: Northwestern Argentina. Geosphere, 9(6), 1766-1782. doi:10.1130/GES00923.1

Peel, M.C., Finlayson, B.L., McMahon, T.A., 2007. Updated world map of the Köppen-Geiger climate classification. Hydrol. Earth Syst. Sci., 11, 1633-1644. doi:10.5194/hess-11-1633-2007

Perkins, J.P., Ward, K.M., de Silva, S.L., Zandt, G., Beck, S.L., Finnegan, N.J., 2016. Surface uplift in the Central Andes driven by growth of the Altiplano Puna Magma Body. Nature Commun., 7 (13185). doi: 10.1038/ncomms13185

Plank, T., Langmuir, C.H., 1988. An evaluation of the global variations in the major element chemistry of arc basalts. Earth Planet. Sci. Lett., 90, 349–370. doi: 10.1016/0012-821X(88)90135-5.

Porras, H., Pinto, L., Tunik, M., Giambiagi, L., Deckart, K., 2016. Provenance of the Miocene Alto Tunuyán Basin (33 40’ S, Argentina) and its implications for the evolution of the Andean Range: Insights from petrography and U–Pb LA–ICPMS zircon ages. Tectonophysics, 690, 298-317.

Profeta, L., Ducea, M.N., Chapman, J.B., Paterson, S.R., Gonzales, S.M.H., Kirsch, M., Petrescu, L., DeCelles, P.G., 2015. Quantifying crustal thickness over time in magmatic arcs. Sci. Rep., 5 (17786). doi: 10.1038/srep17786

Rabassa, J., Coronato, A.M., Salemme, M., 2005. Chronology of the Late Cenozoic Patagonian glaciations and their correlation with biostratigraphic units of the Pampean region (Argentina). J. S. Am. Earth Sci., 20(1-2), 81-103.

Ramos, V.A., Folguera, A., 2005. Tectonic evolution of the Andes of Neuquén: Constraints derived from the magmatic arc and foreland deformation. Geol. Soc. London Spec. Publ., 252, 15–35.

Ramos, V. A., Folguera, A., 2009. Andean flat-slab subduction through time. Geol. Soc. London Spec. Publ., 327, 31–54. doi: 10.1144/SP327.3

Ramos, V.A., Cegarra, M., Cristallini, E., 1996. Cenozoic tectonics of the High Andes of wet-central Argentina (30-36°S latitude). Tectonophysics, 259, 185-200.

Raymo, M. E., Ruddiman, W. F., 1992. Tectonic Forcing of Late Cenozoic Climate. Nature, 359 (6391), 117-122.

Rech, J.A., Currie, B. S., Shullenberger, E.D., Dunagan, S.P., Jordan, T.E., Blanco, N., Tomlinson, A.J., Rowe, H.D., Houston, J., 2010. Evidence for the development of the Andean rain shadow from a Neogene isotopic record in the Atacama Desert, Chile. Earth Planet. Sci. Lett., 292 (3-4), 371-382.

Rech, J.A., Currie, B.S., Jordan, T.E., Riquelme, R., Lehmann, S.B., Kirk-Lawlor, N.E., Li, S., Gooley, J.T., 2019. Massive middle Miocene gypsic paleosols in the Atacama Desert and the formation of the Central Andean rain-shadow. Earth Planet. Sci. Lett., 506, 184-194.

Reiners, P.W., Ehlers, T.A., Mitchell, S.G., Montgomery, D.R., 2003. Coupled spatial variations in precipitation and long-term erosion rates across the Washington Cascades. Nature, 426 (6967), 645-647.

Reiners, P. W., Thomson, S., Vernon, A., Willett, S., Zattin, M., Einhorn, J., Gehrels, G., Quade, J., Pearson, D., Murray, K., 2015. Low-temperature thermochronologic trends across the central Andes, 21°S-28°S. Geol. Soc. Am. Mem., 212, 215-249.

Rehak, K., Bookhagen, B., Strecker, M.R., Echtler, H.P., 2010. The topographic imprint of a transient climate episode: the western Andean flank between 15·5° and 41·5°S. Earth Surf. Process. Landf., 35 (13), 1516-1534.

Riesner, M., Lacassin, R., Simoes, M., Armijo, R., Rauld, R., Vargas, G., 2017. Kinematics of the active West Andean fold-and-thrust belt (central Chile): Structure and long-term shortening rate. Tectonics, 36, 287–303. doi: 10.1002/2016TC004269.

Riesner, M., Lacassin, R., Simoes, M., Carrizo, D., Armijo, R., 2018. Revisiting the Crustal Structure and Kinematics of the Central Andes at 33.5°S: Implications for the Mechanics of Andean Mountain Building. Tectonics, 37, 1347–1375. doi:10.1002/2017TC004513

Riesner M., Simoes, M., Carrizo, D., Lacassin, R., 2019. Early exhumation of the Frontal Cordillera (Southern Central Andes) and implications for Andean mountain-building at ~33.5°S. Sci. Rep., 9(7972). doi: 10.1038/s41598-019-44320-1

Riquelme, R., Hérail, G., Martinod, J., Charrier, R., Darrozes, J., 2007. Late Cenozoic geomorphologic signal of Andean forearc deformation and tilting associated with the uplift and climate changes of the Southern Atacama Desert (26°S–28°S). Geomorphology, 86 (3-4), 283-306.

Rodríguez, M.P., Charrier, R., Brichau, S., Carretier, S., Farías, M., de Parseval, P., Ketcham, R.A., 2018. Latitudinal and longitudinal patterns of exhumation in the Andes of north-central Chile. Tectonics, 37, 2863–2886. doi: 10.1029/2018TC004997

Rohrmann, A., Sachse, D., Mulch, A., Pingel, H., Tofelde, S., Alonso, R.N., Strecker, M.R., 2016. Miocene orographic uplift forces rapid hydrological change in the southern central Andes. Sci. Rep., 6 (35678).

Rojas Vera, E. A., Folguera, A., Zamora Valcarce, G., Giménez, M., Ruiz, F., Martínez, P., Bottesi, G., Ramos, V. A., 2010. Neogene to Quaternary extensional reactivation of a fold and thrust belt: The Agrio belt in the southern central Andes and its relation to the Loncopúe trough (38°–39°S). Tectonophysics, 492, 279–294.

Rossel, K., Aguilar, G., Salazar, E., Martinod, J., Carretier, S., Pinto, L., Cabré, A., 2016. Chronology of Chilean Frontal Cordillera building from geochronological, stratigraphic and geomorphological data insights from Miocene intramontane-basin deposits. Basin Res., 30, 289-310.

Royden, L.H., 1993. Evolution of retreating subduction boundaries formed during continental collision. Tectonics, 12 (2), 629-638.

Ruddiman, W. F., 2008. Earth's Climate: past and future. Freeman and Company, 2nd edition, New York.

Ruskin, B.G., Jordan, T.E., 2007. Climate change across continental sequence boundaries: paleopedology and lithofacies of Iglesia Basin, northwestern Argentina. Jour. Sed. Res., 77(9), 661-679.

Ryan, J., Beck, S., Zandt, G., Wagner, L., Minaya, E., Tavera, H., 2016. Central Andean crustal structure from receiver function analysis. Tectonophysics, 682, 120-133.

Sáez, A., Cabrera, L., Garcés, M., van den Bogaard, P., Jensen, A., Gimeno, D., 2012. The stratigraphic record of changing hyperaridity in the Atacama Desert over the last 10 Ma. Earth Planet. Sci. Lett., 355, 32-38.

Safipour, R., Carrapa, B., DeCelles, P.G., Thomson, S.N., 2015. Exhumation of the Precordillera and northern Sierras Pampeanas and along-strike correlation of the Andean orogenic front, northwestern Argentina. Geol. Soc. Am. Mem., 212, 181-199.

Saulo., A.C., Nicolini, M., Chou, S.C., 2000. Model characterization of the South Americam low-level flow during the 1997-1998 spring-summer season. Clim. Dyn., 16, 867-881.

Saylor, J.E., Horton, B.K., 2014. Nonuniform surface uplift of the Andean plateau revealed by deuterium isotopes in Miocene volcanic glass from southern Peru. Earth Planet. Sci. Lett., 387, 120-131.

Schepers, G., Van Hinsbergen, D. J., Spakman, W., Kosters, M. E., Boschman, L. M., McQuarrie, N., 2017. South-American plate advance and forced Andean trench retreat as drivers for transient flat subduction episodes. Nature commun., 8 (15249).

[dataset] Scheuber, E., 1998. Radiometric and Fission Track Age Determination of Central Andes. Freie Universität Berlin. www.cms.fu-berlin.de/sfb/sfb267/results/data_catalogue/central_andean_data/geochemical_data.html

Scheuber E., Bogdanic T., Jensen A., Reutter, K.J., 1994. Tectonic development of the North Chilean Andes in relation to plate convergence and magmatism since the Jurassic, in: Reutter, K.J., Scheuber E., Wigger, P.J. (Eds.), Tectonics of the Southern Central Andes. Springer, Berlin, Heidelberg, pp. 121-139.

Schildgen, T.F., van der Beek, P.A., Sinclair, H.D., Thiede, R.C., 2018. Spatial correlation bias in late-Cenozoic erosion histories derived from thermochronology. Nature, 559 (7712), 89-93.

Schwerdtfeger, W., 1976. Climates of Central and South America. Elsevier, New York.

Scott, E. M., Allen, M. B., Macpherson, C. G., McCaffrey, K. J., Davidson, J. P., Saville, C., Ducea, M. N., 2018. Andean surface uplift constrained by radiogenic isotopes of arc lavas. Nature commun., 9 (1), 969.

Sempere, T., Butler, R.F., Richards, D.R., Marshall, L.G., Sharp, W., Swisher, C.C., 1997. Stratigraphy and chronology of late Cretaceous–early Paleogene strata in Bolivia and northern Argentina. Geol. Soc. Amer. Bull., 109, 709– 727.

SegemAR, 1997. Mapa geológico de la República Argentina: versión digital; escala 1:2'500'000. Serv. Geol. Min. Argentino, Buenos Aires, Argentina.

SERNAGEOMIN, 2003. Mapa Geológico de Chile: versión digital. Base Geológica escala 1:1'000'000. Serv. Nac. Geol. Min. Publ. Geol., Digital, 4, Santiago, Chile.

Shackleton, N.J., Backman, J., Zimmerman, H.T., Kent, D.V., Hall, M.A., Roberts, D.G., Schnitker, D., Baldauf, J.G., Desprairies, A., Homrighausen, R. …, Westberg-Smith, J., 1984. Oxygen isotope calibration of the onset of ice-rafting and history of glaciation in the North Atlantic region. Nature, 307 (5952), 620-623.

Shuster, D.L., Ehlers, T.A., Rusmoren, M.E., Farley, K.A., 2005. Rapid glacial erosion at 1.8 Ma revealed by 4He/3He thermochronometry. Science, 310 (5754), 1668-1670.

Shuster, D.L., Cuffey, K.M., Sanders, J.W., Balco, G., 2011. Thermochronometry reveals headward propagation of erosion in an alpine landscape. Science, 332 (6025), 84-88.

[dataset] Singer, D.A., Berger, V.I., Moring, B.C., 2008. Porphyry Copper Dpeosits of the World: Data base and Grade and Tonnage Models. U.S. Geological Survey Open-file Report 2008-1155. https://pubs.usgs.gov/of/2008/1155/

Siravo, G., Faccenna, C., Gérault, M., Becker, T.W., Fellin, M.G., Herman, F., Molin, P., 2019. Slab flattening and the rise of the Eastern Cordillera, Colombia. Earth Planet. Sci. Lett., 512, 100-110.

Sobel., E.R., Strecker, M.R., 2003. Uplift, exhumation and precipitation: tectonic and climatic control of Late Cenozoic landscape evolution in the northern Sierra Pampeanas, Argentina. Basin Res., 15, 431-41. doi: 10.1046/j.1365-2117.2003.00214.x

Spikings, R., Dungan, M., Foeken, J., Carter, A., Page, L., Stuart, F., 2008. Tectonic response of the central Chilean margin (35-38°S) to the collision and subduction of heterogeneous oceanic crust: a thermochronological study. J. Geol. Soc., 165 (5), 941-953.

Springer, M., Förster, A., 1998. Heat-flow density across the Central Andean subduction zone. Tectonophysics, 291, 123-139.

Starck, D., Anzótegui, L.M., 2001. The late Miocene climatic change—Persistence of a climatic signal through the orogenic stratigraphic record in northwestern Argentina. J. S. Am. Earth Sci., 14(7), 763-774.

Strecker, M.R., Cerveny, P., Bloom, A.L., Malizia, D., 1989. Late Cenozoic Tectonism and Landscape Development in the Foreland of the Andes: Northern Sierras Pampeanas (26°-28°S), Argentina. Tectonics, 8(3), 517-534.

Strecker, M.R., Alonso, R.N., Bookhagen, B., Carrapa, B., Hilley, G. E., Sobel, E.R., Trauth, M.H., 2007. Tectonics and climate of the southern central Andes. Ann. Rev. Earth Planet. Sci., 35, 747-787.

Strecker, M., Alonso, R., Bookhagen, B., Carrapa, B., Coutand, I., Hain, M., Hilley, G., Mortimer, E., Schoenbohm, L., Sobel, E., 2009. Does the topographic distribution of the central Andean Puna Plateau result from climatic or geodynamic processes?. Geology, 37 (7), 643-646.

Stuut, J.W., Lamy, F., 2004. Climate variability at the southern boundaries of the Namib (southwestern Africa) and Atacama (northern Chile) coastal deserts during the last 120,000 yr. Quat. Res., 62, 301-309. doi:10.1016/j.yqres.2004.08.001

Tarantola, A., 2005. Inverse Problem Theory and Methods for Model Parameter Estimation, siam, Philadelphia, USA, 1-342.

Thomson, S. N., Brandon, M. T., Tomkin, J. H., Reiners, P. W., Vásquez, C., Wilson, N. J., 2010. Glaciation as a destructive and constructive control on mountain building. Nature, 467 (7313), 313-317.

Tripaldi, A., Limarino, C.O., 2005. Vallecito Formation (Miocene): The evolution of an eolian system in an Andean foreland basin (northwestern Argentina). Jour. South Am. Earth Sci., 19 (3), 343-357.

Uba, C.E., Heubeck, C., Hulka, C., 2005. Facies analysis and basin architecture of the Neogene Subandean synorogenic wedge, southern Bolivia. Sediment. Geol., 180, 91-123, doi:10.1016/j.sedgeo.2005.06.013

Uba, C. E., Heubeck, C., Hulka, C., 2006. Evolution of the late Cenozoic Chaco foreland basin, Southern Bolivia. Basin Res., 18, 145–170, doi: 10.1111/j.1365-2117.2006.00291.x

Uba, C.E., Strecker, M.R., Schmitt, A.K., 2007. Increased sediment accumulation rates and climatic forcing in the central Andes during the late Miocene. Geology, 35 (11), 979-982. doi: 10.1130/G224025A.1.

Uba, C. E., Kley, J., Strecker, M. R., Schmitt, A. K., 2009. Unsteady evolution of the Bolivian Subandean thrust belt: The role of enhanced erosion and clastic wedge progradation. Earth Planet. Sci. Lett., 281(3-4), 134-146.

Valero-Garcés, B.L., Jenny, B., Rondanelli, M., Delgado-Huertas, A., Burns, S.J., Veit, H., Moreno, A., 2005. Palaeohydrology of Laguna de Tagua Tagua (34° 30′ S) and moisture fluctuations in Central Chile for the last 46 000 yr. J. Quat. Sci., 20 (7-8), 625-641.

Vandergoes, M.J., Newnham, R.M., Preusser, F., Hendy, C.H., Lowell, T.V., Fitzsimons, S.J., Hogg, A.G., Kasper, H.U., Schlüchter, C., 2005. Regional insolation forcing of late Quaternary climate change in the Southern Hemisphere. Nature, 436(7048), 242-245. doi:10.1038/nature03826

van der Meijde, M., Julià, J., Assumpção, M., 2013. Gravity derived Moho for South America. Tectonophysics, 609, 456-467. doi: 10.1016/j.tecto.2013.03.023

Vargas, G., Klinger, Y., Rockwell, T.K., Forman, S.L., Rebolledo, S., Baize, S., Lacassin, R., Armijo, R., 2014. Probing large intraplate earthquakes at the west flank of the Andes. Geology, 42(12), 1083-1086. doi:10.1130/G35741.1

Vera C., Higgins, W., Amdor, J., Ambrizzi, T., Garreaud, R., Gochis, D., Gutzler, D., Lettenmaier, D., Marengo, J., Mechoso, C.R., Nogues-Paegle, J., Silva Dias, P.L., Zhang, C., 2006. Toward a unified view of the American Monsoon System. Am. Meteorolog. Soc., 19, 4977-5000.

Vermeesch, P., 2009. RadialPlotter: A Java application for fission track, luminescence and other radial plots, Radiat. Meas., 44(4), 409-410.

Victor, P., Oncken, O., Glodny, J., 2004. Uplift of the western Altiplano plateau: Evidence form the Precordillera between 20° and 21°S (northern Chile). Tectonics, 23, TC4004, 1-24. doi:10.1029/2003TC001519

Villagrán, C., Armesto, J.J., Hinojosa, F., Cuvertino, J., Pérez, C., Medina, C., 2004. El enigmático orígen del bosque relicto de Fray Jorge, in: Squeo, F.A., Gutiérrez, J.R., Hernández, I.R. (Eds.), Historia Natural del Parque Nacional Bosque Fray Jorge. Ediciones Universidad de La Serena, La Serena, Chile, pp. 3–43.

Vuille, M., Ammann, C., 1997. Regional snowfall patterns in the high, arid Andes. Clim. Change, 36, 413-423. doi:10.1023/A:1005330802974

Wagner, G.A., Miller, D.S., Jäger, E., 1979. Fission track ages on apatite of Bergell rocks from central Alps and Bergell boulders in Oligocene sediments. Earth Planet. Sci. Lett., 45(2), 355-360.

Ward, K. M., Zandt, G., Beck, S.L., Christensen, D. H., McFarlin, H., 2014. Seismic imaging of the magmatic underpinnings beneath the Altiplano-Puna volcanic complex from the joint inversion of surface wave dispersion and receiver functions. Earth Planet. Sci. Lett., 404, 43-53.

Weatherall, P., Marks, K.M., Jakobsson, M., Schmitt, T., Tani, S., Arndt, J.E., Rovere, M., Chayes, D., Ferrini, V., Wigley, R., 2015. A new digital bathymetric model of the world's oceans. Earth Space Sci., 2 (8), 331-345.

Whipple, K. X., 2009. The influence of climate on the tectonic evolution of mountain belts. Nat. Geosci., 2 (2), 97-104.

Whipple, K. X., 2014. Can erosion drive tectonics?. Science, 346 (6212), 918-919.

Whipple, K.X., Meade, B.J., 2006. Orogen response to changes in climatic and tectonic forcing. Earth Planet. Sci. Lett., 243, 218-228.

Willenbring, J. K., Jerolmack, D. J., 2016. The null hypothesis: globally steady rates of erosion, weathering fluxes and shelf sediment accumulation during Late Cenozoic mountain uplift and glaciation. Terra Nova, 28 (1), 11-18.

Willett, S.D., 1999. Orogeny and orography: The effects of erosion on the structure of mountain belts. J. Geophys. Res. Solid Earth, 104 (B12), 28957-28981.

Willett, S.D, Beaumont, C., Fullsack, P., 1993. Mechanical model for the tectonics of doubly vergent compressional orogens. Geology, 21 (4), 371-374.

Willett, S.D., Herman, F., Fox, M., Stalder, N.F., Yang, R., Ehlers, T.E., subm. Bias and error in modelling thermochronometric data: resolving a potential increase in Plio-Pleistocene erosion rate. Earth Surf. Dyn. Discussions

Winocur, D. A., Litvak, V. D., Ramos, V. A., 2015. Magmatic and tectonic evolution of the Oligocene Valle del Cura Basin, main Andes of Argentina and Chile: Evidence for generalized extension. Geol. Soc. London. Spec. Pub., 399, 109-130. doi: 10.1144/SP399.2

Wotzlaw, J. F., Decou, A., von Eynatten, H., Wörner, G., Frei, D., 2011. Jurassic to Palaeogene tectono-magmatic evolution of northern Chile and adjacent Bolivia from detrital zircon U-Pb geochronology and heavy mineral provenance. Terra Nova, 23 (6), 399-406.

York, D., Evensen, N.M., López Martínez, M., De Basabe Delgado, J., 2004. Unified equations for the slope, intercept, and standard error of the best straight line. Am. J. Phys., 72, 367. doi: 10.1119/1.1632486

Zachos, J., Pagani, M., Sloan, L., Thomas, E., Billups, K., 2001. Trends, Rhythms, and Aberrations in Global Climate 65 Ma to present. Science, 292(5517), 686-693.

Zapata, S., 2019. Paleozoic to Pliocene evolution of the Andean retroarc between 26 and 28°S: Interactions between tectonics, climate, and upper plate architecture. PhD Thesis, Universität Potsdam, Germany, pp. 139.

Zapata, S., Sobel, E.R., del Papa, C., Muruaga, C. Zhou, R., 2019. Miocene fragmentation of the Central Andean foreland basins between 26 and 28° S. Jour. South Am. Earth Sci., 94, 1-18

Zech, R., May, J.-H., Kull, C., Ilgner, J., Kubik, P. W., Veit, H., 2008. Timing of the late Quaternary glaciation in the Andes from ∼15 to 40°S. J. Quat. Sci.., 23, 635-647. doi: 10.1002/jqs.1200

Zech, R., Zech, J., Kull, C., Kubik, P.W., Veit, H., 2011. Early last glacial maximum in the southern Central Andes reveals northward shift of westerlies at ~39 ka. Clim. Past, 7, 41-46.

Zhang, P. Z., Molnar, P., Downs, W. R., 2001. Increased sedimentation rates and grain sizes 2-4 Myr ago due to the influence of climate change on erosion rates. Nature, 410 (6831), 891-897.

Zhou, J., Lau, K.-M., 1999. Does a Monsoon Climate Exist over South America?. Jour. Clim., 11, 1020-1040.

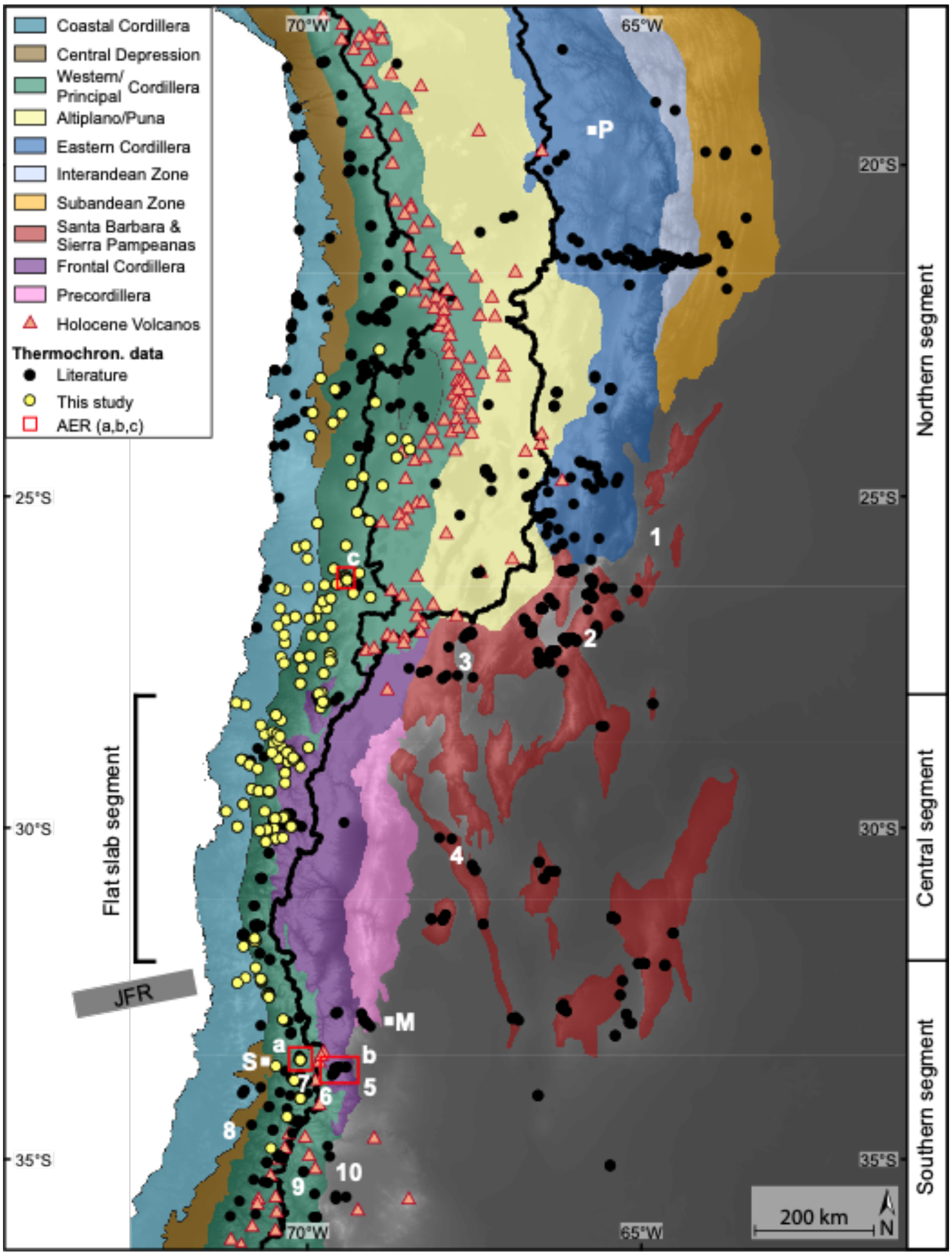

Fig. 1: Tectonomorphic units of the Central Andes modified from Müller et al. (2002), Mpodozis et al. (2005), Hilley and Coutand (2010), Carrapa et al. (2014), Armijo et al. (2015) and Riesner et al. (2018) and based on geological maps from SegemAR (1997) and SERNAGEOMIN (2003). JFR = Juan Fernandez ridge; AER = locations of age-elevation relationships shown in Fig. 14 (AER-a,b) and in supplementary Fig. S3 (AER-c). Numbers represent specific locations referred to in the text: 1 = Santa Barbara system; 2 = Sierra Aconquíja; 3 = Fiambalá Basin; 4 = Sierra de Valle Fértil; 5 = Cuyo foreland basin; 6 = Aconcagua fold-and-thrust belt; 7 = West Andean fold-and-thrust belt; 8 = Laguna de Tagua Tagua; 9 = Malargüe fold-and-thrust belt; 10 = Malargüe foreland basin. S = Santiago de Chile

(CL); M = Mendoza (AR); P = Potosi (BO). Underlying topography from GMTED2010, 7.5 arc-s (Danielson and Gesch, 2011).

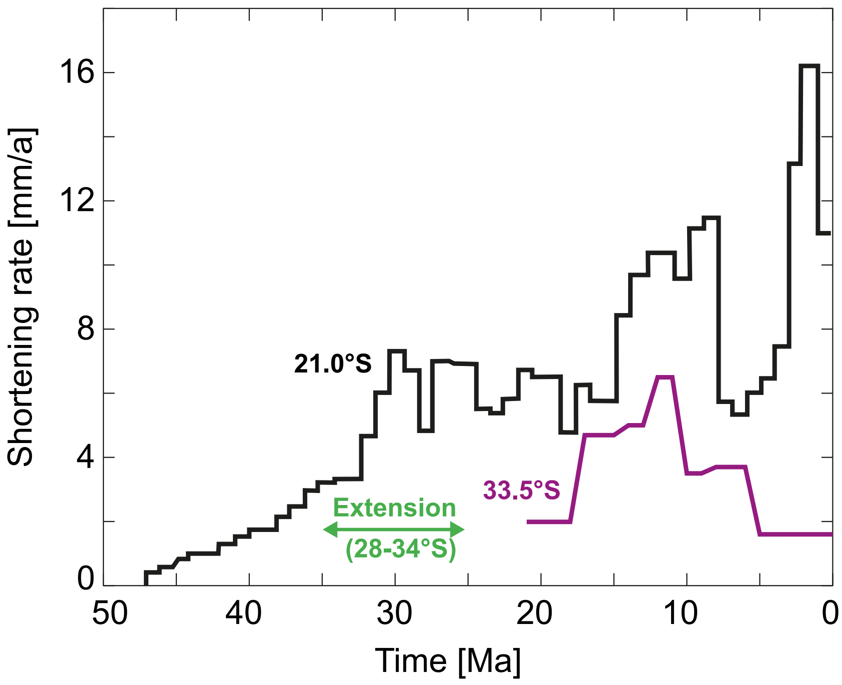

Fig. 2: Average orogenic shortening rates for the northern segment at 21°S (black line; Oncken et al., 2012) and southern segment at 33.5°S (purple line; Giambiagi et al., 2015a) of the study area. Green arrow indicates the period of Oligocene extension in the central and southern segments (see text for discussion). Please note that these shortening rate reconstructions mainly rely on studies from the eastern part of the Andes whereas shortening on the western side and in the Altiplano is largely unresolved.

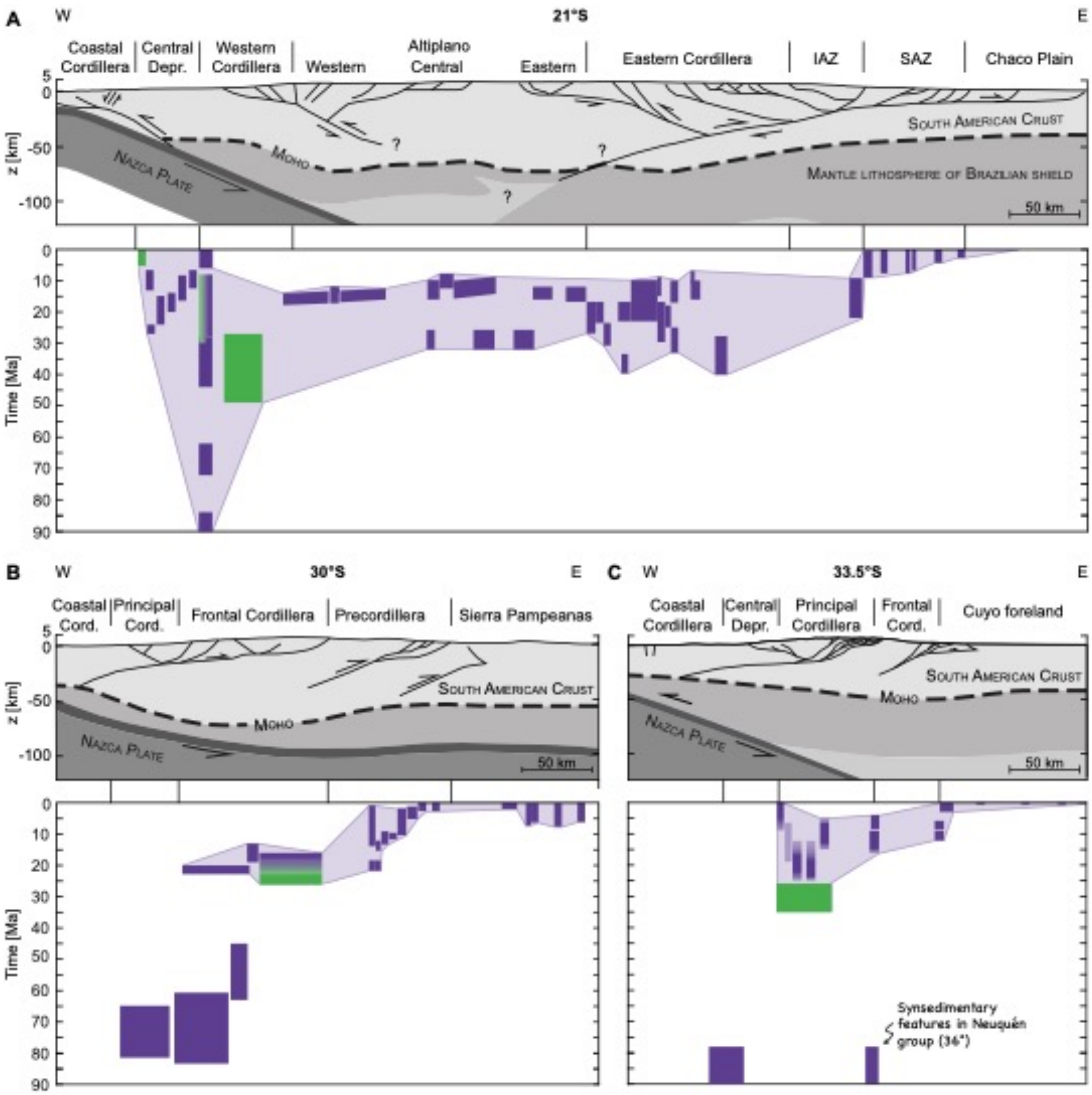

Fig. 3: Lithospheric-scale cross-sections and approximate onset and duration of deformation in the Central Andes as observed in syntectonic sediments. Dark purple boxes represent compression, green boxes extension. Light purple envelope outlines the inferred timespan of compression, i.e. delimiting the onset and cessation of tectonic activity in the respective tectonic units. See supplementary Table S6 for data compilation and references. Mean elevation from SWATH profiles over the respective areas. **A)** The northern segment comprises data between 19° and 24°S that was projected on a cross-section at 21°S within the respective tectonic units. Geological cross-section and crustal thickness modified from Armijo et al. (2015). Question marks indicate high uncertainty. IAZ = Interandean zone; SAZ = Subandean zone. **B)** The middle segment shows data between 28° and 31°S projected on a cross-section at 30°S within the respective tectonic units. Geological cross-section and crustal thickness

modified from Lossada et al. (2017) and Gans et al. (2011), respectively. **C)** Data for the southern segment include studies between 32.5° and 34°S projected on a cross-section at 33.5°S within the respective tectonic units. Geological cross-section and crustal thickness modified from Giambiagi et al. (2015a) and Gans et al. (2011), respectively.

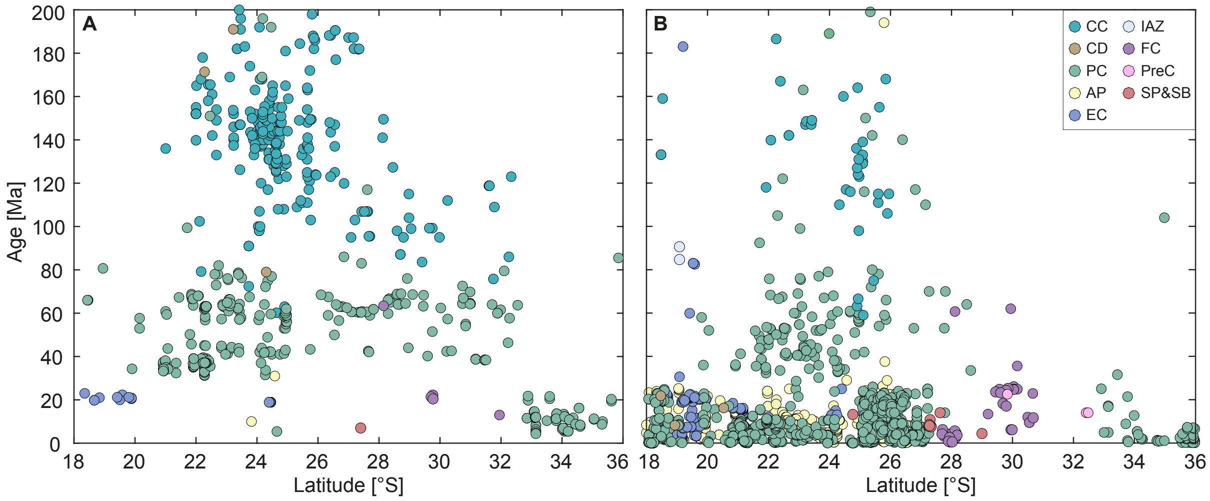

Fig 4: A) Magmatic and **B**) volcanic activity during the last 200 Ma along the strike of the Andes. Colors represent tectonomorphic units shown in Fig. 1: AP = Altiplano-Puna plateau; CC = Coastal Cordillera; CD = Central Depression; EC = Eastern Cordillera; FC = Frontal Cordillera; IAZ = Interandean zone; PC = Western/Principal Cordillera; PreC = Precordillera; SP = Sierra Pampeanas and Santa Barbara ranges. Data compilation from Mamani et al. (2010b) with additional data from McNutt et al. (1975), Kurtz et al. (1997), Scheuber (1998), Mutschler et al. (2001), Farías et al. (2008), Singer et al. (2008), Hervé et al. (2014), Jones et al. (2015), Muir et al. (2015) and Naranjo et al. (2018). Data are provided in supplementary Table S7.

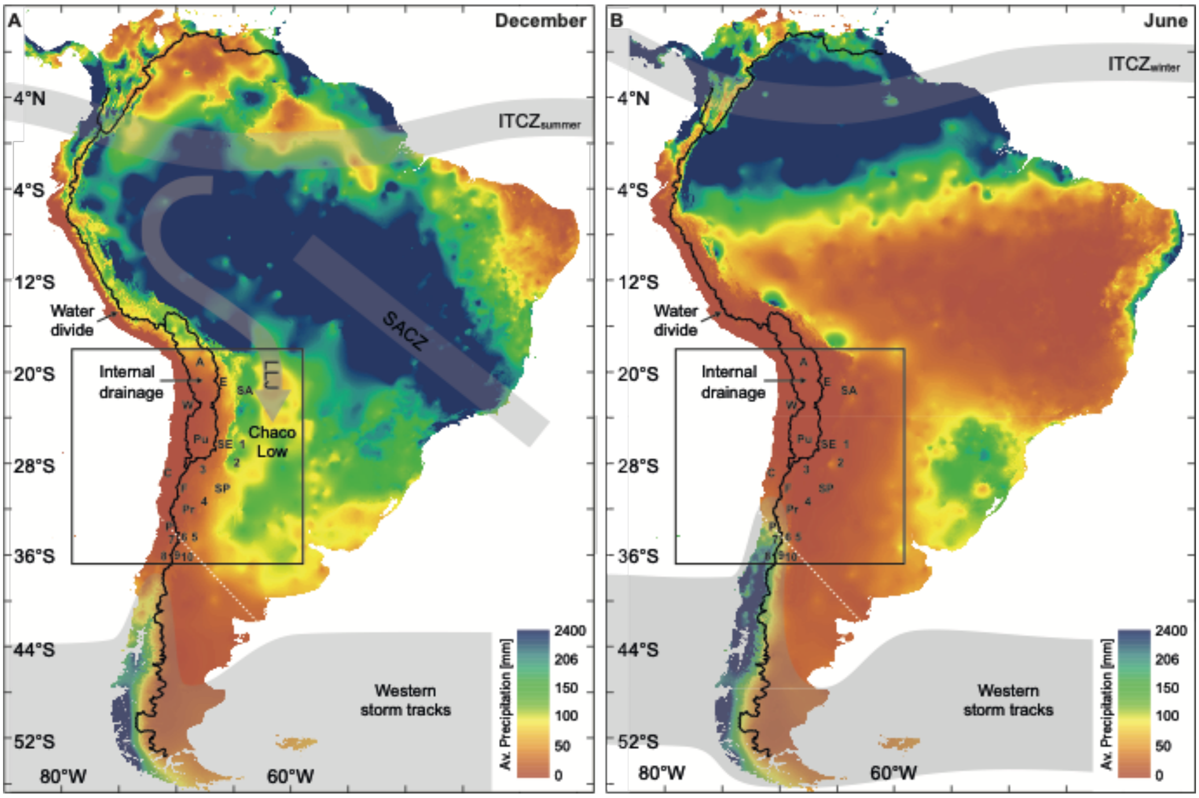

Fig. 5: Precipitation pattern of South America averaged over 1960-1990, with 2.5 arc-minutes resolution (from worldclim.org; Hijmans et al. (2005)). Black line represents the main drainage divide (Lehner and Grill, 2013), white stippled line the Arid Diagonal. Grey arrows indicate positions of main climatic features (after Norgués-Pagele et al., 2002, Vera et al., 2006; Garreaud, 2009): ITCZ = Intertropical Convergence Zone; SACZ = South Atlantic Convergence Zone; LLJ = low-level jet. 1 = Santa Barbara system; 2 = Sierra Aconquíja; 3 = Fiambalá Basin; 4 = Sierra de Valle Fértil; 5 = Cuyo foreland basin; 6 = Aconcagua fold-and-thrust belt; 7 = West Andean fold-and-thrust belt; 8 = Laguna de Tagua Tagua; 9 = Malargüe fold-and-thrust belt; 10 = Malargüe foreland basin. Letters correspond to tectonomorphic units: A = Altiplano; C = Coastal Cordillera; E = Eastern Cordillera; F = Frontal Cordillera; P = Principal Cordillera; Pr = Precordillera; Pu = Puna; SA = Subandean zone; SE = southern Eastern Cordillera; SP = Sierra Pampeanas; W = Western Cordillera. **A)** During austral summer, the LLJ brings moisture from the Atlantic to the eastern flank of the Andes. The SACZ is an additional source of moisture. The influence of the western storm tracks is restricted to areas south of ~38°S. **B)** In austral winter, almost no precipitation reaches the eastern flank and plateau, whereas the area affected by westerly precipitation expands up to about 30°S.

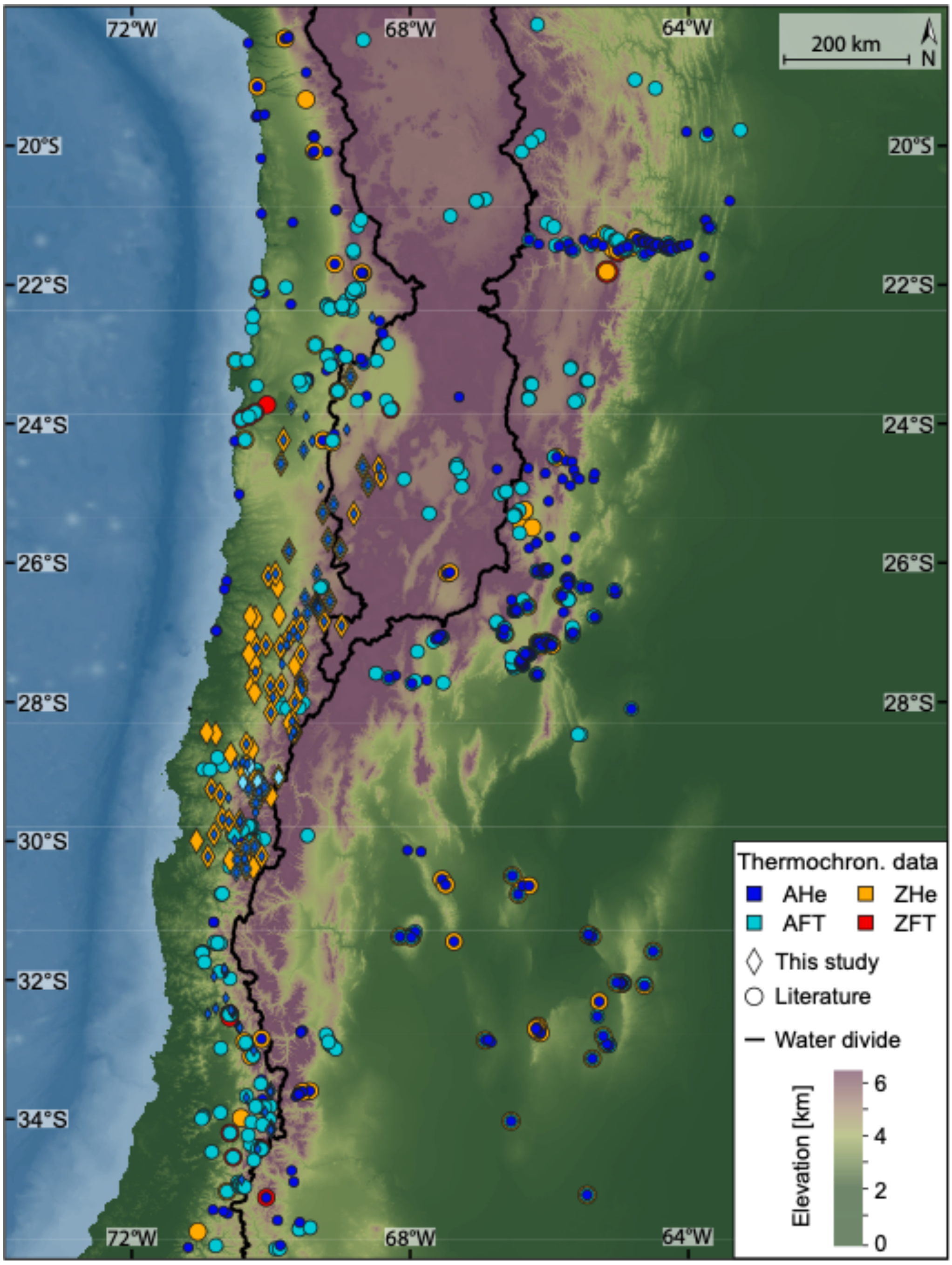

Fig. 6: Low-temperature thermochronological ages compiled from literature and own data (see supplementary Table S5 for data and references). Topography from GMTED2010, 7.5 arc-s (Danielson and Gesch, 2011), bathymetry from GEBCO_2014 (Weatherall et al., 2015).

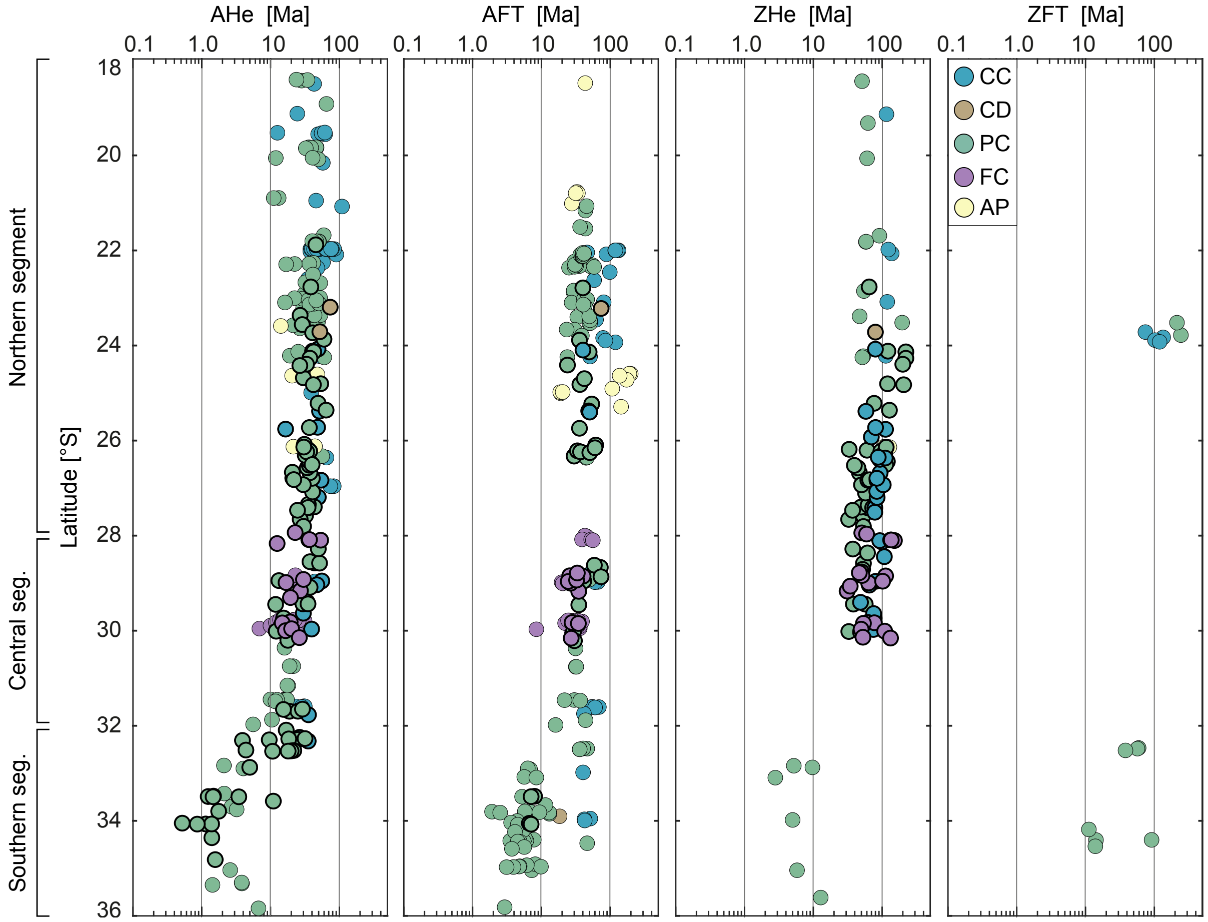

Fig. 7: Thermochronological ages west of the drainage divide along the strike of the Andes, including the internally drained Altiplano-Puna plateau. Colors represent tectonomorphic units from Fig. 1: AP = Altiplano-Puna plateau; CC = Coastal Cordillera; CD = Central Depression; FC = Frontal Cordillera; PC = Western/Principal Cordillera. Data from this study are highlighted with bold black rim. Ages south of 32°S are significantly younger than in the north for all thermochronologic systems. R denotes the exceptionally young sample from Rodríguez et al. (2018).

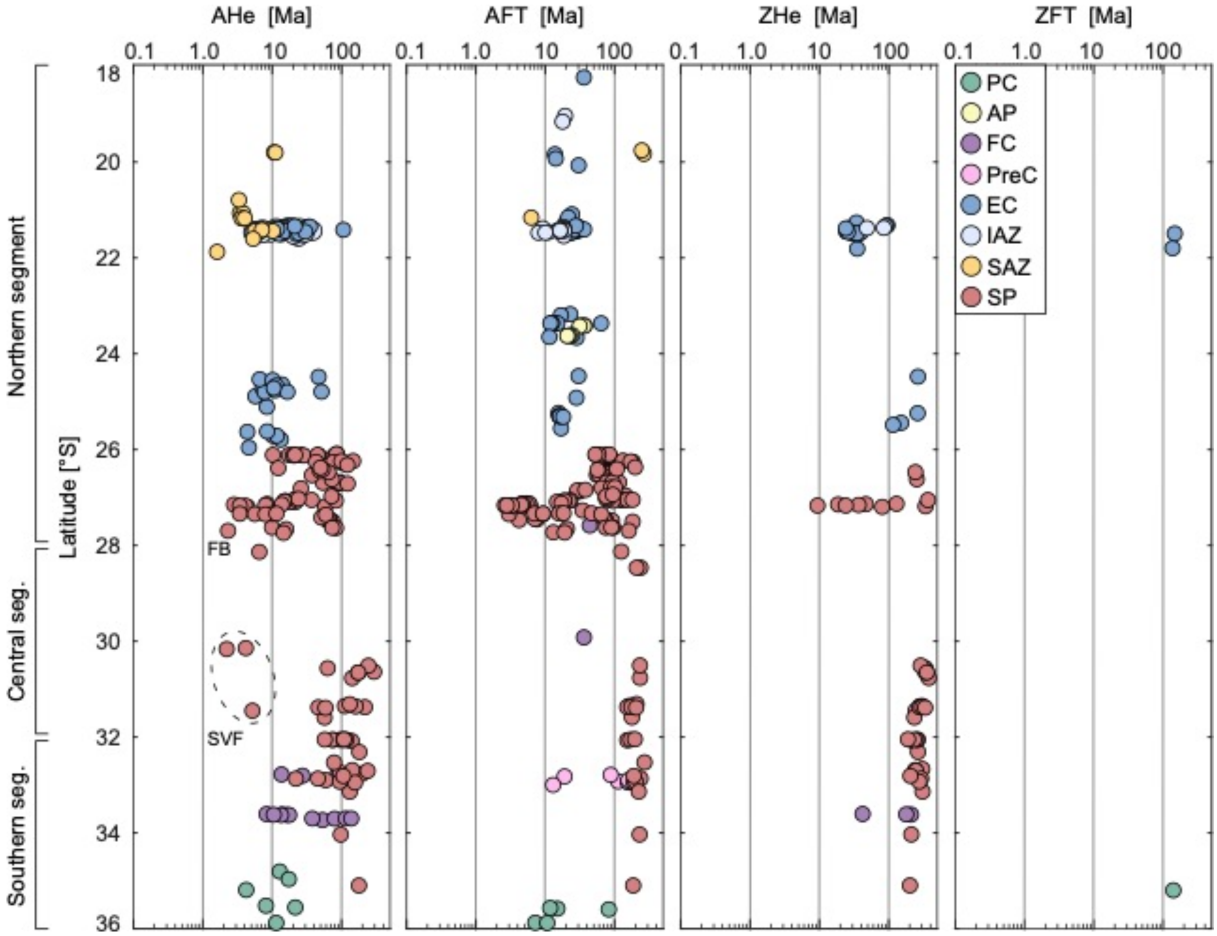

Fig. 8: Thermochronological ages east of the drainage divide along the strike of the Andes. Colors represent tectonomorphic units from Fig. 1: AP = Altiplano-Puna plateau; EC = Eastern Cordillera; FC = Frontal Cordillera; IAZ = Interandean zone; PC = Western/Principal Cordillera; PreC = Precordillera; SAZ = Subandean zone; SP = Sierra Pampeanas and Santa Barbara ranges. AHe, AFT and ZHe systems all show a youngest age cluster between 26° and 28°S but no clear pattern is observed. The AHe data additionally show young ages in the Subandean zone (21-22°S) and in the Sierra de Valle Fértil (SVF; Ortiz et al., 2015). FB denotes the young sample from the Fiambalá Basin (Safipour et al., 2015).

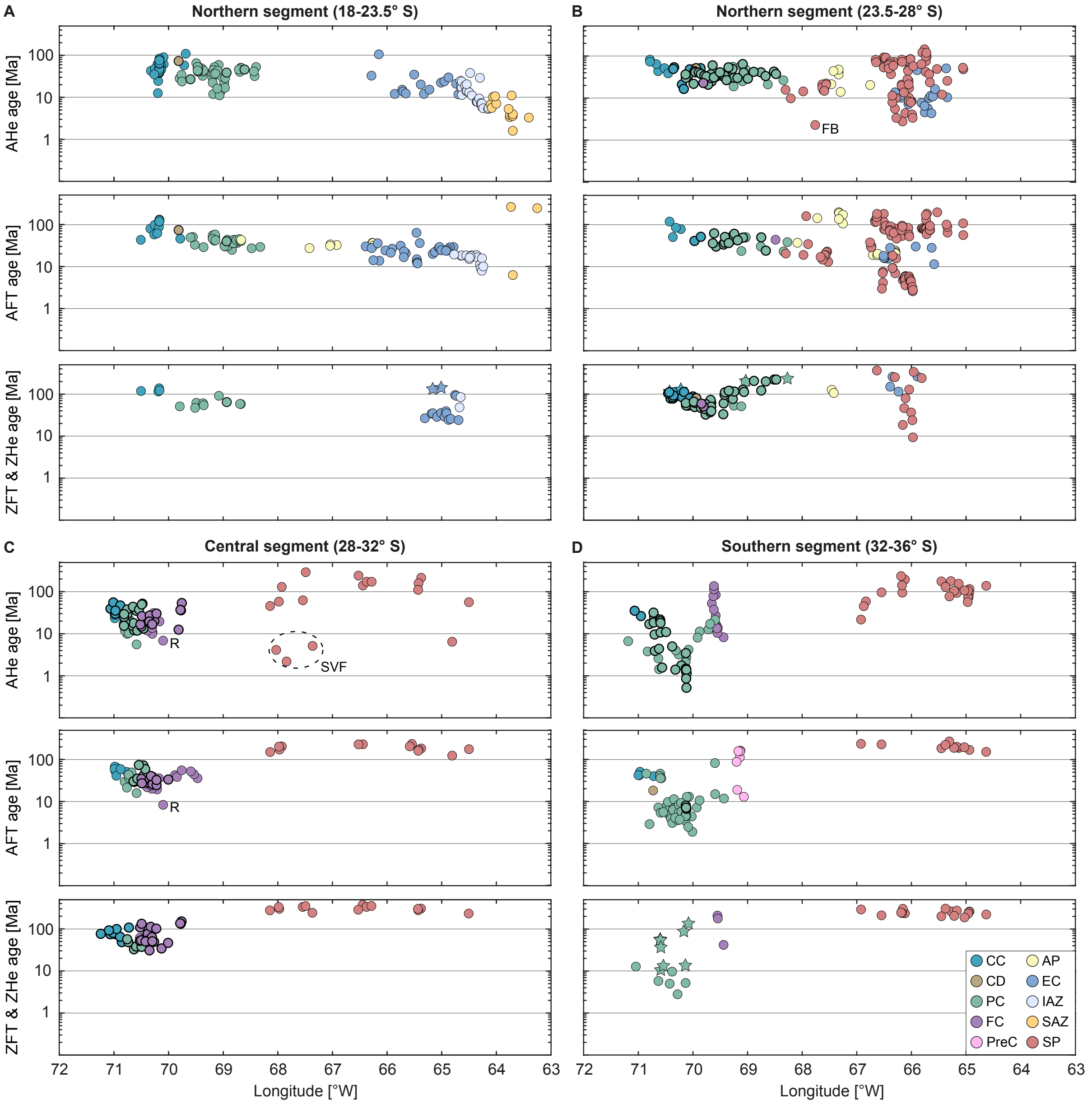

Fig. 9: Latitudinal cross-sections of thermochronological ages. ZFT ages in B&D are shown together with ZHe ages and represented by star symbols. Colors correspond to tectonic units from Fig. 1: AP = Altiplano-Puna plateau; CC = Coastal Cordillera; CD = Central Depression; EC = Eastern Cordillera; FC = Frontal Cordillera; IAZ = Interandean zone; PC = Western/Principal Cordillera; PreC = Precordillera; SAZ = Subandean zone; SP = Sierra Pampeanas and Santa Barbara ranges. **A, B**) The northern segment shows cooling ages that are younger than 10 Ma east of ca. 65°W in the Inter- and Subandean zones (A) and east of ca. 66.5°W in the northern Sierra Pampeanas and southern Eastern Cordillera (B). Ages to the west are all older than 10 Ma, with the exception of the young AHe age from the Fiambalá Basin (FB; Safipour et al., 2015). The central (C) and southern (D) segments show the opposite age trend with ages younging to the west, apart from four AHe ages from the Sierra de Valle Fértil (SVF; Ortiz et

al., 2015) and in the foreland (Zapata, 2019) in the central segment. Data from this study are highlighted with bold black rim.

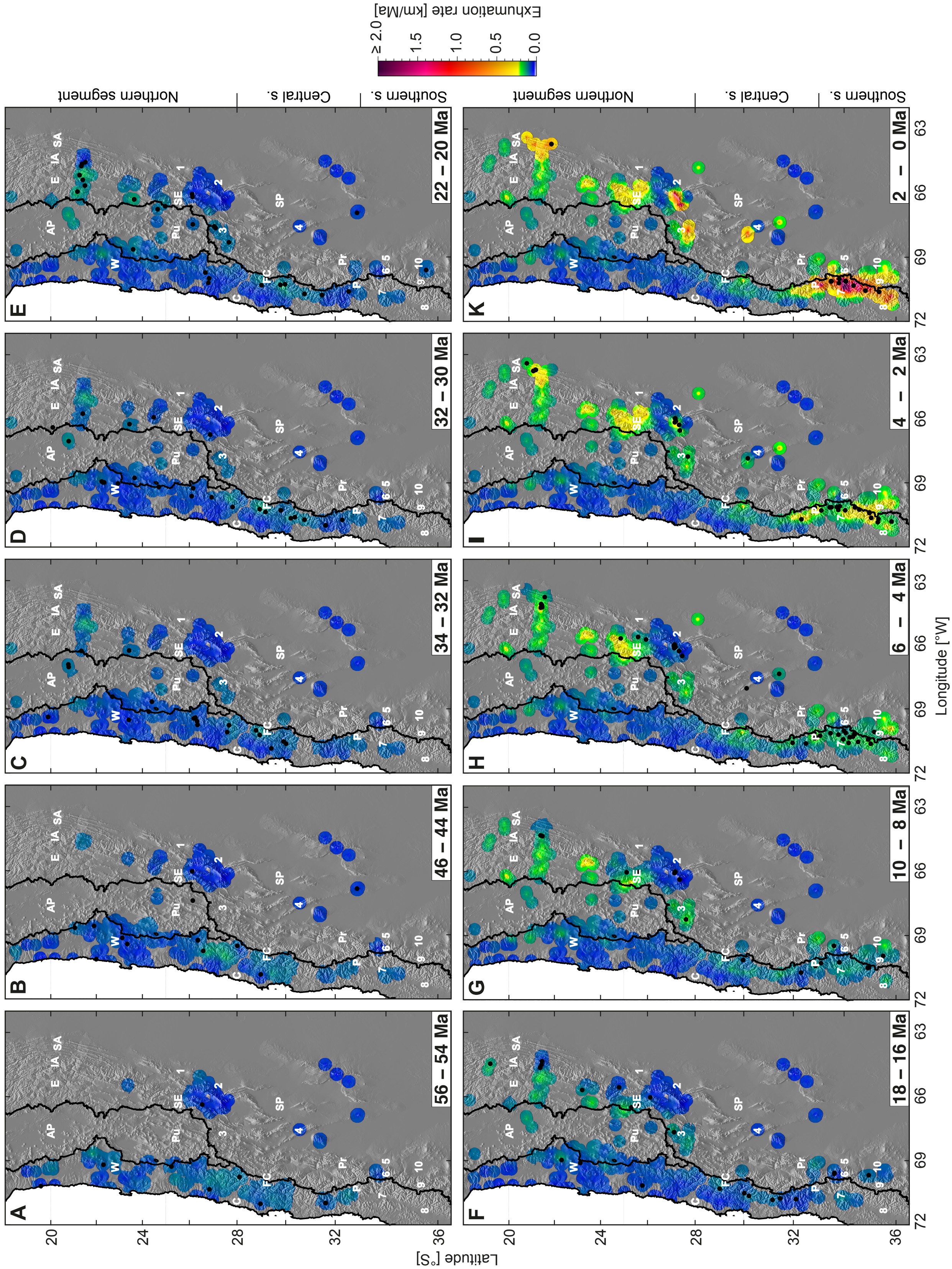
A
56 – 54 Ma
B
46 – 44 Ma
C
34 – 32 Ma
D
32 – 30 Ma
E
22 – 20 Ma
F
18 – 16 Ma
G
10 – 8 Ma
H
6 – 4 Ma
I
4 – 2 Ma
K
2 – 0 Ma
AP
E
IA
SA
W
Pu
SE
SP
C
FC
Pr
P
1
2
3
4
5
6
7
8
9
10
Northern segment
Central s.
Southern s.
Exhumation rate [km/Ma]
≥ 2.0
1.5
1.0
0.5
0.0
Latitude [°S]
20
24
28
32
36
Longitude [°W]
72
69
66
63

Fig. 10: Modelled exhumation rates for selected time intervals discussed in the text. Black line delineates the main water divide, black points represent thermochronological data falling into the respective time intervals. Numbers indicate specific locations referred to in the text: 1 = Santa Barbara system; 2 = Sierra Aconquíja; 3 = Fiambalá Basin; 4 = Sierra de Valle Fértil; 5 = Cuyo foreland basin; 6 = Aconcagua fold-and-thrust belt; 7 = West Andean fold-and-thrust belt; 8 = Laguna de Tagua Tagua; 9 = Malargüe fold-and-thrust belt; 10 = Malargüe foreland basin. Letters correspond to the following tectonomorphic units: AP = Altiplano; C = Coastal Cordillera; E = Eastern Cordillera; FC = Frontal Cordillera; IA = Interandean zone; P = Principal Cordillera; Pr = Precordillera; Pu = Puna; SA = Subandean zone; SE = southern Eastern Cordillera; SP = Sierra Pampeanas; W = Western Cordillera. Underlying topography from GEBCO_2014, 30 arc-s (Becker et al., 2009).

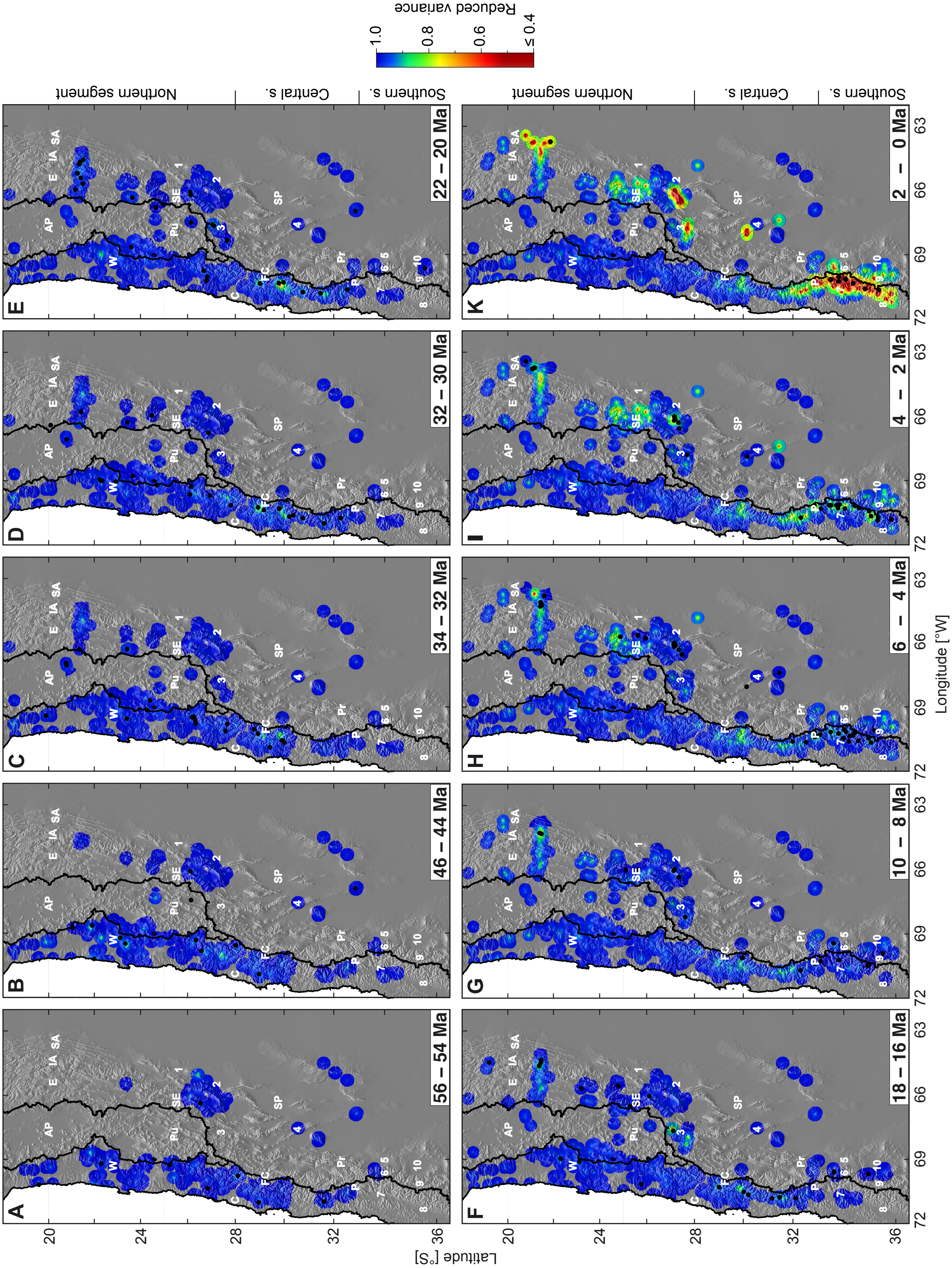

Fig. 11: Reduced variance corresponding to the exhumation rate maps shown in Fig. 10. Black line delineates the main water divide, black points represent thermochronological data falling

into the respective time intervals. See caption Fig. 10 for numbers and letters. Underlying topography from GEBCO_2014, 30 arc-s (Becker et al., 2009).

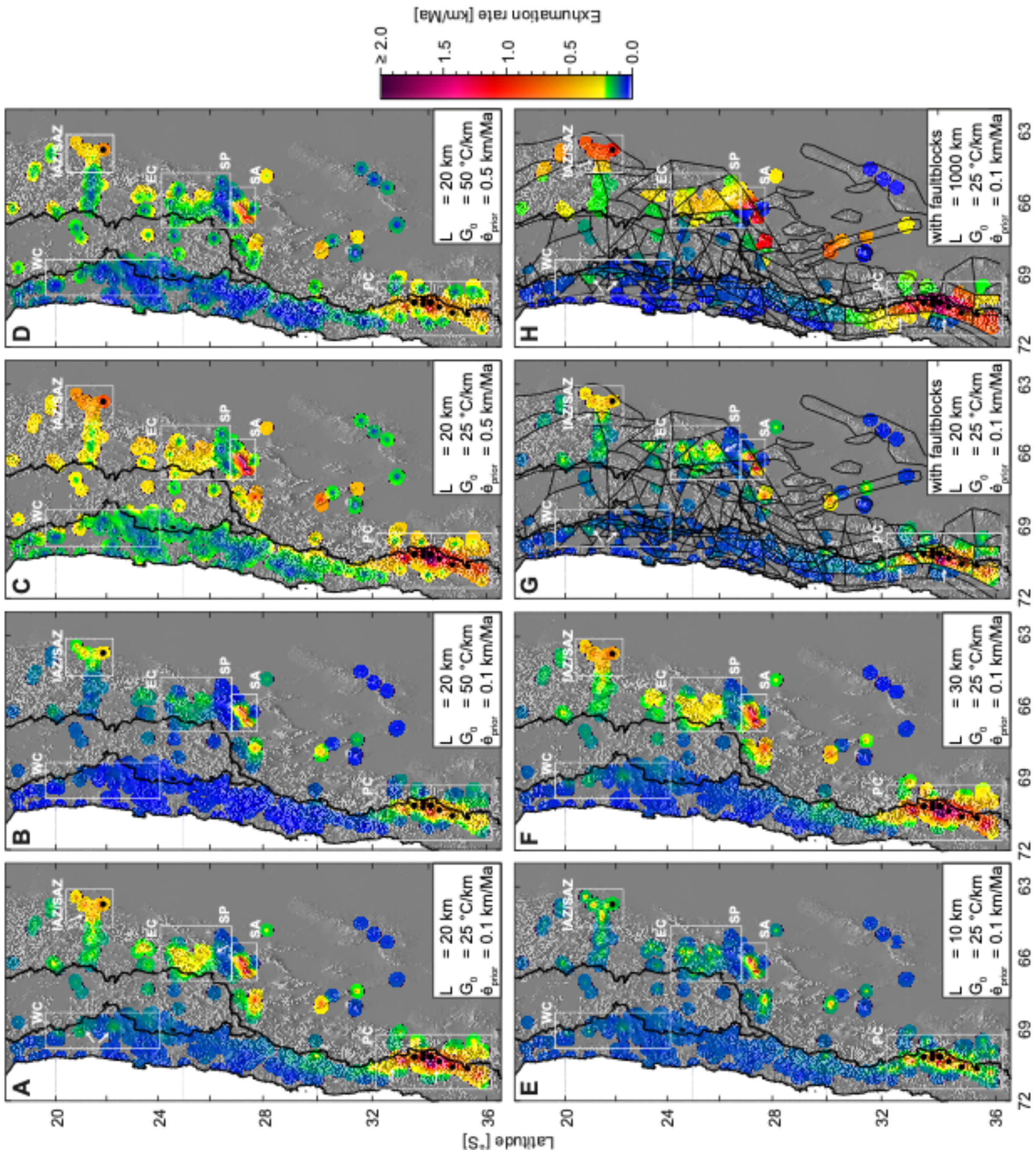

Fig. 12: Influence of the model parameters on the modelled exhumation rates of the most recent timestep (2-0 Ma). White rectangles delineate specific locations discussed in the text: EC = southern Eastern Cordillera; IAZ/SAZ = Inter- and Subandean zones; PC = southern Principal Cordillera; SA = Sierra Aconquíja, northern Sierra Pampeanas; WC = Western Cordillera. Arrows highlight differences between inversions modelled with and without fault blocks. **A-D)** Inversions with different combinations of $\dot{e}_{prior}$ (0.1, 0.5 km/Ma) and G_0 (25, 50

°C/km). Correlation length scale is 20 km. **E, F)** Inversions with the same set of parameter as in **A)** but with correlation lengthscales of 10 and 30 km, respectively. **G, H)** Inversions with fault blocks and the same set of parameter as in (A) and correlation lengthscales of 20 and 1000 km, respectively. Thin black lines delineate the faultblocks.

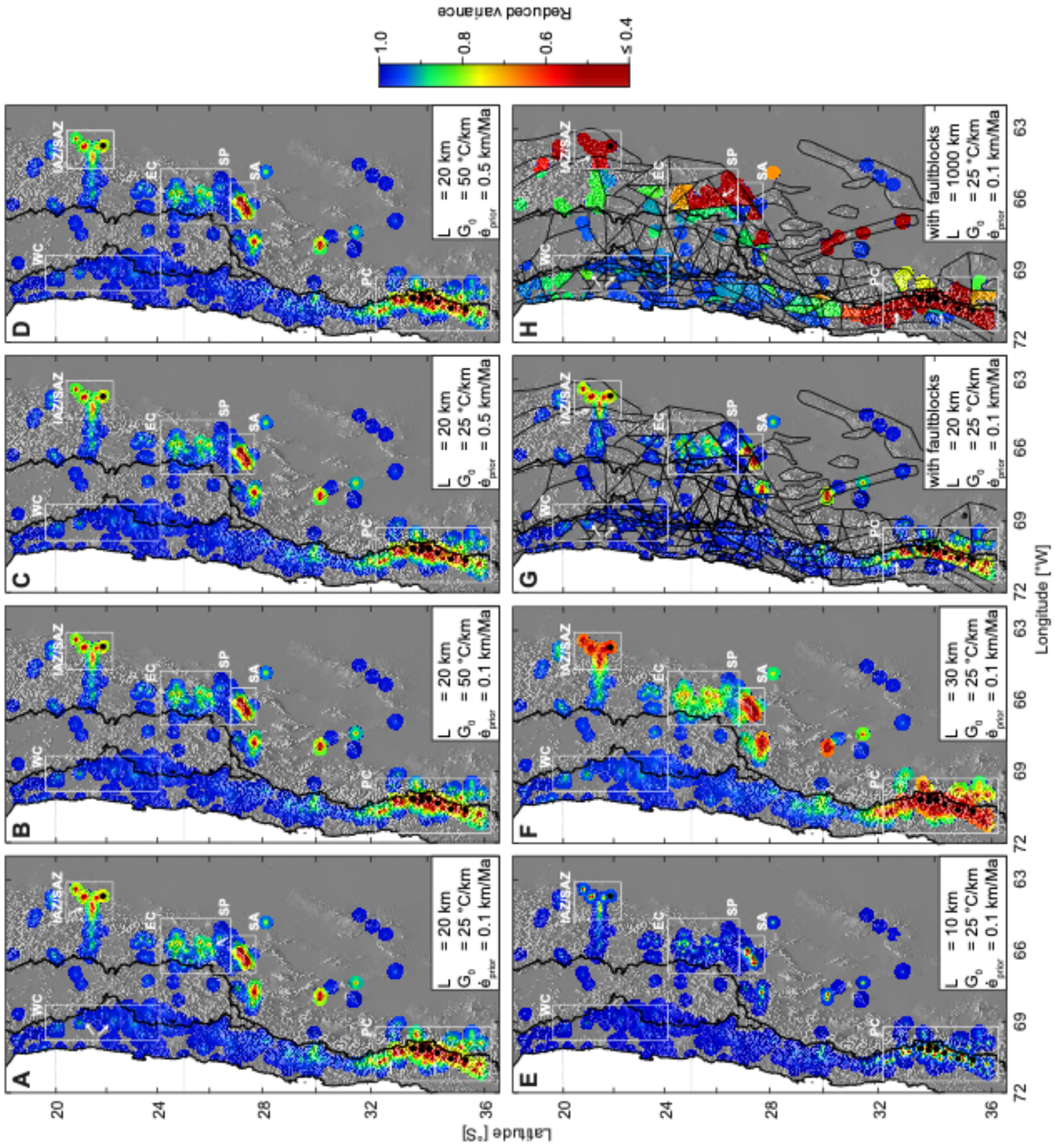

Fig. 13: Reduced variance of the inversion results shown in Fig. 12. White rectangles delineate specific locations discussed in the text: EC = southern Eastern Cordillera; IAZ/SAZ = Inter- and Subandean zones; PC = southern Principal Cordillera; SA = Sierra Aconquíja (Sierra Pampeanas); WC = Western Cordillera. Arrows highlight differences between inversions modelled with (G, H) and without (A) fault blocks.

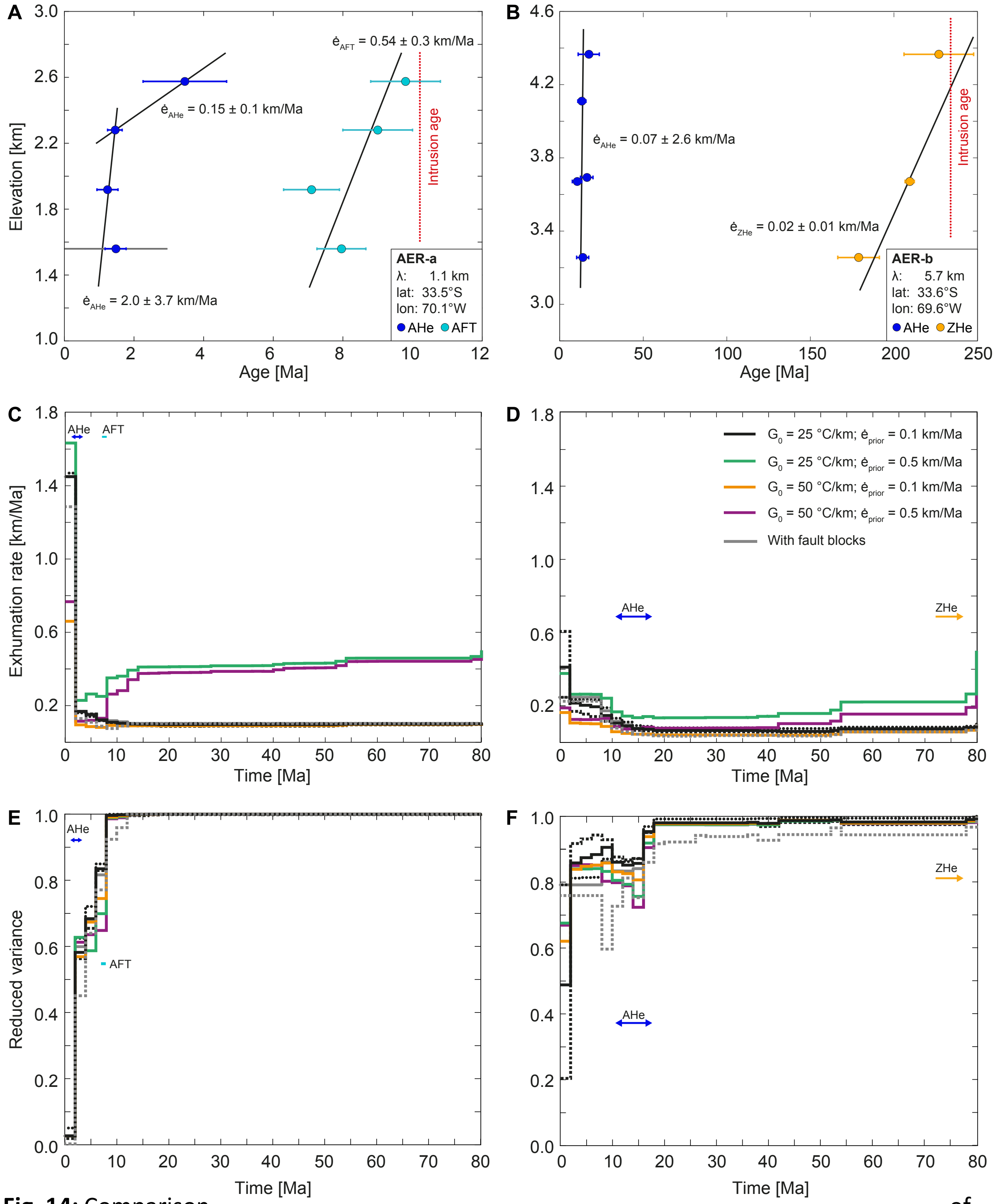

Fig. 14: Comparison of exhumation rates derived from age-elevation profiles and from the inversions for the southern segment of the study area. See Fig. 1 and supplementary Table S5 for locations and data. **A, B)** Age-elevation profiles at 33.5°S to the west (AER-a) and east (AER-b) of the water divide, with linear best-fit after York et al. (2004) indicating the exhumation rate. For consistency with the inversion, average ages with standard deviation rather than individual grain ages are used. The AHe data of profile AER-a shows a break in slope that indicates an

increase in exhumation rate from 0.15 ± 0.1 km/Ma before 2 Ma (slope of the line connecting the two highest elevated samples) to 2.0 ± 3.7 km/Ma after 2 Ma. To get a meaningful linear fit, a higher uncertainty (1.5 Ma instead of 0.3 Ma; grey error bar) was given to the lowermost sample. **C, D)** Exhumation rates derived from the inversions at the respective locations of the age-elevation profiles using different sets of parameters. The ZHe data from AER-b is not used in the model because ages older than 80 Ma are excluded in the inversion. Solid lines represent inversions with a correlation length scale of 20 km and varying G_0 (25 and 50 °C/km) and $\dot{e}_{prior}$'s (0.1 and 0.5 km/Ma). Black lines are inversions with our preferred parameter set (G_0 = 25 °C/km; $\dot{e}_{prior}$ = 0.1 km/Ma) run with correlation length scales of 10 km (dotted), 20 km (solid) and 30 km (dashed). Grey lines represent the inversion with fault blocks and correlation length scales of 20 km (solid) and 1000 km (dashed), respectively. Colored arrows indicate the time span covered by the respective thermochronological systems. **E, F)** The reduced variance of the model drops when information of the thermochronological data are available.

Supplementary Material

1. Thermochronological analyses (AHe, ZHe and AFT)

To increase spatial coverage on the western side of the Andes, where thermochronometric data was sparse, we have collected 149 new samples from Chile during several field campaigns that were realized over the last 4 years. After crushing and sieving of the bedrock samples to gain the fraction between 25-350 µm, apatite and zircon crystals were concentrated using the traditional two-steps heavy liquid separations (3.1 and 3.3 g/cm^{-3}) and Frantz paramagnetic separation techniques. Different laboratories were involved for mineral separation and dating. Samples labelled with the prefix 14NC (Campaign 1) were separated at the Geological Institute of the Bulgarian Academy of Sciences in Sofia, Bulgaria, those with the prefix Clin (Campaign 2) by Zirchron LLC in Tucson, Arizona, and those with the prefix CLRK (Campaign 3) by the Langfang Yantuo Geological Service Company in Langfang, China. Samples from Campaign 1 and 2 (14NC-x; Clin-x) were analysed at the ARHDL lab (University of Arizona, Tucson) for (U-Th)/He dating. Fission-track analyses were conducted at the ISTerre (Grenoble, FR) (14NC-x) and at the ETH Zurich (Zurich, Switzerland) (Clin-x), respectively. CLRK-x samples were analysed at Dalhousie University (Halifax, CA) for (U-Th)/He dating and AFT.

1.1. (U-Th)/He dating of zircons and apatites

For each sample, 2 to 5 apatite and zircon crystals were manually selected under a high-magnification stereoscopic microscope for (U-Th)/He analyses. Preference was given to euhedral, transparent, inclusion- and crack-free grains with the smallest dimensions being not less than 70 µm (CLRK-x) or 60 µm (14NC-x and Clin-x). Grain dimensions of apatites were determined and photographed in at least two different orientations parallel and perpendicular to the c-axis. For zircon crystals, the bipyramidal tip heights and two different c-axis parallel widths were measured. In rare cases, where all inclusion-free grains were broken, apatite and zircon grains with one damaged tip were analysed. This was taken into account during the α-particle ejection corrections (e.g., Farley et al., 1996). All selected grains were packed in Nb tubes for ^{4}He extraction.

1.1.1. (U-Th)/He analytical procedure for samples 14NC-x and Clin-x analysed at the University of Arizona

Apatite grains were heated by a focused laser beam (either CO_2 or diode) to 900-1000°C for 3 minutes, zircon grains were heated 3 times to ~1000-1250°C for 20 minutes each time to allow complete degassing of ^{4}He. The ^{4}He was spiked with 0.1-0.2 pmol ^{3}He and analysed by a Balzers quadrupole mass spectrometer (QMS). Durango apatite and Fish Canyon tuff were used as external standards for apatite and zircon measurements, respectively. The ablated grains were spiked with nitric acid solutions enriched in ^{233}U, ^{229}Th (and ^{42}Ca, ^{147}Sm for apatites, ^{90}Zr for zircon) isotopes and dissolved in acid to determine molar contents of U, Th, Sm, Ca, and Zr via isotope-dilution ICP-MS. Preparation procedure and analytical details are provided in the ARHDL Report 1 of Reiners and Nicolescu (2006). All ages were corrected for α-particle ejection by using individual grain dimensions (Reiners et al., 2018).

1.1.2. (U-Th)/He analytical procedure for samples CLRK-x analysed at Dalhousie University

^{4}He measurements were completed on a custom-built He-extraction line equipped with a 40 W diode laser and a Pfeiffer Vacuum Prisma quadrupole mass-spectrometer. Apatite crystals were heated to 1050° C for 5 minutes, whereas zircon crystals were heated to 1250° C for 15 minutes. After ^{4}He extraction, a precisely measured aliquot of ^{3}He was added to the sample and the ^{3}He/^{4}He ratio was measured using the quadrupole mass-spectrometer. This procedure was repeated once for apatite crystals to assure that no ^{4}He is left in the grain. Since zircon crystals retain ^{4}He to higher temperatures, the ^{4}He extraction for zircon grains was repeated minimum 3 times until the amount of ^{4}He in the last re-extraction was less than 1% of the total ^{4}He extracted from this grain. Typical analytical uncertainties are in the range of 1.5-2% (1σ) for both zircon and apatite crystals. Durango apatites and Fish Canyon tuff zircons were used as external standards for apatite and zircon measurements, respectively, that went through the same analytical procedures as unknown samples to ensure accuracy, reproducibility and reliability of the data.

After ^{4}He extraction, both apatite and zircon crystals were spiked with mixed ^{235}U, ^{230}Th, and ^{149}Sm and dissolved following standard dissolution protocols for these minerals. Apatite crystals were dissolved in HNO_3 at 80°C for 1.5 hours, whereas zircon crystals were dissolved in high-pressure dissolution vessels in mixture of concentrated HF and HNO_3 at 200°C for 96 hours. Isotopic ratios were measured using an iCAP Q ICP-MS.

Raw data were reduced using the Helios software package developed by R. Kislitsyn and D. Stockli at Dalhousie University (Halifax, CA) specifically for (U-Th)/He data reduction. The α-ejection correction was calculated based on surface to volume ratio (Farley at al., 1996).

1.2. Fission-track dating of apatites

Apatite grains were mounted into epoxy resin, polished to expose the internal grain surface and etched for 20s at 21°C in 5.5 M HNO_3. All mounts were prepared using the external detector method (Hurford and Green, 1983).

Samples from Campaign 1 (14NC-x) were irradiated at the FRM II research reactor in Garching, Germany under a nominal neutron fluence of $8 \cdot 10^{15}$ n/cm^2 and with IRMM540R dosimeter glasses (15 ppm U) and Fish Canyon tuff and Durango apatite as external standards. Samples from Campaign 2 (Clin-x) and Campaign 3 (CLRK-x) were irradiated at the Radiation Centre of the Oregon State University under a nominal neutron fluence of $1.2 \cdot 10^{16}$ n/cm^2 and

$1 \cdot 10^{16}$ n/cm^2, respectively. The high flux used for samples Clin-x was chosen based on the expected young cooling ages and relatively low (~1ppm) uranium content. CN5 dosimeter glasses and Durango apatite as external standard were used for samples Clin-x and CLRK-x. After irradiation, the low-U muscovite detectors that covered the apatite grain mounts and glass dosimeters were etched in 48% HF for 18 min at 23 °C (samples 14NC-x) and in 40% HF for 45 min at 21 °C (samples Clin-x and CLRK-x) to reveal induced fission tracks. Dry counting was performed under an optical microscope at a magnification of 1000 (CLRK-x) and 1250 (14NC-x and Clin-x), respectively. Fission-track ages were calculated using a weighted mean Zeta calibration factor (Hurford and Green, 1983) based on IUGS ages standards (Durango, Fish Canyon and Mount Dromedary apatites) (Hurford, 1990; Miller et al., 1985), giving Zetas of $\zeta_{\text{ISTerre}} = 310.4 \pm 13.8$ for samples 14NC-x, $\zeta_{\text{Zurich}} = 354.96 \pm 12.6$ for samples Clin-x and $\zeta_{\text{Dalhousie}} = 370.6 \pm 5$ for samples CLRK-x, respectively.

2. U-Pb analyses

A total of 75 zircon crystals from two samples (Clin22A - 39 crystals; Clin25A – 36 crystals) were analysed for U-Pb ages by LA-ICP-MS (supplementary Table S4, Fig. S5). Zircons were handpicked, mounted into epoxy and polished down to half thickness with a 1 µm diamond paste. Ablation spots of 50 µm were preselected on cathodoluminescence images conducted on a CamScanMV2300 SEM at the University of Lausanne. Neither sample showed mineral zonations, but the zircon grains of Clin22A have inclusion-rich cores and appear in two generations that are characterized by two different crystal sizes. Zircons from both generations were analysed. ^{238}U/^{206}Pb ages were obtained by measuring ^{202}Hg, ^{204}Pb, ^{206}Pb, ^{207}Pb, ^{208}Pb, ^{232}Th, ^{235}U, and ^{238}U intensities on an UP-193FX (ESI) ablation system interfaced to an Element XR sector field, single-collector ICP-MS (Thermo Scientific) at the University of Lausanne. Operation conditions were similar to Ulianov et al. (2012) and included a repetition rate of 5 Hz, a spot size of 50 µm and an on-sample energy density of 3 Jcm^{-2}. We used GJ-1 (Jackson et al., 2004; ID–TIMS $^{206}Pb/^{238}U$ age of 600.4 ± 0.4 Ma (Ulianov et al., 2012; Boekhout et al., 2012)) as a primary Reference material and Plesoviče zircon as a secondary standard ($^{206}Pb/^{238}U$ age of 337.13 ± 0.37 Ma; Slàma et al., 2008). The weighted mean $^{206}Pb/^{238}U$ age of our measurements for Plesoviče zircon is 335.6 ± 3.5 Ma (2σ of 1.1%). The measurements of the Plesoviče zircon crystals show a day-long drift from older (344.7 Ma) to younger (328.9 Ma) ages (supplementary Table S4 and Fig. S6), which corresponds to max. inaccuracies of ca. 2% relative to the ID-TIMS age. Such inaccuracies are considered normal for the U/Pb LA-ICP-MS dating of zircon (e.g., Schaltegger et al., 2015). The drift is not observed for the samples Clin22A and Clin25A. Common Pb contamination was qualitatively assessed by controlling the measured ^{202}Hg and ^{204}Pb. Weighted mean average ages with 2σ standard errors of analytically concordant values were calculated by using Isoplot 4.1 (Ludwig, 2001) (supplementary Fig. S5, Fig, S6).

3. Inverse model using fault blocks

The fault blocks of the study area were defined by an exploration team of First Quantum Minerals FQM using a variety of sources including seismic tomography, earthquake epicentres, satellite gravity enhanced with ground station readings, regional aeromagnetics, tectonostratigraphic geological mapping at 1:100.000-500.000, mapped faults from SERNAGEOMIN and SEGEMAR published maps and topography (Banyard and Farrar, 2018). The boundaries between the blocks are interpreted to be long-lived, deep seated structural corridors and as such may not find their expression in a single, traceable fault at surface (Banyard and Farrar, 2018). Thermochronological data in different blocks move independently from each other even if they are located within the correlation distance. An $\dot{e}_{prior}$ of 0.1 km/Ma, G_0 25 °C/km and correlation length scales of 20 and 1000 km, respectively, were used to test the influence of the fault blocks on the exhumation rates (Fig. 12G, H and supplementary movies, InversionG and InversionH).

References for supplementary material

Banyard, J., Farrar, A., 2018. Mapping of structural blocks in the Central Andes district. Int. Tech. Rep., FQM First Quantum Minerals ltd. Santiago de Chile, Chile.

Boekhout, F., Spikings, R., Sempere, T., Chiaradia, M., Ulianov, A., Schaltegger, U., 2012. Mesozoic arc magmatism along the southern Peruvian margin during Gondwana breakup and dispersal. Lithos, 146-147, 48–64.

Farley, K.A., Wolf, R.A., Silver, L.T., 1996. The effects of long alpha-stopping distances on (U-Th)/He ages. Geochim. Cosmochim. Acta, 60, 4223–4229.

Hurford, A.J., 1990. Standardization of fission-track dating calibration: recommendation by the Fission Track Working Group of the I.U.G.S. Subcommission on geochronology, Chem. Geol., 80, 171-178.

Hurford, A.J., Green, P.F., 1983. The Zeta age calibration of fission-track dating. Isot. Geosci., 1, 285-371.

Jackson, S.E., Pearson, N.J., Griffin, W.L., Belousova, E.A., 2004. The application of laser ablation-inductively coupled plasma-mass spectrometry to in situ U-Pb zircon geochronology. Chem. Geol., 211 (1), 47–69.

Ketcham, R.A., Gautheron, C., Tassan-Got, L., 2011. Accounting for long alpha-particle stopping distances in (U-Th-Sm)/He geochronology: Refinement of the baseline case. Geochim. et Gosmochim. Acta, 75, 7779-7791.

Ludwig, K.R., 2001. Isoplot 4.1: A Geochronological Toolkit for Microsoft Excel. Spec. Publ., Vol. 4. Berkeley Geochronology Center, Berkley.

Miller, D.S., Duddy, I.R., Green, P.F., Hurford, A.J., Naeser, C.W., 1985. Results of interlaboratory comparison of fission-track age standards. Nucl. Tracks and Radiat. Meas., 10, 381-391.

Reiners, P.W., Nicolescu, S., 2006. Measurement of parent nuclides for (U-Th)/He chronometry by solution sector ICP-MS. ARHDL Report 1. https://www.geo.arizona.edu/~reiners/arhdl/arhdlrep1.pdf

Reiners, P.W., Carlson, R.W., Renne, P.R., Cooper, K.M., Granger, D.E., McLean, N.M., Schoene, B., 2018. Geochronology and Thermochronology, Wiley, 480 pp., ISBN: 978-1-118-45585-2.

Schaltegger, U., Schmitt, A.K., Horstwood, M.S.A., 2015. U–Th–Pb zircon geochronology by ID-TIMS, SIMS, and laser ablation ICP-MS: Recipes, interpretations, and opportunities. Chem. Geol., 402, 89-110.

Sláma, J., Košler, J., Condon, D.J., Crowley, J.L., Gerdes, A., Hanchar, J.M., Horstwood, M.S.A, Morris, G., Nadala, L., Norberg, N., Schaltegger, U., Schoene, B., Tubrett, M.N., Whitehouse, M.J., 2008. Plešovice zircon — A new natural reference material for U–Pb and Hf isotopic microanalysis. Chem. Geol., 249, 1–35.

Ulianov, A., Müntener, O., Schaltegger, U., Bussy, F., 2012. The data treatment dependent variability of U–Pb zircon ages obtained using mono-collector, sector field, laser ablation ICPMS. J. Anal. At. Spectrom., 27, 663-676

Supplementary Figures

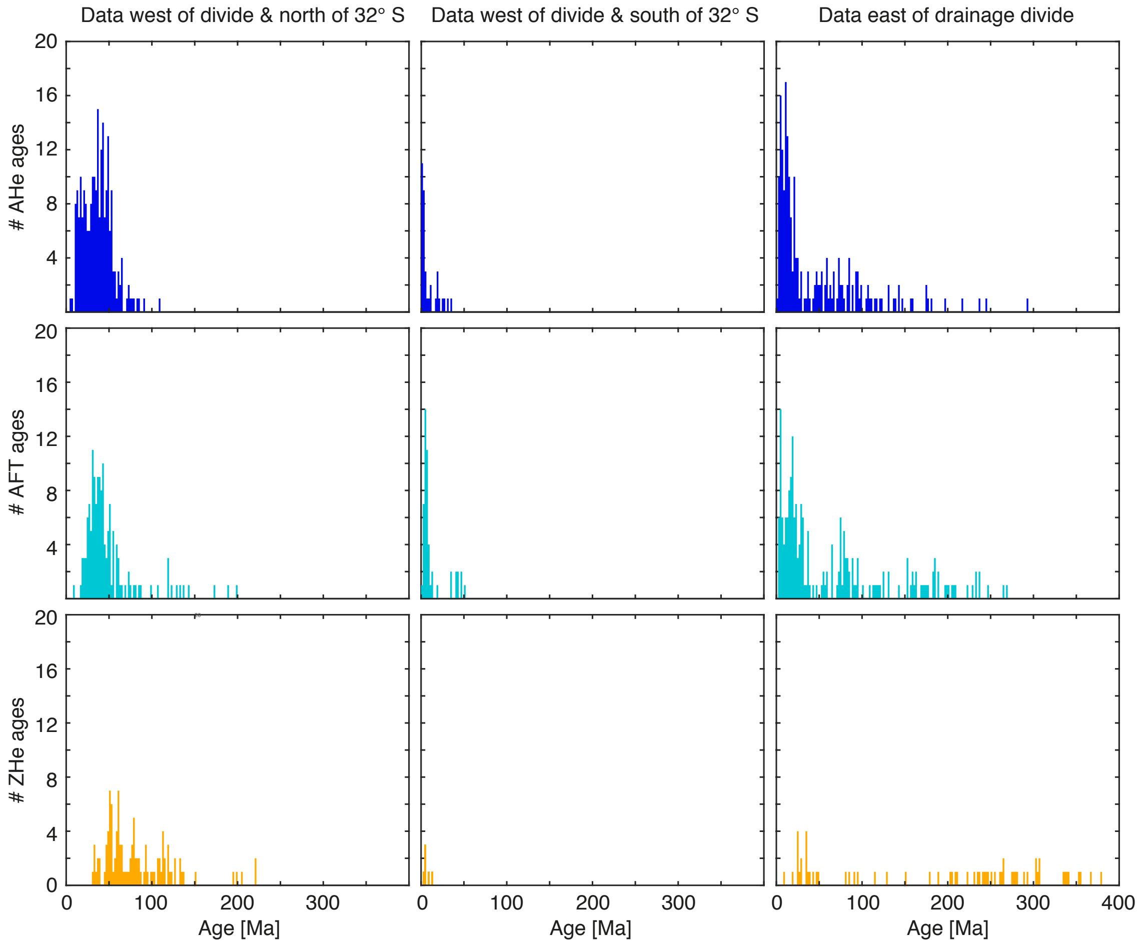

Fig. S1: Histograms of AHe, AFT and ZHe ages for the different data sets described in the text. **A)** Data west of the drainage divide and north of 32°S, **B)** data west of the drainage divide and south of 32°S and **C)** data east of drainage divide.

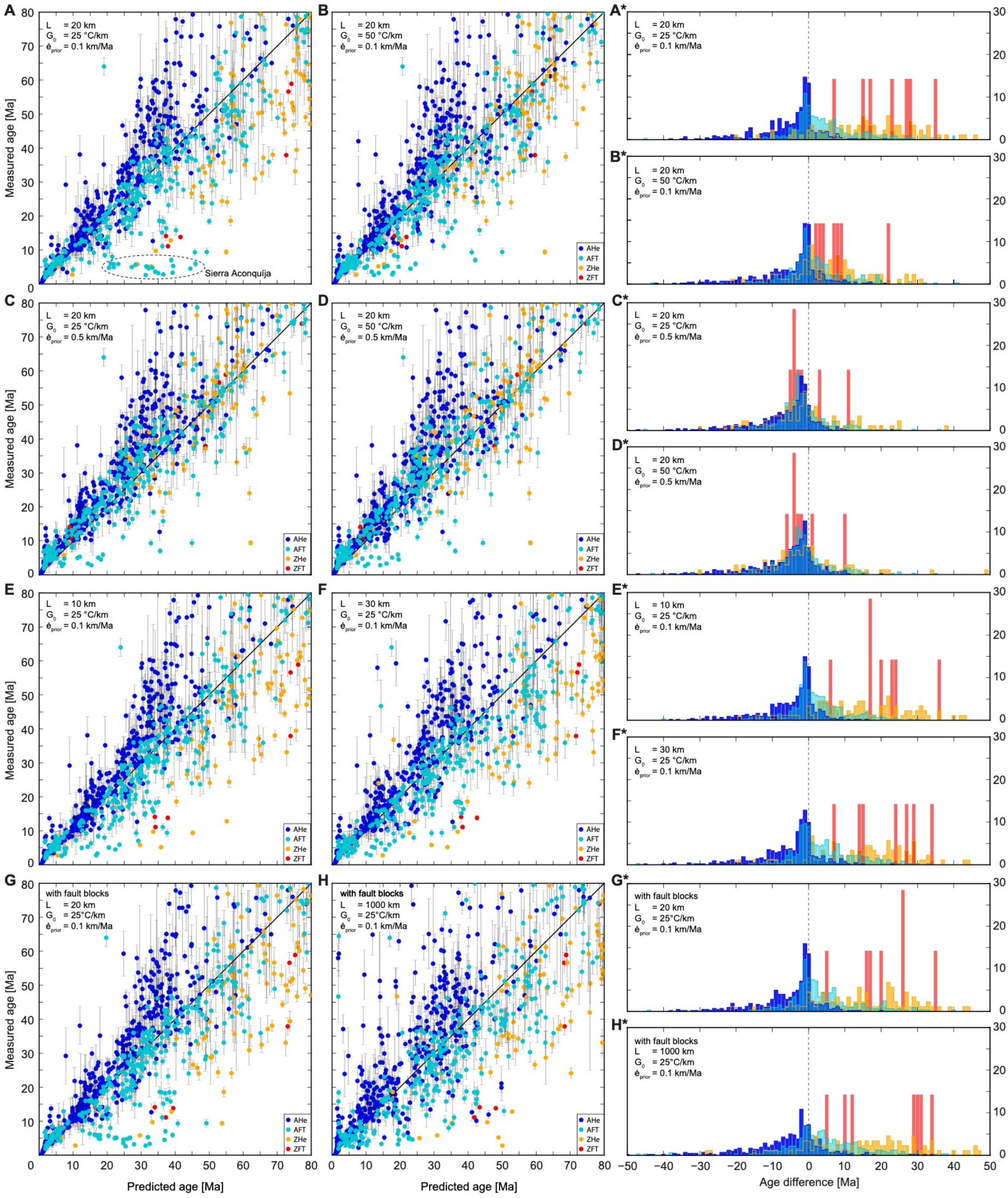

Fig. S2: Misfit and histograms for the eight tested inversions. **A-D)** Inversions with different combinations of $\dot{e}_{prior}$ (0.1, 0.5 km/Ma) and G_0 (25, 50 °C/km) and a correlation length scale of 20 km. **E, F)** Inversions with the same set of parameter as in (A) but with correlation lengthscales of 10 and 30 km, respectively. **G, H)** Inversions with fault blocks and the same set of parameter as in (A) and correlation lengthscales of 20 and 1000 km, respectively. **A*-H*)** Histograms of age differences (age_{pred}-age_{obs}) corresponding to inversions A-H.

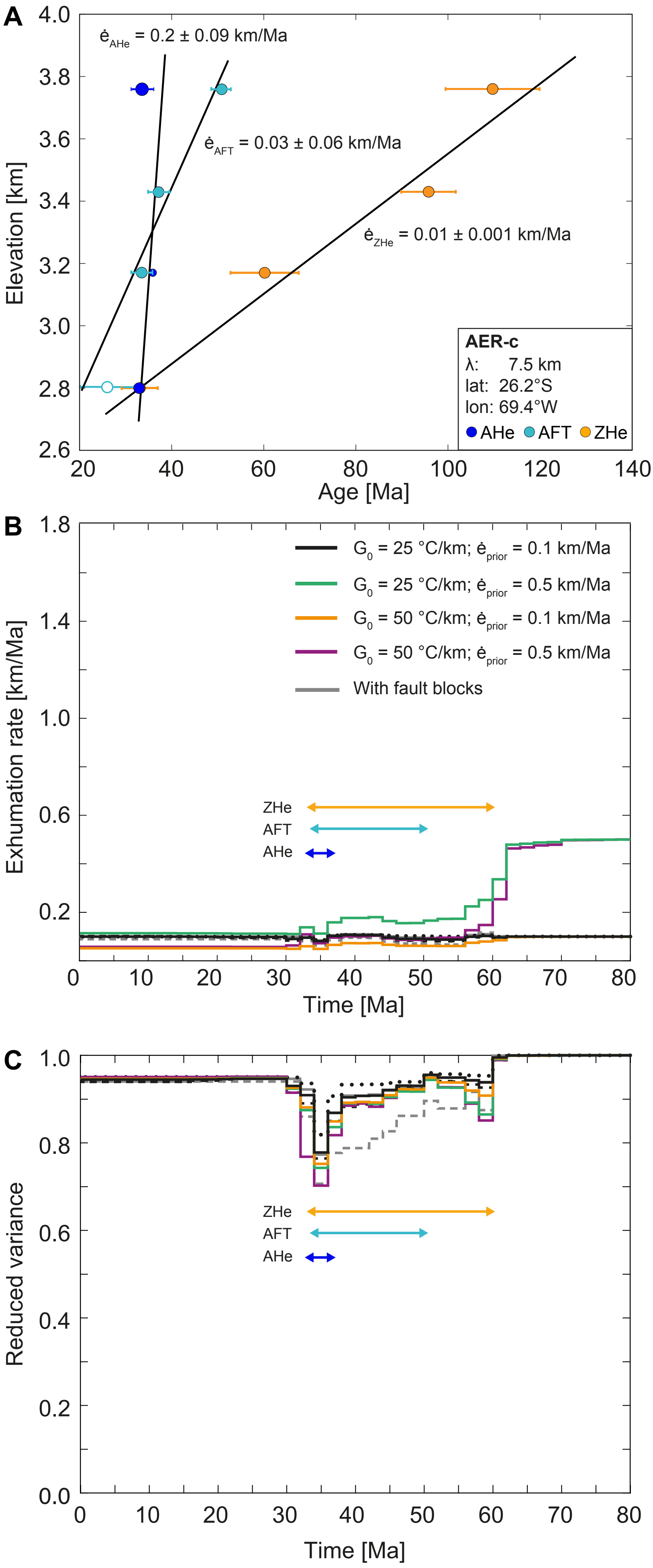
A
ė_AHe = 0.2 ± 0.09 km/Ma
ė_AFT = 0.03 ± 0.06 km/Ma
ė_ZHe = 0.01 ± 0.001 km/Ma
Elevation [km]
Age [Ma]
AER-c
λ: 7.5 km
lat: 26.2°S
lon: 69.4°W
● AHe ● AFT ● ZHe
4.0
3.8
3.6
3.4
3.2
3.0
2.8
2.6
20
40
60
80
100
120
140
B
G_0 = 25 °C/km; ė_prior = 0.1 km/Ma
G_0 = 25 °C/km; ė_prior = 0.5 km/Ma
G_0 = 50 °C/km; ė_prior = 0.1 km/Ma
G_0 = 50 °C/km; ė_prior = 0.5 km/Ma
With fault blocks
ZHe
AFT
AHe
Exhumation rate [km/Ma]
Time [Ma]
1.8
1.4
1.0
0.6
0.2
0
10
20
30
40
50
60
70
80
C
ZHe
AFT
AHe
Reduced variance
Time [Ma]
1.0
0.8
0.6
0.4
0.2
0.0
0
10
20
30
40
50
60
70
80

3019

Fig. S3: Comparison of exhumation rates in the northern segment of the study area (26.2°S) derived from the age-elevation profile AER-c and from our inversion (see Fig. 1 and supplementary Table S5 for location and data). **A)** Age-elevation profile with linear best-fit indicating the exhumation rate. For consistency with the inversion, average ages with standard deviation rather than individual grain ages are used. Open circles represent thermochronological ages are excluded in the inversion. **B)** Exhumation rates derived from the inversion at the location of the age-elevation profile shown in (A) using different sets of parameters. Solid lines represent inversions with a correlation length scale of 20 km and varying G_0 (25 and 50 °C/km) and $\dot{e}_{prior}$'s (0.1 and 0.5 km/Ma). Black lines represent inversions with our preferred set of parameters ($G_0 = 25$ °C/km; $\dot{e}_{prior} = 0.1$ km/Ma) and correlation length scales of 10 km (dotted), 20 km (solid) and 30 km (dashed). Grey lines represents the inversion with fault blocks and correlation length scales of 20 km (solid) and 1000 km (dashed), respectively. Colored arrows indicate the time span covered by the respective thermochronological systems. **C)** The reduced variance of the model drops when information of the thermochronological data are available.

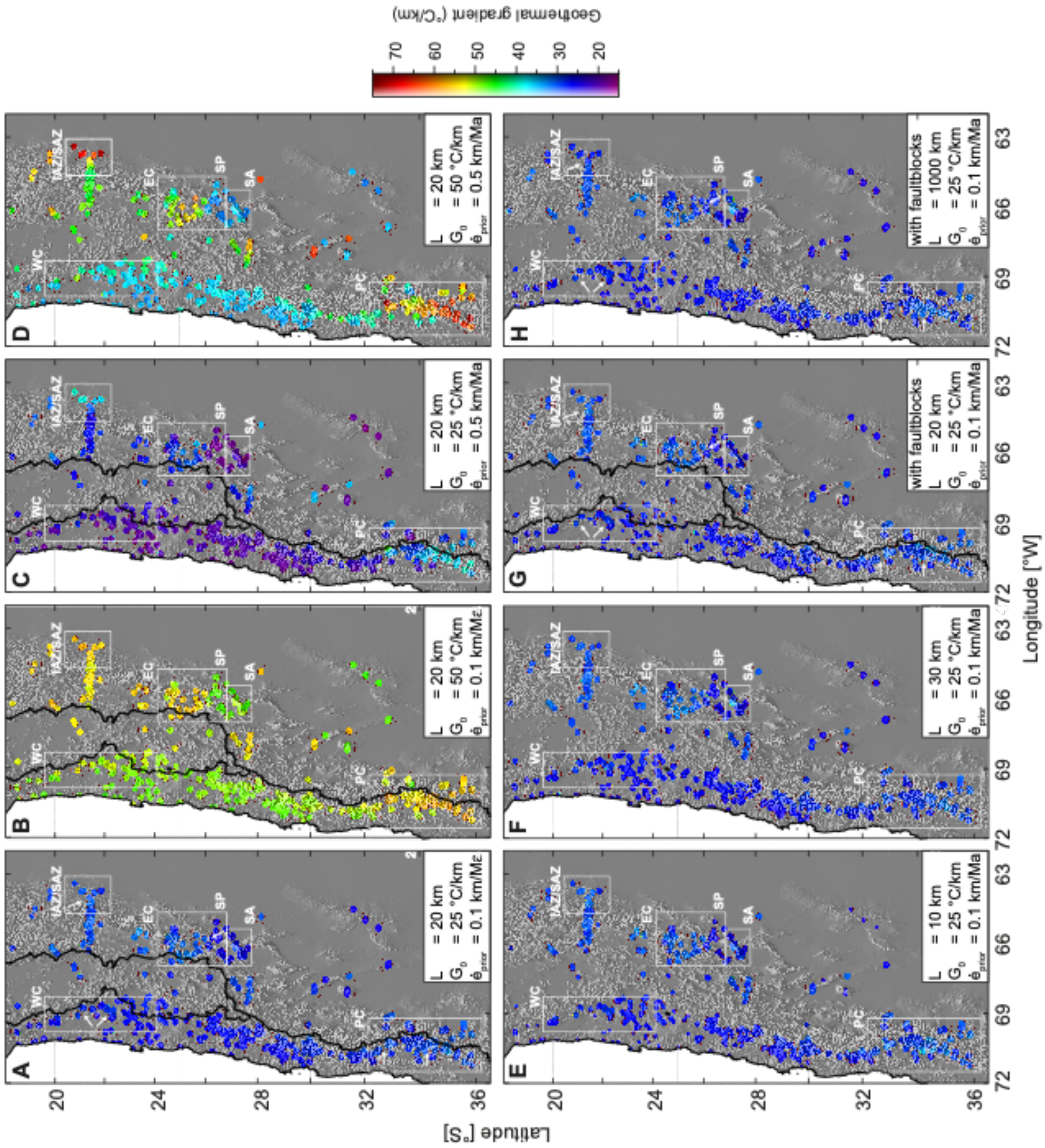

Fig. S4: Modelled present-day heat flow for the tested inversions. White rectangles delineate specific locations discussed in the text: EC = southern Eastern Cordillera; IAZ/SAZ = Inter- and Subandean zones; PC = southern Principal Cordillera; SA = Sierra Aconquíja, northern Sierra Pampeanas; WC = Western Cordillera. **A-D)** Inversions with different combinations of $\dot{e}_{prior}$ (0.1 and 0.5 km/Ma) and G_0 (25 and 50 °C/km) and a correlation length scale of 20 km. **E, F)** Inversions with the same set of parameter as in (A) but with correlation lengthscales of 10 and 30 km, respectively. **G, H)** Inversions with fault blocks using the same set of parameter as in (A) and correlation lengthscales of 20 and 1000 km, respectively.

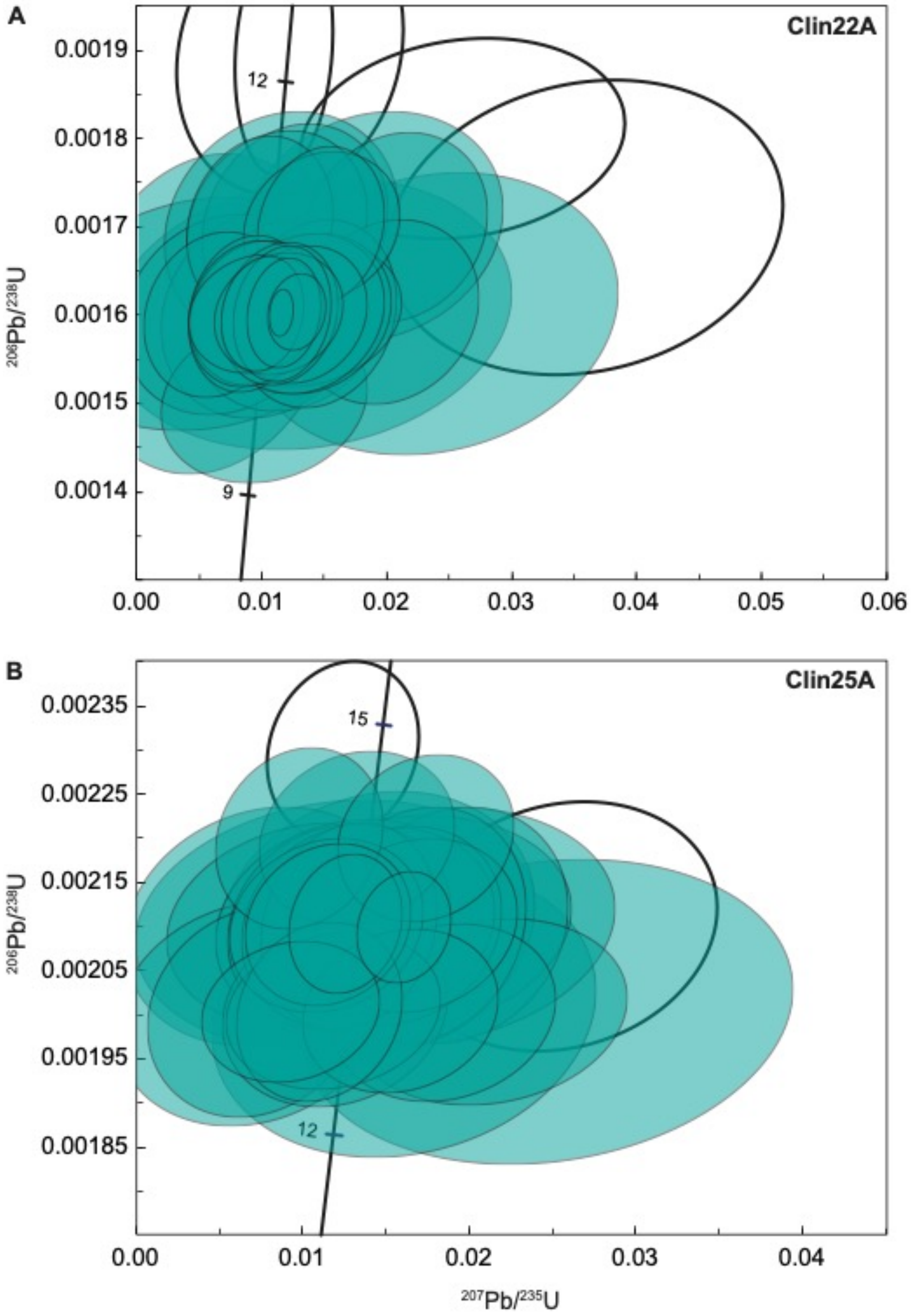

Fig. S5: U-Pb Concordia diagrams for samples Clin22A and Clin25A. Discordant ages are shown as empty, black ellipses.

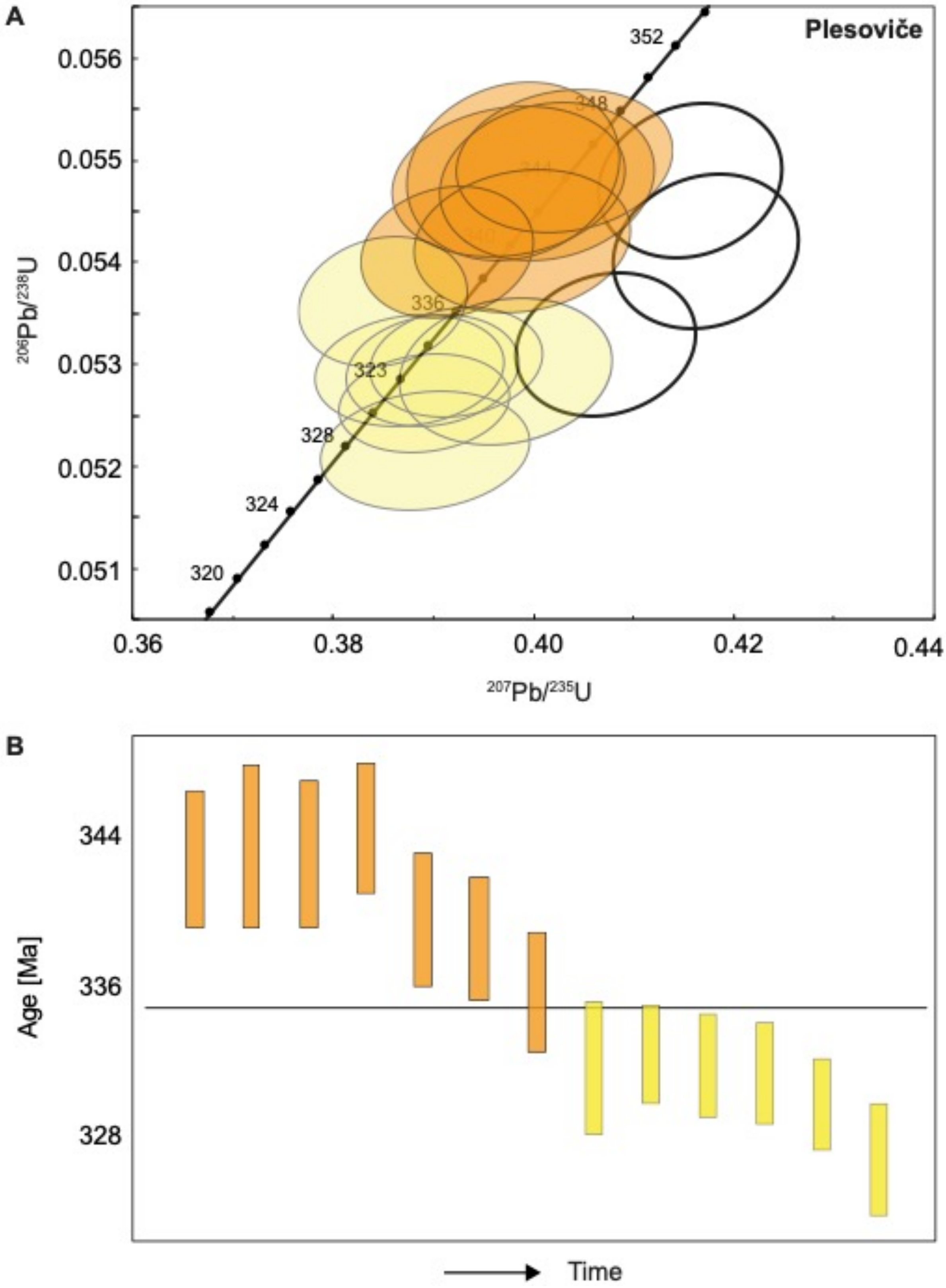

Fig. S6: A) U-Pb Concordia diagram of Plesoviče Secondary standard. Discordant ages are shown in empty, black ellipses. **B)** Observed day-long drift of the Plesoviče Secondary standard. Black line represents mean value of concordant ages (335.6 ± 3.5 Ma).